

Development of a Rig and Testing Procedures for the Experimental Investigation of
Horizontal Axis Kinetic Turbines

by

Catalina Lartiga
B.Sc., Catholic University of Chile, 2001

A Thesis Submitted in Partial Fulfilment of the
Requirements for the Degree of

MASTER OF APPLIED SCIENCES

in the Department of Mechanical Engineering

© Catalina Lartiga, 2012
University of Victoria

All rights reserved. This thesis may not be reproduced in whole or in part, by
photocopying or other means, without the permission of the author.

Development of a Rig and Testing Procedures for the Experimental Investigation of
Horizontal Axis Kinetic Turbines

by

Catalina Lartiga
B.Sc., Catholic University of Chile, 2001

Supervisory Committee

Dr. Curran Crawford., Supervisor
(Department of Mechanical Engineering)

Dr. Peter Oshkai, Departmental Member
(Department of Mechanical Engineering)

Supervisory Committee

Dr. Curran Crawford., Supervisor
(Department of Mechanical Engineering)

Dr. Peter Oshkai, Departmental Member
(Department of Mechanical Engineering)

ABSTRACT

The research detailed in this thesis was focused on developing an experimental testing system to characterize the non-dimensional performance coefficients of horizontal axis kinetic turbines, including both wind turbines and tidal turbines. The testing rig was designed for use in a water tunnel with Particle Image Velocimetry (PIV) wake survey equipment to quantify the wake structures. Precision rotor torque measurement and speed control was included, along with the ability to yaw the rotor. The scale of the rotors were purposefully small, to enable rapid-prototyping techniques to be used to produce many different test rotors at low cost to furnish a large experimental dataset.

The first part of this work introduces the mechanical design of the testing rig developed for measuring the output power of the scaled rotor models with consideration for the requirements imposed by the PIV wake measurements. The task was to design a rig to fit into an existing water tunnel facility with a cross sectional area of 45 by 45 cm, with a rotor support structure to minimize the flow disturbance while allowing for yawed inflow conditions. A rig with a nominal rotor diameter of 15 cm was designed and built. The size of the rotor was determined by studying the fluid similarities between wind and tidal turbines, and choosing the tip speed ratio as a scaling parameter. In order to maximize the local blade Reynolds number, and to obtain different tip speed ratios, the rig allows a rotational speed in the range of 500 to 1500 RPM with accurate rotor angular position measurements. Rotor torque measurements enable rotor mechanical power to be calculated from simulation results. Additionally, it is included in this section a description of the instrumentation for measurement and the data acquisition system.

It was known from the outset that measurements obtained in the experiments would be subject to error due to blockage effects inherent to bounded testing facilities. Thus, the second part of this work was dedicated to developing a novel Computational Fluid Dynamics (CFD) methodology to post-process the experimental data acquired. This approach utilizes the velocity field data at the rotor plane obtained from the water tunnel PIV test data, and CFD simulations based on the actuator disk concept to account for blockage without the requirement for thrust data which would have been unreliable at the low forces encountered in the tests.

Finally, the third part of this work describes the practical aspects of the laboratory project, including a description of the operational conditions for turbine testing. A set of preliminary measurements and results are presented, followed by conclusions and recommendations for future work. Unfortunately, the water tunnel PIV system was broken and thus unavailable for more than a year, so only mechanical measurements were possible with the rig during the course of this thesis work.

Contents

Supervisory Committee	ii
Abstract	iii
Table of Contents	v
List of Tables	viii
List of Figures	ix
Nomenclature	xii
Acknowledgments	xvii
Dedication	xviii
1 Introduction	1
1.1 Horizontal Axis Tidal Turbines	2
1.2 Experimental Kinetic Turbine Rotor Investigations	3
1.2.1 Previous Test Campaigns	4
1.2.2 Blockage effects	5
1.3 Motivation and Contributions	6
1.4 Thesis Outline	8
2 Rig Design	9
2.1 Water Tunnel Facility	10
2.2 Scaling Parameters	11
2.2.1 Rotor Size	13
2.2.2 Force Estimation	16

2.3	Finite Element Method (FEM) Modelling	18
2.3.1	Failure Criteria and Maximum Deflection	18
2.3.2	Modal Analysis	20
2.3.3	Summary of the FEM Results	20
2.4	Mechanical Design	22
2.4.1	Instrument Structure	24
2.4.2	Belt System	25
2.4.3	Submersed Structure	28
2.4.4	The Rotor	30
2.4.5	Yaw System	32
2.5	Instrumentation	33
2.5.1	The Drive System	35
2.5.2	The Motor	36
2.5.3	Torque cell	37
2.5.4	PIV system	39
2.5.5	DAQ Rio System	42
3	Computational Fluid Dynamic Simulations	45
3.1	Modelling Approach	46
3.1.1	Porous disk	46
3.1.2	Domain	46
3.1.3	Boundary Conditions	48
3.2	Computational Model	49
3.2.1	Governing Equations	49
3.2.2	Momentum Source Sink	51
3.2.3	CFX Boundary Conditions	52
3.3	CFD Simulation Results	53
3.3.1	Unbounded Flow Validation	54
3.3.2	Bounded Flow Results	56
3.3.3	Tunnel Wall Boundary Growth Effects	57
3.3.4	Reynolds Dependency Analysis	59
4	Tunnel Blockage Correction Models	62
4.1	Thrust Based Analytical Models	63
4.1.1	Momentum Based Model	64

4.2	Blockage Correction Model Development	66
4.2.1	CFD Correction Factors	69
5	Experimental Procedures and Testing Campaigns	73
5.1	Objectives of the experiment	74
5.1.1	Power output	74
5.2	Experiment Protocol	75
5.3	Experimental Blade Sets	76
5.4	Measurement Error Estimation	77
5.4.1	Error estimation	78
5.5	Initial Testing Campaign	80
5.6	Second Testing Campaign	81
5.6.1	Operational Conditions	82
5.6.2	Experimental Results	83
5.6.3	Surface Roughness and Reynolds Number Effects	84
5.6.4	Estimation of Blockage Effects	86
6	Conclusions	92
6.1	Rig Design	92
6.2	Computational Fluid Dynamic Simulations	93
6.3	Experimental Study	93
6.4	Future Work	94
	Bibliography	95
A	Momentum Theory: The Actuator Disc Concept	100
B	Finite Element Analysis Modelling	105
B.1	Geometry and Material Properties	105
B.2	Forces Applied to the System	108
B.3	Maximum Deflection - Results	109
B.4	Modal Analysis - Results	110
B.5	Mesh Refinement	110
C	PIV Theory	113

List of Tables

Table 2.1	Full size tidal turbine versus scaled model	15
Table 2.2	Forces at the rotor plane	17
Table 2.3	Dimensions resulting from FEM analysis	22
Table 2.4	Characteristics of the candidate belts	28
Table 3.1	ΔC_P (%) with respect theory value for different disc thickness	55
Table 3.2	Cases for mesh dependency study	56
Table 3.3	ΔC_P (%) with respect theory value for different mesh configurations	56
Table 3.4	Maximum C_P values	58
Table 3.5	Turbine size and flow conditions for additional RANS simulations	60
Table 5.1	Pumping system frequencies and tunnel inflow velocity	76
Table 5.2	Uncertainties of measurement	79
Table 5.3	Pumping system frequencies and tunnel inflow velocity	83
Table B.1	Configurations of study for modal analysis	106
Table B.2	Maximum deflections and stresses (Non-yawed condition)	110
Table B.3	Max.deflections and stresses at 30° yaw angle	110
Table B.4	Maximum deflections and stresses at 45° yaw angle	111
Table B.5	Result of modal analysis - natural frequencies [Hz]	111

List of Figures

Figure 1.1	Tidal Turbine Industry	3
(a)	Tidal Generation Ltd	3
(b)	Marine Current	3
(c)	Lunar Energy	3
Figure 1.2	Actuator disk concept in open and bounded flows	6
(a)	Unbounded domain	6
(b)	Bounded domain (e.g. water tunnel)	6
Figure 2.1	Water tunnel facility	10
Figure 2.2	The energy extracting stream-tube of a wind turbine (adapted from [1])	14
Figure 2.3	Schematic of the testing rig	19
Figure 2.4	FEM tube model of the testing rig	21
Figure 2.5	Schematic operation	24
Figure 2.6	Key components of the rig	25
Figure 2.7	Components of the instrument structure	26
Figure 2.8	Rig for belt testing	27
Figure 2.9	Submerged support structure	29
Figure 2.10	Model of fairings covering the submerged structure	30
Figure 2.11	Rotor assembly	31
Figure 2.12	Yaw system operation	33
Figure 2.13	PIV system layout	34
Figure 2.14	Experiment system schematic	36
Figure 2.15	Drive system	37
Figure 2.16	Performance curve Parker Motor HV233	38
Figure 2.17	Novatech installation schematic	39
Figure 2.18	General schematics of PIV system	40

Figure 2.19	CompactRio package	43
Figure 2.20	LabView interface	44
Figure 3.1	Quarter domain water tunnel model (ANSYS CFX)	47
Figure 3.2	CFX quarter domain boundary conditions	52
Figure 3.3	C_P v/s C_T for turbulent flow conditions in bounded domain with opening boundary conditions	54
Figure 3.4	C_P v/s C_T for turbulent flow conditions in water tunnel domain	57
Figure 3.5	C_P values for a wider range of Thrust Coefficients	58
Figure 3.6	Boundary layer effect for a rotor diameter 15 mm (9% blockage ratio) referenced to tunnel conditions	59
Figure 3.7	C_P v/s C_T , Unbounded domain	61
Figure 3.8	C_P increment v/s blockage ratio at $C_T = 8/9$	61
Figure 4.1	Actuator disk model in a closed tunnel section	65
Figure 4.2	Trend of C_P v/s C_T in water tunnel and unbounded domains	67
Figure 4.3	CFD-computed corrected velocity to inlet velocity ratio for different blockage ratios and operational conditions	69
Figure 4.4	Comparison between analytical and CFD power coefficient corrections (all values corrected to free-stream, C_T referred to tunnel conditions)	71
Figure 4.5	Correction curve for the experimental testing referenced to tunnel conditions	72
	(a) Ratio of corrected velocity to tunnel velocity v/s axial induction factor for a 9% blockage ratio	72
	(b) Increment in power coefficient v/s axial induction factor for a 9% blockage ratio	72
Figure 5.1	Frictional Torque - Dec. 2010	80
Figure 5.2	C_P v/s λ Results Dec. 2010	81
Figure 5.3	α (deg) v/s r/R	83
Figure 5.4	Re v/s r/R	84
Figure 5.5	C_P v/s λ at low water tunnel velocity (rough)	85
Figure 5.6	C_P v/s λ at high water tunnel velocity (rough)	86
Figure 5.7	C_P v/s λ at high water tunnel velocity (smooth)	87

Figure 5.8	C_P v/s λ at high water tunnel velocity, 1.0X and 1.5X smooth blades	88
Figure 5.9	C_L v/s α , forced transition at 0.1 chord	88
Figure 5.10	C_L v/s α , forced transition at 0.3 chord	89
Figure 5.11	C_D v/s C_L xtr=0.1	89
Figure 5.12	C_D v/s C_L xtr=0.3	90
Figure 5.13	C_P v/s λ 1X rough surface blade - correction bounds	90
Figure 5.14	C_P v/s λ 1X smooth surface blade - correction bounds	91
Figure 5.15	C_P v/s λ 1.5X rough surface blade - correction bounds	91
Figure A.1	An energy extracting actuator disk and stream-tube (adapted from the Wind Energy Handbook [1])	101
Figure B.1	Rig structure modelling	107
Figure B.2	Rig structure modelling	108
Figure B.3	Mesh analysis (<i>Model</i> ₁₀)	112
Figure C.1	Numerical processing flow-chart DPIV	115

Nomenclature

Chapter 1

V'	Glauert's equivalent axial freestream velocity
U_F	Bahaj's equivalent open speed
P_{wt}	Power in the water tunnel domain
P_{unb}	Power in the unbounded domain
C	Cross sectional area of the water tunnel
W	Cross sectional area at the far wake
u_i	Axial velocity at location i
p_i	Pressure at location i
U_C	Corrected axial velocity to free stream conditions
$C_{T,wt}$	Thrust coefficient characteristic of water tunnel domain
$C_{T,unb}$	Thrust coefficient characteristic of unbounded domain
$C_{P,wt}$	Power coefficient characteristic of water tunnel domain
$C_{P,unb}$	Power coefficient characteristic of unbounded domain
y_+	Non-dimensional wall distance

Chapter 2

C_P	Power coefficient
λ	Tip speed ratio
ρ	Water density
Ω	Angular velocity
P	Power
R	Radius of the Rotor
U_∞	Axial velocity of the undisturbed free stream
U	Stream velocity
U_0	Axial inflow velocity in the water tunnel
R_w	Radius of the wake expansion
a	Axial induction factor
Re	Reynolds Number
A	Cross sectional area at the disc
T	Thrust force
γ	Angle of Yaw
F_X	Maximum Thrust force aligned to the axis of the turbine
F_Z	Maximum Thrust force orthogonal to the axis of the turbine
σ_{VM}	Von Mises stress
σ_i	Stress in the i direction
$[K]$	Stiffness matrix
θ_i	Mode shape vector
$[M]$	Mass matrix
ω_i^2	Eigenvalue i
Ω_{Ei}	Natural frequency of a structure of mode i
L	Characteristic length
c	Chord length
D	Rotor disc diameter
Re_c	Reynolds Number based on chord length
Re_D	Reynolds Number based on rotor diameter length
$T_{frictional}$	Frictional torque
T_{hydro}	Hydrodynamic torque
T_{react}	Reaction torque

Chapter 3

χ	Momentum sink
C_T	Thrust coefficient
U_0	Axial inflow velocity in the water tunnel
ρ	Water density
t	Thickness of the disc
D	Diameter of the scaled rotor
$K - \Omega$	Equation to model turbulence
Re	Reynolds Number
u	vector velocity
p	pressure
τ	stress tensor
(S_M)	External momentum sources
\mathbf{u}	Turbulent Vector velocity
\bar{u}	Mean velocity
u'	Random velocity fluctuation
K	CFX Momentum Source Coefficient
U_Z	Velocity in the Z axis
U_S	Flow speed in the streamwise direction
$p_{opening}$	Pressure at the Opening boundary surface
p_{spec}	Pressure specified at certain surface
$U_{n,wall}$	Velocity normal to the wall
τ_w	Shear stress
U_{inlet}	Velocity specified at inlet surface
$U_{spec,X}$	X axis velocity component specified at inlet
$U_{spec,Y}$	Y axis velocity component specified at inlet
$U_{spec,Z}$	Z axis velocity component specified at inlet
$p_{average,outlet}$	Average pressure over the outlet surface
U_{wall}	Vector velocity at the wall surface
C_P	Power coefficient
C_T	Thrust coefficient
a	Axial induction factor
y_+	Non-dimensional wall distance
A_{tunnel}	Water tunnel cross sectional area

Chapter 4

C_P	Power coefficient
C_T	Thrust coefficient
a	Axial induction factor
V'	Glauert's equivalent axial freestream velocity
U_0	Axial inflow velocity in the water tunnel
U_C	Corrected axial velocity to free stream conditions
U_F	Bahaj's equivalent open speed
u_i	Axial velocity at location i
p_i	Pressure at location i
$C_{P,unb}$	Power coefficient characteristic of unbounded domain
$C_{P,wt}$	Power coefficient characteristic of water tunnel domain
$C_{T,unb}$	Thrust coefficient characteristic of unbounded domain
$C_{T,wt}$	Thrust coefficient characteristic of water tunnel domain
P_{wt}	Power in the water tunnel domain
P_{unb}	Power in the unbounded domain
C	Cross sectional area of the water tunnel
W	Cross sectional area at the far wake
U_{corr}	CFD corrected axial velocity
K	CFX Momentum Source Coefficient

Chapter 5

P_{wt}	Power in the water tunnel domain
τ_{rotor}	Measured reaction torque
Ω	Angular velocity
$C_{P,wt}$	Power coefficient in water tunnel before correction
ρ	Water density
U_{∞}	Axial velocity of the undisturbed free stream
R	Radius of the Rotor
λ	Tip speed ratio
α	Angle of attack
C_L	Lift coefficient
C_D	Drag coefficient
r	Local position along blade
$UNC.R_X$	Random uncertainty estimation of X measurement
S_X	Standard deviation of the sample X
M	Sample size
UNC	Total uncertainty estimates

ACKNOWLEDGEMENTS

I wish to thank all those who helped me to complete this project and turned this graduate time into a great experience. Without their support this work may not have been possible.

My sincere gratitude to my supervisor *Dr. Curran Crawford*, for his patience, support, and guidance through all the stages in this learning process. I really appreciate the time *Dr. Crawford* spent helping me to develop understanding of my subject of study and helping me to solve practical aspects of my work. I would like to extend my thanks to *Rodney Katz*, *Oleksandr Barannyk*, and *Patrick Chang* for their advice and hands-on help with the practical execution of my experiment; and *Heshan Fernando* for his work on the rig design.

And last but not least, my deepest gratitude goes to *my family* and *Patricio*, for their love and support over all these years.

DEDICATION

To Patricio, for his vision and his encouragement through this journey

Chapter 1

Introduction

As a result of the Kyoto Protocol and the Copenhagen International Conference on Climate Change, several industrialized countries have committed to reduce Green House Gas (GHG) emissions and to increase electricity generation using low-carbon intensive technologies. Consequently, emerging economies have recognized the potential role of renewable energies within a portfolio of electric power generation projects. Research on renewable energy technologies has become a priority in order to develop a cost-competitive green technology capable of providing reliable and predictable access to energy, and allowing countries to reach their GHG reduction targets.

In this context, *kinetic turbines*, as mechanical energy extracting devices, are a choice for environmentally-friendly production of alternative energy in the near future. Wind turbines, tidal turbines and in-stream turbines are the key devices being developed. Although wind turbines are considered a mature technology, already installed in several locations and providing energy to the grid, there is still much research being carried out to better understand the wakes of single devices and turbine arrays. Many studies on blade profiles have been carried out in the aeronautic industry, however to fully understand how blade geometry affects the flow downstream of the rotor, in turn affecting the turbine performance, experimental studies on vortex wakes have been recently performed [2]. A comprehensive summary of several experiments done and numerical studies performed on wind turbines for both near and far wakes is presented by Vermeer and Sorensen [3].

Regarding marine turbines, not much has been established as standard design yet in the industry. The present designs for marine turbines are basically an adaption of conventional wind turbines, taking into account the inherent differences of devices

harnessing the kinetic energy of marine currents instead of air. Comprehensive studies and experiments are required in order to secure and strengthen the application of this technology. As wind turbines are more familiar to the reader, a presentation of tidal turbine technology is presented next, although the experimental rig and techniques developed in this thesis are applicable to all forms of kinetic turbine testing.

1.1 Horizontal Axis Tidal Turbines

Energy from marine currents seems to be a reliable and perhaps more importantly a predictable source of electricity generation [4]. The typical resource referred when talking about marine turbines are the tides, caused by the gravitational forcing of the sun and moon on the oceans. Two other water-based kinetic turbine applications also exist: run-of-river turbines in freely flowing rivers, and ocean-based turbines set in ocean flows largely driven by wind stress, such as the Gulf Stream, or ocean circulation driven by surface heat and freshwater fluxes. In all cases, water-based kinetic turbines offer a higher power density than other types of renewable sources (such as wind). Since it is possible to identify the sites where sea flows are channelled due to topographies, it makes possible to locally study the source itself in order to better predict the energy output.

Since the design of Horizontal Axis Tidal Turbines (HATTs) is an emerging area, and even if the majority of these devices present a conventional design setting a rotating shaft in line with the flowstream, it is possible to find as many different types of turbines as companies getting into the market. HATTs development has widely benefited from the wind industry and their experience with axial rotor machines. In the same way, several companies with tidal stream technologies under development have been strongly influenced by the predominantly open three-bladed rotor design. Other companies have moved to in-stream turbines, taking advantages of flow acceleration [5].

Fig. 1.1 illustrates the mix of technological approaches. Subfigure (a) corresponds to the Tidal Generation Ltd company. The turbine consists of a three-bladed, up-stream pitch controlled rotor, with a drivetrain and power electronics inside the nacelle. A 500 kW prototype is currently operating at the European Marine Energy Centre (EMEC) [6], with a commercial machine rating at 1 MW. Subfigure (b) is a dual two-bladed rotor built by Marine Current Turbine, the biggest HATT installed

in the ocean (Strangford Narrow), generating 1.2 MW. Finally, subfigure (c) displays the Lunar Energy ducted turbine. Ducted turbines have smaller rotor diameters and a shroud that accelerates the incoming flow, with a 500 kW prototype not yet tested in ocean, and a 1 MW device under development [5]. Not shown in figure, Nova Scotia Power has installed a 1 MW in-stream tidal turbine in Minas Passage of the Bay Fundy, to explore the feasibility of harnessing tidal energy on a commercial scale [7].

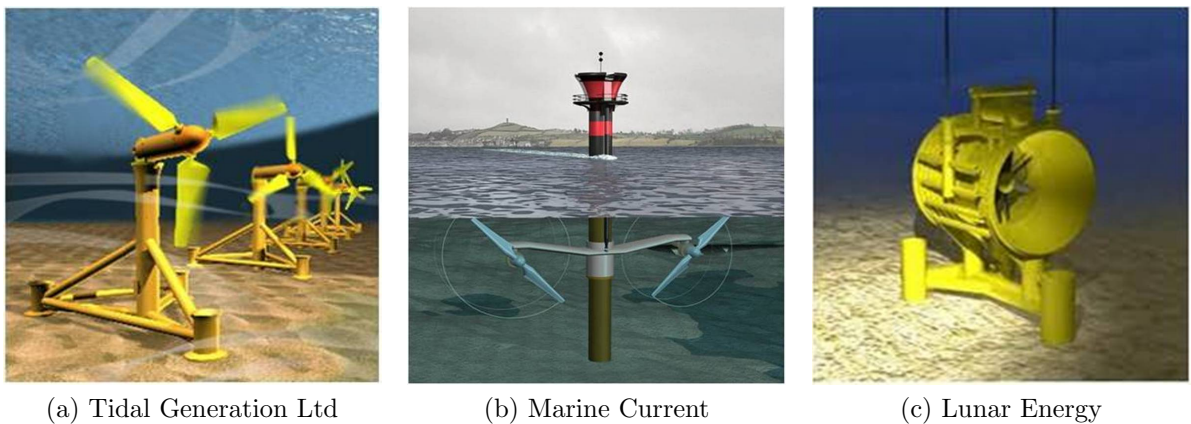


Figure 1.1: Tidal Turbine Industry

1.2 Experimental Kinetic Turbine Rotor Investigations

An important amount of knowledge from wind turbines and classical marine propellers can be applied to the design and operational analysis of marine turbines [1, 8]. However, relevant differences inherent to flow characteristic and fluid properties of marine turbines, such as density, high Reynolds number, viscosity, turbulence, cavitation, etc, must be taken into account in the development processes of these machines. Continued experimental investigation is required to validate prediction codes and designs in this field, as well as that of wind turbines, for which experimental data is also sparse.

1.2.1 Previous Test Campaigns

There have been efforts done to characterize the performance of marine extracting energy devices and evaluate the energy resources [9, 10]. The following section presents a summary of the most relevant test campaign performed so far in this area.

Two physical tests were carried out at the University of Edinburgh [11, 12] for validation of numerical simulations of energy extraction based on the actuator disk concept. The testing considered several operational conditions for different disk porosities with free surface. It was found good agreement between numerical simulations of wake velocity and experimental data. This led to the conclusion that numerical models can outline first results regarding wake development downstream of turbines.

A contra-rotating tidal turbine of 0.8 m rotor diameter (1/30th scale) was designed and tested at the University of Strathclyde, UK [13]. The results of this laboratory testing were used for the design and construction of a prototype of 2.5 m diameter to be tested in the open ocean, to finally become a grid-connected device.

Related to industry development, a scaled model of a commercial turbine was tested in a circulating channel at Southampton University to verify power output prediction [14]. The horizontal axis turbine model had a 0.4 m diameter (1/30th scale), and experimental data was acquired for varied channel flow speeds, blade pitch angles, and rotor speed and yaw angle. The results obtained were compared to a commercial Blade Element Momentum Theory (BEM) computer package, where it was found that measured power output was higher than the simulated values for high angles of attack. Moreover, Bahaj [15] carried out experimental studies on a 0.8 m diameter Marine Current Turbine model in a cavitation tunnel and tank test. It was found that interference between the twin rotors was not significant, providing also useful information for the hydrodynamic design and experimental data for numerical model simulations, such as C_P vs λ performance curves.

Measurements on water surface elevation have also been performed to explore blockage-type effects taking place around rotors. Investigation of a 0.4 m diameter rotor shown exaggerated water level variation [16], however the author pointed out that a reasonable variation in flow level and velocity should be expected in a full scale array. This experimental investigation highlighted the relevance of estimating optimal cross-sectional area versus power output of turbines (array) within a constrained area, such as a channel. Another testing project to explore turbine interaction was developed at University of Strathclyde [17]. Different array configurations of two-

bladed rotors of 25 cm diameter were tested at a towing tank having a maximum velocity of 0.47 m/s. A significant power output reduction was found for in-line turbine arrays, however an optimal array configuration was found that optimized energy production, heading for an array efficiency of 100 %.

At this point, we can recognize that more experimental data is needed to validate designs and simulations for emerging HATT. All types of kinetic turbine designs (including wind turbines) can benefit from experimental studies.

1.2.2 Blockage effects

A common issue that arises in this type of experimental testing is that Reynolds similitude is improved with larger scale models. Fortuitously, the behaviour of rotor wake vorticity is relatively insensitive to Reynolds number [3]. However, for a larger ratio of the rotor swept area to the tunnel section area, the greater the associated error due to blockage. Consequently, larger models less accurately predict the performance of the full scale turbine. Physically, the walls of the water tunnel constrain the flow and cause an increment in the velocity around the rotor, compared to the inlet velocity.

A simple model of the turbine takes the rotor as a thin disc plane that extracts energy from the stream as the flow passes through it. This approach is known as the actuator disc concept, and is explained in Appendix A. The energy extraction done by the turbine implies a drop in static pressure in the area right after the disc plane, which downstream causes a reduction in the velocity and cross sectional area expansion of the streamtube through the rotor.

This situation is depicted in Fig. 1.2a, if the turbine is placed in an unbounded domain. It is assumed that flow at constant pressure p_0 surrounds the stream-tube and the flow velocity remains undisturbed U_0 everywhere outside the stream-tube surrounding the disk. Conversely, if the turbine is placed in a constrained domain, such as in a water tunnel section as shown in Fig. 1.2b, there is a change in the velocity and pressure that surround the stream-tube compared to the far upstream (undisturbed) conditions. This effect leads to higher forces and power outputs measured in the bounded domain relative to unbounded flow conditions around the real machine. Conversely to propeller testing which create contracting wakes, this block-

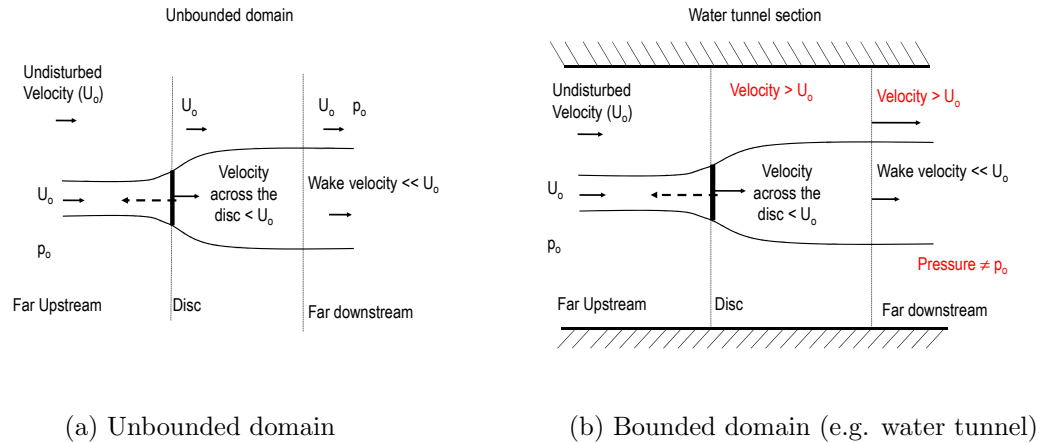


Figure 1.2: Actuator disk concept in open and bounded flows

age is not negligible for kinetic turbines which extract energy from the flow and cause flow expansion in the wake behind the rotor.

In the past decades, several efforts have been made to provide a suitable methodology to correct for wind and water tunnel blockage effects [18–20]. To date, these methods have been based on the axial momentum theory representing this tunnel interference by an equivalent free stream velocity. Analytical expressions correlating this equivalent open flow velocity to thrust coefficient are used to correct the characteristic power coefficient, and consequently real power output [15, 18–21]. However, the validity of these analytic corrections as the blockage ratio, the turbulence level, and rotor loads increase, has not been clearly defined. These factors might affect the flow field in the water tunnel used in the current work in such a way that the assumptions from which the analytical corrections were derived are not longer valid. Additionally, the need for a new post processing methodology arises when thrust data is not available in the experimental testing. In the current work, due to the small size of the rotors, it is impractical to measure with any accuracy the thrust force of the rotor itself.

1.3 Motivation and Contributions

The purpose of this thesis research was to build a rig and develop associated testing methods for the physical testing of scaled models of kinetic turbines in an existing

water tunnel facility. The experimental information generated by the testing could then be used for turbine performance assessment, rotor design efforts, and validation of numerical prediction codes. The rig was intentionally designed for small rotors, so that many blade sets could quickly be produced using Fused Deposition Modeling (FDM), a rapid prototyping technique producing Acrylonitrile-Butadiene-Styrene (ABS) or polycarbonate parts in 3D, thereby allowing the testing of a wide range of rotors to produce a rich set of data. Any scaled model has limitations due to the scaled physics of the facilities and rig, as well as the attainable accuracy of the instruments used for measurement. This project therefore focused specifically on developing a precision testing rig with the capability to properly scale operational conditions of real machines.

The experimental study described in this work includes the use of Particle Image Velocimetry (PIV) techniques to obtain quantitative information about the vector flow field at the rotor plane and upstream/downstream. Flow measurements are obtained at various rotor azimuthal positions at the same time that power measurement are taken. The intention is to use this information in future studies in order to validate potential flow and Computational Fluid Dynamics (CFD) simulations that resolve wake features.

It is important to note that accurate thrust force measurements are not possible for the size of the scale model built. Since PIV data will be available from the experiment anyway, a novel actuator-disk CFD-PIV methodology was developed to post-process the measured experimental data to properly account for tunnel blockage effects in the absence of thrust measurements [22, 23].

Although not detailed in this thesis, the CFD simulation modelling approach was also applied to a study [24] looking at recommended testing procedures for full-scale turbines *in-situ*. In particular, the study looked at blockage effects in comparison between various modelling approaches including complete CFD with explicit resolution of the blades. Recommendations were supplied to the authors of tidal turbine testing standards currently in development related to acceptable testing parameters to avoid erroneous performance estimates through testing in constrained conditions.

Unfortunately, the water tunnel PIV equipment was broken for an extended period covering the entire latter half of the thesis period, and therefore only an initial mechanical measurement test campaign can be presented in this thesis as an initial application of the rig. Progress was also delayed by a broken torque transducer which

had to be returned to the UK for servicing after a difficult fault-diagnosis process. In addition, a problem with the driving stepper motor causing pull-out and severe vibration that was only finally resolved by replacing the motor.

1.4 Thesis Outline

This thesis consist of five chapters, organized as follows. Chapter 2 details the mechanical design of the rig focused on ensuring accurate measurements could be taken with the forces involved, and that PIV data could be gathered through a range of operating conditions. Chapter 3 presents the CFD simulations used to study rotor behaviour in unbounded and bounded domains, leading to the work presented in Chapter 4 carried out to deal with tunnel blockage effects. Chapter 5 then presents the initial experimental campaigns carried out to test the operation of the rig, in the absence of PIV measurements due to protracted equipment breakdown. Finally, Chapter 6 summaries the work and provides direction for follow-on use of the rig once the PIV system is operational.

Chapter 2

Rig Design

This chapter describes the main aspects that were involved in the mechanical design of an experimental apparatus for the investigation of the hydrodynamic performance of kinetic turbines. The rig was initially developed with a view to testing HATT. The model parameters were therefore sized to scale down a typical HATT device of 17 m diameter full size, which is expected to generate about 1 MW if is placed in a free stream of maximum velocity of 3 m/s when rotating at approximately 20 Revolutions per Minute (RPM).

It is of particular interest to accurately estimate the dimensionless coefficients that characterize the hydrodynamic performance of these types of turbines. The focus of the experimental design is therefore on power output measurements. Obtaining quantitative information of the flow field in the near wake, which is approximately up to one rotor diameter downstream [3], is the other primary objective, as this data can be used to directly validate CFD and potential-flow simulation codes. The latter directly simulate vorticity (wake) evolution, making experimental validation with PIV-derived wake trajectories very useful.

The final testing rig design enables measurement of the reaction torque of the rotor under different inflow tunnel velocities and rotational speeds. The output power can then be calculated as a function of the operational conditions. In addition, the rig design leaves an area free from obstruction (undisturbed flow) in the near wake downstream the rotor for the quantitative study of the flow field. Within this undisturbed section, the velocity field will be estimated using PIV techniques, which also provides the information required to post process the measured torque data and to validate numerical prediction codes [23].

This chapter is comprised of the following sections:

- Section 2.1 introduces the water tunnel facility.
- Section 2.2 details the scaling parameters used to determine the appropriate physical size for the models, an estimation of the forces in the system, and testing requirements. These serve as a set of requirements for the mechanical design of the scaled-model.
- Section 2.3 presents the Finite Element Method (FEM) for the mechanical rig design, including static deflection and modal analyses carried out to determine the minimum size of the main parts of the rig.
- Section 2.4 presents the mechanical rig design including a description of the mechanical components, features, and capabilities of the finalized testing rig design.

2.1 Water Tunnel Facility

The water tunnel shown in Fig. 2.1 utilized in the current study at the University of Victoria (UVic) is a model 504 25 cm re-circulating type from Engineering Laboratory Design, INC.



Figure 2.1: Water tunnel facility

It is composed of a test section, a filtering station in line, and a circulating pump system with variable speed. The water tunnel has an interior cross sectional area of

45 cm width by 45 cm depth, and 2.5 m of working length. The sidewalls and floor of the test section are fabricated of clear transparent acrylic. The tunnel usually is typically operated with a free surface for ease of use, but an acrylic cover is available to close the working section and allow for flow through the full section with slight pressurization. A maximum flow speed of 2 m/s can be reached in this setup, and 1 m/s in the open configuration. For this experiment, the tunnel will operate fully enclosed, so that higher flow speeds can be used, increasing the model Reynolds numbers and providing higher forces to maximize the signal to noise ratio of the measurements. The flow depth is also maximized to avoid free-surface and blockage effects to the greatest extent possible in the testing facility.

2.2 Scaling Parameters

The analysis and design of HATTs is a new area of endeavour, however the basic flow physics are quite similar to that of Horizontal Axis Wind Turbines (HAWTs). Considering these similarities, it is possible to apply the simple momentum and blade element theories used for wind turbines [3] to the modelling of tidal turbines and power output estimation.

Wind turbine performance is typically described in a non-dimensional manner in terms of the power coefficient C_P as a function of the tip speed ratio λ . A Buckingham's Pi theory applied to turbine parameters leads to the result that these two dimensionless groups are the key non-dimensional parameters to define a rotor's performance. λ is defined as the ratio of the rotor rotational speed times the blade tip radius to the free-stream velocity, as shown in Eq. (2.1), where Ω is the rotor angular velocity.

$$\lambda = \frac{\Omega R}{U} \quad (2.1)$$

The power coefficient C_P is defined as the ratio of the power extracted to the power available in the stream that goes through the rotor area, as shown in Eq. (2.2).

$$C_P = \frac{P}{1/2\rho U_\infty^3 \pi R^2} \quad (2.2)$$

where P is the power extracted by the rotor, ρ is the density of the fluid, U_∞ is the velocity of the undisturbed free stream, and R is the radius of the rotor. The theoretical maximum value for the power coefficient is given by the Betz limit, $C_P = 0.593$ for conventional wind turbines [1]. Based on tidal and wind turbine similarities, this expression will be utilized for the performance study of tidal turbines.

For the primary scaling parameter of the tidal turbine device, the tip speed ratio λ will be used. It is well known in the wind industry that there is an optimal λ range, for a given number of blades, that maximizes the power extraction of HAWTs. Thus, for future design applications of HATTs it is desirable to identify and compare the optimal operational range to that of HAWTs.

The scaled turbine will be tested across a range of tip speed ratios λ in the range of 2-8 corresponding to maximum power production [1, 2, 15]. Since the maximum inlet velocity in the tunnel facility U_0 is 2 m/s, the turbine must have an angular velocity high enough to fit the operational testing conditions. In other words, given the operational testing conditions, the rotational speed of the scaled model will be directly related to rotor diameter chosen for the model.

The Reynolds number is a dimensionless coefficient that quantifies the relative importance of inertial forces relative to viscous forces. It is generally defined as given in Eq. (2.3), where ρ is the density for the fluid, U stands for stream velocity, and L for a characteristic length scale or dimension of the model being studied.

$$Re = \frac{\rho U L}{\mu} \quad (2.3)$$

For this work, two Re are calculated based on different characteristic dimensions: a Re_c based on airfoil chord length (c) to characterize the airfoil section (see Chapter 5); and a Re_D based on rotor disc diameter (D) used in the CFD simulations in Chapter 3. Equations (2.4) and Eq. (2.5) define Re_c and Re_D respectively.

$$Re_c = \frac{\rho U c}{\mu} \quad (2.4)$$

$$Re_D = \frac{\rho U D}{\mu} \quad (2.5)$$

Reynolds number similitude is impossible at the model scale desired for the water tunnel facility, while Froude number scaling is not required as the water tunnel will be operated in a fully-enclosed and pressurized mode with no free surface. Re_c similitude is obviously important for proper scaling of effects local to the rotor blades, in particular separation and lift/drag curve slopes for the airfoils. It should be noted that in the case of bluff bodies, there is typically a distinctive C_D-Re_A ¹ relationship that has sharply defined Re_A ranges. However, what is important to remember is that for the streamlined airfoil shapes used in the experiments there is not as dramatic a change in lift and drag characteristics with Re_c . Of course there will be changes associated with varying Re_c in terms of laminar or turbulent separation and associated viscous and pressure drag, but these are more smoothly varying with Re_c and the drag coefficient of bluff bodies with Re_A . In any case, the actual airfoil coefficients seen at the small model scale will be determined in a separate experimental campaign to properly account for varying Re_c effects.

Additionally, the underlying assumption adopted is that once the flow has left the blade and forms the wake, the evolution of the wake is Reynolds (Re_D independent [3]). It is the wake properties that dominate the flow conditions seen at the blade, and hence the experiments will properly scale these velocities.

2.2.1 Rotor Size

In order to best represent the full-size turbine and minimize the errors associated with scaling phenomena, it is desirable to have the largest model rotor size as possible, but this also introduces errors due to physical blockages of the flow. Because rotor inflow and the wake structures are mutually related [3], the performance of the rotor will be affected by any changes in free wake expansion. Indeed, there is a trade off between the larger models' higher Reynolds numbers and the induced blockage errors. Thus, the ratio of the the area swept by the rotor to testing tunnel area is a key variable to choose.

¹Where A is the frontal area of the bluff body

In this section, a simple approach is used to determine the optimal size of the turbine model. Based on the actuator disc concept [1], explained in Appendix A, the rotor of the turbine is modelled as a thin disc that causes a drop in pressure as the flow goes through it. In ideal conditions in an open flow, the kinetic turbine acts like an extracting energy device, causing the flow to reduce its velocity when approaching the disc. The disc exerts a pressure drop in the flow as it passes through the disk, and downstream of the disc there is region that remains at reduced pressure and reduced velocity, the so called the wake region. The theory assumes that eventually viscous mixing returns the wake to the freestream velocity very far downstream.² Because of mass conservation, there is a flow expansion after the disc, as seen in Fig. 2.2.

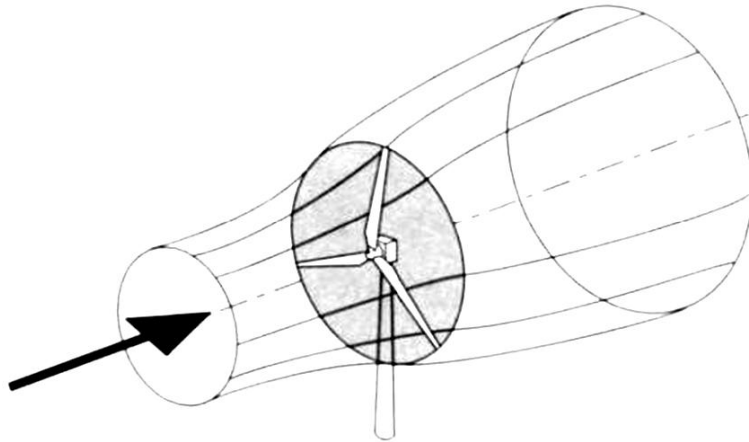


Figure 2.2: The energy extracting stream-tube of a wind turbine (adapted from [1])

This approach makes it possible to obtain a simple expression that relates the area of the streamtube required for the wake region, the rotor size, and the flow speed variation induced by the disc on the free stream velocity. This induced velocity in the stream wise direction is referred to as the axial induction factor $a = 1 - u_d/U_\infty$, where u_d is the axial velocity at the disc location, and U_∞ the undisturbed velocity far upstream.

²This is of course an assumption of an infinite domain to re-energize the downstream flow.

Equation (2.6) presents a simple correlation between the size of the rotor (R), the radius of the wake (R_w), and the axial induction factor a . This expression is derived from equations Eq. (A.1), Eq. (A.2), and Eq. (A.8) detailed in Appendix A.

$$R_w = \sqrt{\frac{R^2(1-a)}{1-2a}} \quad (2.6)$$

Equation Eq. (2.6) gives a rough reference to estimate the maximum rotor diameter of the model if we limit the wake tube radius expansion to the cross section of the water tunnel facility. It is assumed that the turbine will operate at optimal conditions to maximize output power, which corresponds to an axial induction factor a equal to 1/3 in ideal, unbounded flow conditions [1]. For a tunnel section of cross sectional area of 45x45 cm, the rotor radius obtained for the model turned out to be approximately 15 cm.

Summarizing the scaling conditions, the following table Table 2.1 shows a comparison between the full scale turbine and the model for the HATT experiment.

Variables	Full Size Turbine	Scaled Model
Rotor diameter [m]	17.5	0.15
Maximum axial flow velocity [m/s]	3	2
Rotational speed [RPM]	10 – 30	500 – 1500
Tip speed ratio λ	3 – 10	2 – 9
Typical blade chord Reynolds number [Re_c]	10^7	10^5

Table 2.1: Full size tidal turbine versus scaled model

The full scale turbine operates with a maximum flow speed of 3 m/s³, and the tunnel facility has a maximum inlet flow speed of 2 m/s. It is seen that the range of tip speed ratio λ is similar for both operational cases, but is not possible to match the Reynolds number (Re_c).

The momentum theory was used as a first approach to determined the maximum rotor size of the model, however the wall of the water tunnel produces several effects in the scaled-model that are not found in an unbounded flowstream. Rae and Pope [25]

³Although tidal flows can be above 5 m/s, 3 m/s is a typical tidal inflow velocity.

listed nine effects for the case of general wind tunnel testing. The two most important factors related to experiments to study the wake structure [2, 26] and power output measurement [15] are the so-called solid blockage and wake blockage. These two blockage effects occur when the walls of the tunnel confine the flow around a model in the test section, reducing the area through which the fluid must flow as compared to the free unbounded conditions. This effect increases the velocity of the fluid as it flows in the vicinity of the model, causing an increment in dynamic pressure which affects all the hydrodynamic forces measured. This blockage effect adds error to the measurements which must be corrected. A simple rule of thumb suggested by Rae and Pope [25] indicates that the maximum ratio of frontal model to test-section cross sectional area should be 7.5% to minimize errors. In Chapters 4 and 3 a more exact method is presented to correct for the tunnel effects associated with wake blockage.

2.2.2 Force Estimation

Based on the momentum theory, the maximum thrust force at the rotor plane can be estimated as the pressure drop across the rotor area times the rotor area [1]. If the rotor axis is aligned with the incoming flow in steady conditions, the thrust force can be expressed in terms of fluid density (ρ), undisturbed free stream velocity (U_∞), rotor area (A), and axial induction factor a , and the thrust force (T) as given in Eq. (2.7).

$$T = 2\rho AU_\infty^2 a(1 - a) \quad (2.7)$$

Tidal turbines are not perfectly aligned with the flow direction and so maintain steady yawed operational conditions most of the time. It has been determined for wind turbines that the yawed rotor decreases its efficiency of energy production compared to the non-yawed rotor [1], thus it is important to consider the assessment of yawed rotor behaviour in terms of efficiency of energy generation.

The momentum theory has limited applications for force estimation in yawed conditions, however this approach is good enough for the purposes of estimating the maximum forces to be exerted on the rotor. If the rotor is held at an angle of yaw γ to the steady fluid direction, the thrust force can be expressed in terms of the fluid

density (ρ), undisturbed free-stream velocity (U_∞), rotor swept area (A), yawed angle (γ) and axial induction factor(a) as in Eq. (2.8).

$$T = \rho A U_\infty^2 2a(\cos \gamma - a) \quad (2.8)$$

where the optimal condition is given for $a = \frac{\cos \gamma}{3}$.

Appendix A provides more details about the momentum theory for a turbine rotor in steady yawed conditions. The following Table 2.2 presents the summary of the resultant maximum forces calculated at the rotor plane based on the actuator disc concept. These were used as inputs to the FEM model developed next in §2.3. F_X represents the thrust force aligned to the axis of the turbine, and F_Z the thrust force orthogonal to the axis of the turbine.

Plane of the rotor w.r.t. the inflow direction (degrees)	F_X [N]	F_Z [N]
90	31.32	0
105	28.22	7.56
145	11.08	11.08

Table 2.2: Forces at the rotor plane

Note that testing in a water tunnel leads to forces approximately an order of magnitude higher than if the same-sized model was tested in a wind tunnel. This is a result of the kinematic viscosity being an order of magnitude smaller for water, but the density being three orders of magnitude larger, and assuming the model is run at the same tip speed ratio but the wind tunnel speeds are an order of magnitude larger than water tunnel speeds. These larger forces are advantageous in terms of force measurement sensitivity for small-scale models, but are challenging in that as described in §2.4 in order to control the rotor the instrument package must be out of the tunnel to physically accommodate the required hardware. It is also interesting to note, that given the same assumptions, the Reynolds number local to the blade chords is approximately the same for wind and water tunnel-based testing of identically sized rotors.

2.3 Finite Element Method (FEM) Modelling

The testing rig basically consists of a three-bladed rotor attached to a main horizontal shaft which drives the rotor, driven by a belt carried up through a vertical support tube. The horizontal and vertical tubes that compose the support-structure are made of aluminum tubing and are submerged in the water tunnel so that the motor and instruments of the system are placed outside the water, on top of the cover of the water tunnel, as shown Fig. 2.3. The scaled rotor has a diameter of approximately 15 cm, and it will be placed at half of the water tunnel height (25 cm). Since the vertical tube (main upright) should be positioned as far downstream of the rotor location as possible, in order to minimize the disturbance in the near wake, the length of the horizontal tubing (the sting) was expected to be between the 20 and 30 cm. This corresponds to a number of complete wake revolutions downstream of the rotor that could be characterized using PIV.

Several configurations of lengths, diameter and wall thicknesses for the tubing support-structure were evaluated using ANSYS 11.0 in order to determine the minimum possible sizes for the tubes. A structural static analysis was performed on the loaded structure to estimate the maximum deflections. The intent was to have a rigid structure so that aero and hydrodynamic validation could be carried out without confusing the picture with coupled aero/hydro-elastic deformations. In addition, a modal analysis was performed to obtain the natural frequencies in order to compare with the external frequency imposed on the system by the rotor rotation. Details of the FEM modelling, such as geometry and property materials, can be found in Appendix B.

Once the minimum allowable sizes for the main tube components were determined, the mechanical components of the model were chosen based on testing requirement and availability in the market. The detailed drawings needed for fabrication, summarized in the §2.4, were developed by a co-op student, Heshan Fernando [27].

2.3.1 Failure Criteria and Maximum Deflection

The maximum deflection accepted for the final design is restricted to 1.5 mm for yawed conditions, and limited to a maximum value of 1 mm for the case of the rotor plane facing the inflow orthogonally. The von Mises stresses available in ANSYS [28] were used in the evaluation of failure for the tubing-material. The von Mises stress is

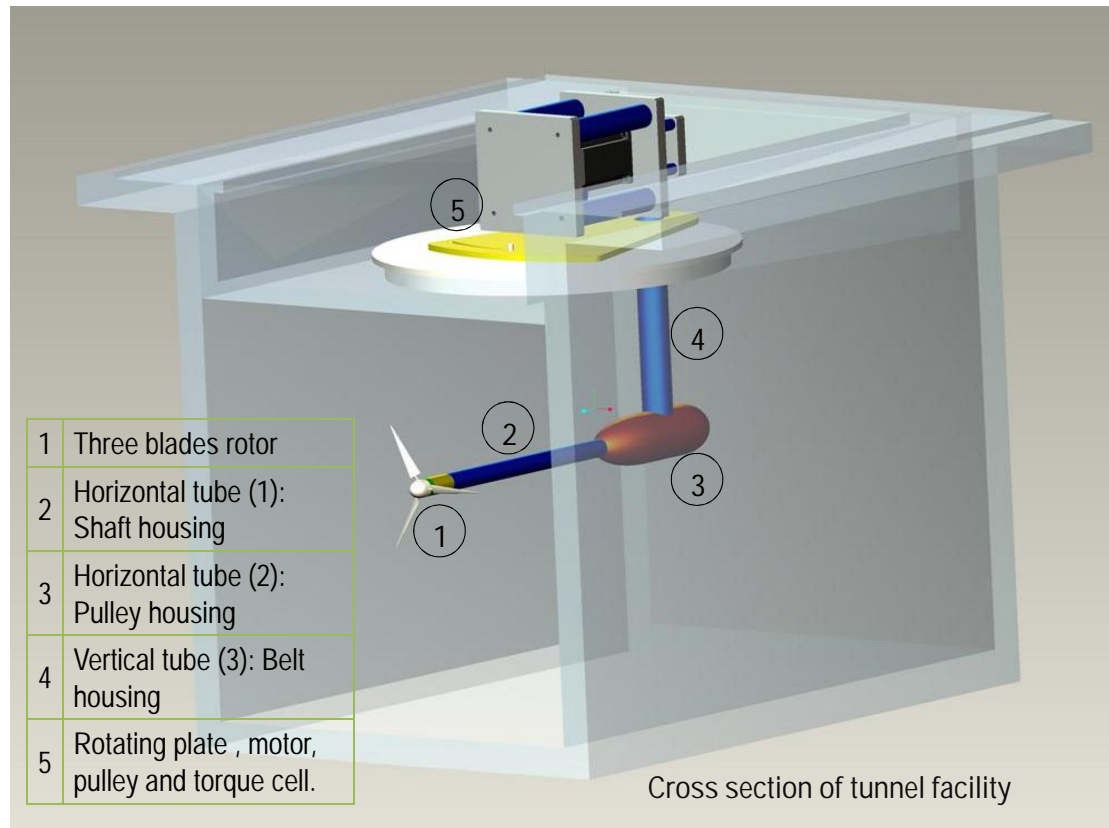


Figure 2.3: Schematic of the testing rig

essentially an equivalent tensile stress value computed from the stress tensor that can be compared to the yield strength of the material to predict yielding under a specific loading condition [29].

The von Mises stress (σ_{VM}) is related to the principal stresses (σ_1, σ_2 , and σ_3) by the following expression:

$$\sigma_{VM} = \frac{1}{\sqrt{2}} \sqrt{(\sigma_1 - \sigma_2)^2 + (\sigma_2 - \sigma_3)^2 + (\sigma_3 - \sigma_1)^2} \quad (2.9)$$

The yield strength of pure aluminum is 7-11 MPa, while aluminum alloys have yield strengths ranging from 200 MPa to 600 MPa. For this model a value of 200 MPa was used as the design yield strength.

2.3.2 Modal Analysis

A modal analysis was performed to determine the natural frequencies and mode shapes of the support structure [30]. The purpose of this analysis was to determine vibration characteristics of the testing rig structure in order to avoid coupling with the spinning turbine blades while performing the experiments. In this particular model, neither pres-stress nor damping was computed.

The basic equation solved in typical modal analysis without damping is the classical eigenvalue problem:

$$[K]\theta_i = \omega_i^2[M]\theta_i \quad (2.10)$$

where $[K]$ is the stiffness matrix of the structure, θ_i is the eigenvector (mode shape) of mode i , $[M]$ is the mass matrix, and ω_i is the eigenvalue (natural frequency) of mode i . The modal analysis is solved using the consistent mass matrix. The natural frequencies and mode shapes are equivalent to the solution of an eigenvalue problem. Depending on the computation of damping and the resulting system matrices the numerical effort to solve the eigenvalue problem may vary.

ANSYS provides a number of different eigenvalue solver options [31]. To solve the eigenvalue problem the Block Lanczos Method was chosen. It is a fast and robust algorithm and used for most applications as the default solver. It is recommended when finding many modes, or when the model consists of mainly solid elements [28].

2.3.3 Summary of the FEM Results

Ten different configurations of tube length and wall thickness were defined and computed in the analysis ($Model_1$ to $Model_{10}$). Table B.1 in Appendix B presents the detailed dimension for the 10 configurations, where $Tube_1$ is the horizontal tube that houses the rotating shaft; $Tube_3$ is the vertical tube that houses the vertical belt; and $Tube_2$ is the short tube that houses the pulley and connects $Tube_1$ to $Tube_3$ as shown in Fig. 2.4.

$Tube_3$ did not vary its length since the rotor must be placed at the half-height of the tunnel depth, however wall thicknesses between 0.058 in and 0.12 in are considered in the analysis. The same was true for $tube_2$ of length 5 cm and thickness between

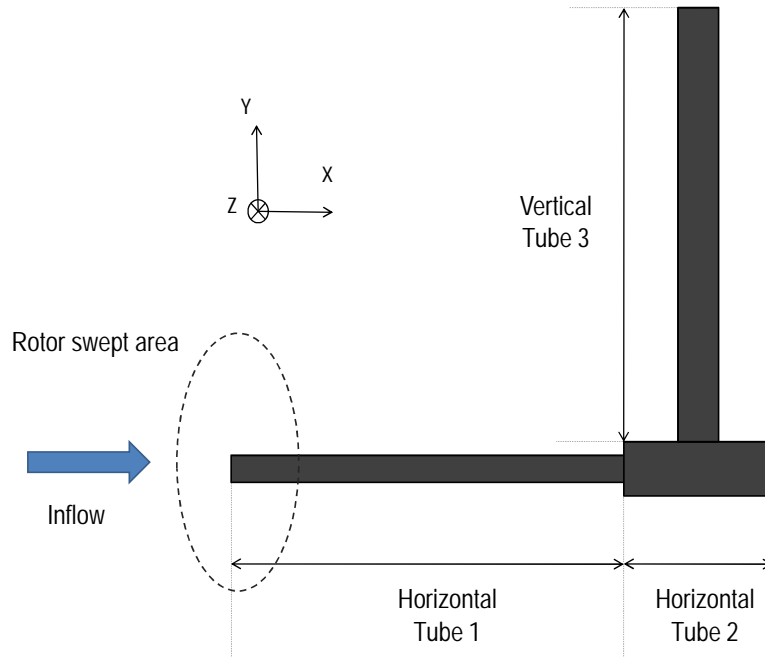


Figure 2.4: FEM tube model of the testing rig

0.058 and 0.12 in. $Tube_1$ varied its length between 20 and 30 cm and wall thickness between 0.058 and 0.12 in.

The results of the static analyses are provided in Appendix B, displayed in Table B.2 to Table B.5. In the first model simulations, only four of the ten models ($Model_7$, $Model_8$, $Model_9$, and $Model_{10}$) achieved maximum deflections within the threshold value set up for the design. Based on this static analysis, the minimum diameter for the horizontal tube that houses the spinning shaft ($Tube_1$, the sting) was 1/2 in with a minimum wall thickness of 0.065 in. The minimum diameter of the vertical tube that houses the belt ($Tube_3$) was found to be 3/4 in with a minimum wall thickness of 0.12 in; and the minimum diameter of the shortest tube that houses the pulley ($tube_2$) is 3/4 in with a minimum wall thickness of 0.065 in.

The modal analysis was then computed for the selected models, and the first 10 modes extracted for the system composed of the three tubes and a mass representing the rotor, as shown in Appendix B, Fig. B.1.

External forcing vibration frequency will be applied to the system due to the rotating set of blades, during the testing. The rotor will spin in the range of 500 to 1500 RPM, which means frequencies in the range of 8.33 and 25 rev/s. To avoid vibration coupling, the natural frequencies obtained in this modal analysis were compared to the frequencies associated with the operational conditions of the rotor. Details of this analysis is presented in Appendix B, where in Table B.5 it is seen that natural frequencies are higher than the external frequencies for *Model*₅ to *Model*₁₀. Since at the time this modal analysis was done the final design was not yet finished, the most robust and heavier structure (*Model*₁₀) was chosen for determining the minimum diameters and wall thickness of the tubes that compose the structure. The modal analysis results of *Model*₁₀ allowed variation in the rig design without the risk of increasing significantly the mass of the system and consequently decreasing the characteristic vibration frequency of the structure.

The maximum length of *Tube*₁, and recommended minimum thickness and diameter for all the tubes that composed the rig structure are summarized in Table 2.3.

Dimension	<i>Tube</i> ₁	<i>Tube</i> ₂	<i>Tube</i> ₃
Length [mm]	20	25	5
Diameter [in]	0.75	0.75	0.12
Thickness [in]	0.12	0.12	0.12

Table 2.3: Dimensions resulting from FEM analysis

2.4 Mechanical Design

This section presents a summarized description of the mechanical components that compose the rig mechanical design. Detailed information is found in Fernando’s report [27].

There were four main objectives that the testing rig design had to meet:

1. It must fit into a existing facility: the water tunnel of cross sectional area of 45 by 45 cm and height of 25 cm.

2. The driving system should provide speed control in order to measure power output for different operational controlled conditions.

It is important to notice that frictional forces are not negligible for this model size. The mechanical components of the rig, such as seals, bearings, belt, shaft, etc, exert frictional forces and torque ($T_{frictional}$) on the system, which could be of the same order of magnitude as the hydrodynamic torque expected to be measured from the rotor. Moreover, depending on the operational conditions it is possible that the frictional torque is greater than the hydrodynamic torque exerted by the fluid on the rotor. To better understating of this situation, Fig. 2.5 shows a schematic of the externally applied torques identified in the rig system.

The instrument load cell is attached to the case of the motor which runs the system. The motor drives the belt which in turn drives the rotating shaft and the rotor attached to it. T_{hydro} is the hydrodynamic torque exerted by the flow-stream on the system, $T_{frictional}$ is the torque due to static and dynamic frictional forces of the mechanical components, and $T_{reaction}$ is the reaction torque at the motor, read by the load cell, corresponding to the difference between of hydrodynamic and frictional torque, $T_{reaction} = T_{hydro} - T_{frictional}$.

Summarizing, a motor/generator (as opposed to simply a generator) is required to overcome friction and to properly control the turbine when $T_{frictional} > T_{hydro}$. Additionally, accurate control of the angular position of the rotor was required for PIV post-processing phase/azimuthal correlation between blade and wake positions.

3. The rig must have an area behind the spinning rotor where the disturbance of the flow, due to the supports, is minimal. A distance of one to two rotor diameters was imposed as a requirement for the horizontal tube that houses the rotating shaft for this purpose.
4. The rig must allow testing in yawed flow conditions. For that, a yaw system is required up to 45° , ideally maintaining the rotor in the center of the tunnel to avoid wall interference effects.

The main components of the final design are shown in Fig. 2.6. The top plates, located on top of the cover of the water tunnel (as shown in Fig. 2.3) contain the

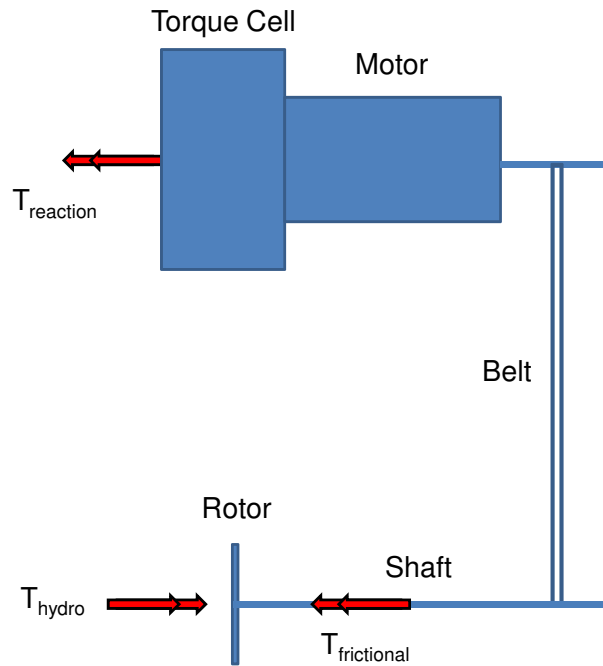


Figure 2.5: Schematic operation

instrument structure and the yaw system. The instrument structure consist of a torque cell and the stepper motor that drives the system. The yaw system consists of two plates attached to the hatch that can rotate and adjust position of the submersed structure. The submersed structure is composed of several parts: the horizontal rotating shaft and its housing tube, the rotor, the fairings that reduce the disturbance of the flow, and the belt system and its corresponding housing tubes. The motor drives the belt system which is connected to the rotating shaft which in turn drives and controls the speed of the rotor.

2.4.1 Instrument Structure

Figure 2.7 presents a schematic of the instrument structure.

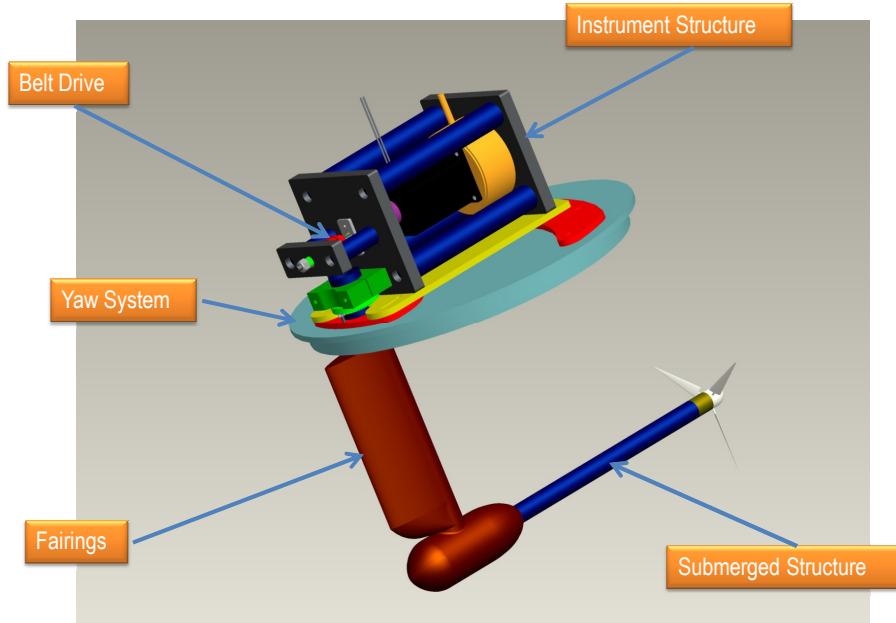


Figure 2.6: Key components of the rig

Plates and posts compose the structure that houses the motor and torque cell. The torque cell is attached to one plate; the motor is attached to the torque cell and a flexible coupler attaches the output shaft of the motor to the pulley shafts that drives the belt system. Bearings are used to minimize the friction, and a clamp attaches the vertical tube support of the submerged structure to the instrument structure. Since the measurements must be very precise, alignment is critical for this design. The plates and posts are accurately machined to meet these requirements. Holes are made on the plate that accurately mate with bosses machined on the posts. Further details of the motor and instruments are provided in Chapter 5.

2.4.2 Belt System

In order to minimize the friction of the rotating components, a belt was chosen to drive the submerged rotating shaft (which runs the rotor). This option has less friction than

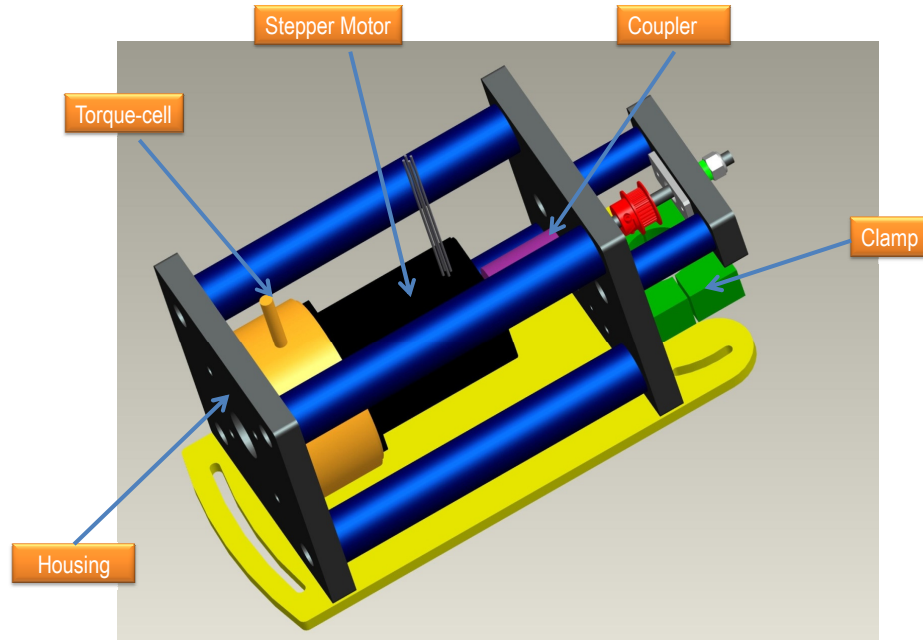


Figure 2.7: Components of the instrument structure

using a rotating gear system. The spinning rotor will reach high rotational speed, up to 1500 RPM, which can lead to additional vibration in the system. To check this design choice, a rig for belt testing was fabricated before carrying out the final design of the testing rig.

To assess two different belt options, and to check the level of vibration of the system in the range of rotational speeds considered for the final experiment, belt testing was performed in this early design stage. The belts were ordered from SDP/SI products; Table 2.4 presents the characteristics of the two belts tested [32]. Pulleys were also ordered from SDP/SI, each type corresponding to the belt model.

The rig designed for the belt testing had a support structure made of two plywood platforms and two aluminum posts, as shown in Figure 2.8. The mechanical components for the testing were the motor, the belt, two pulleys (one attached to the output shaft of the motor and the other located in the lower platform), and a bearing system that houses a free-spinning shaft located in the lower platform. It was



Figure 2.8: Rig for belt testing

possible to adjust the location of the motor in the vertical plane by fastening four screws, which provided the tension required for the belt to work properly. The test was run for rotational speeds in the range of 60 RPM to 1500 RPM.

As a result of this testing, vibrations were noticed only at very low speeds, below 500 RPM. The belt type MXL ran smoother than the belt type GT3; this may be because belt type GT3 was found to be stiffer than belt type MXL. In addition, the pulley corresponding to belt GT3 used a set screw to attach to the output shaft of the motor, what caused slight damage to the shaft, whereas pulley of belt MXL had a clamp. In conclusion, belt MXL was chosen for the final testing rig.

Model number	Material body	Material cord	Pitch length [in]	No of. grooves
MXL A6G16-350025	polyurethane	polyester	28	350
GT3 A6R53M250060	nylon covered fiber-glass reinforced	polyester	29.5	250

Table 2.4: Characteristics of the candidate belts

2.4.3 Submersed Structure

The submerged structure is composed of a rotor, a sting, a connecting part, a vertical tube, and a set of fairings, as shown Figure 2.9. The aim of this particular design was to make the components of this structure as small as possible to avoid blockage effects and flow disturbances. In addition, the sting had to be as long as possible in order to provide an undisturbed area behind the rotor for the PIV images to be taken.

The sting is the part that houses the rotating shaft which is attached to the rotor. This assembly part is made of aluminum tube of 0.75 in external diameter, and has two press-fitted pieces at each end, one of them containing threads that attach this structure to the connecting piece.

The connecting piece connects the sting assembly and the vertical tube which suspends the submerged structure from the rig-plates. This connecting piece is made of aluminum and has an overall outside diameter of 2 in. It was not possible to make this piece smaller since it has to provide sufficient room to locate the pulley that drives the shaft inside this connecting piece. For the sting assembly to be attached and aligned to this connecting piece, a bore and threads were designed in the front part.

There is a vertical tube that houses the belt which compose the rig drive system. The vertical tube, made of stainless steal of 1.25 in diameter, connects the submerged structure to the upper instrument structure, and keeps the sting assembly at the center of the vertical tunnel cross-section. A flange is welded at the bottom of the tube to secure it by screws to the connecting piece.

The blades and hub that composed the three-blade rotor design are fabricated in the SSDLs lab, using the FDM machine as described in section next.

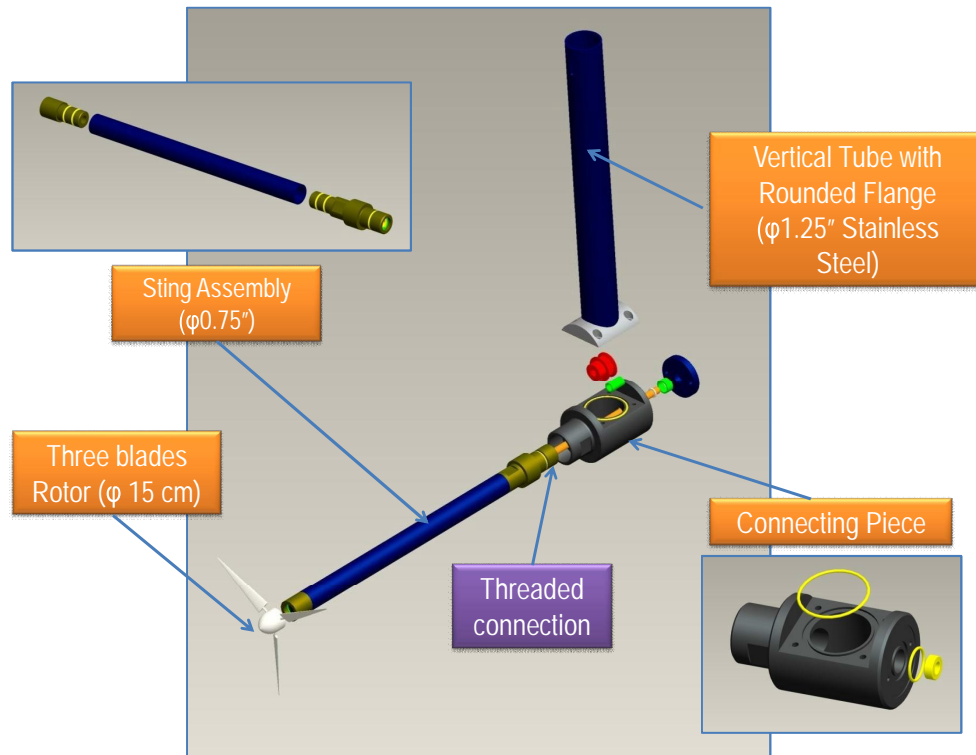


Figure 2.9: Submerged support structure

In addition to all the structural parts that compose the underwater structure, there are fairings incorporated into the rig design with the purpose of reducing flow turbulence and drag as the water passes the submerged assembly.

As shown in Figure 2.10, there are two main fairings: one covers the vertical tube and the other covers the connecting piece. The vertical fairing slides over the vertical tube; the tolerances in this design also allow aligning the fairing to the flow for the yawed position of the rig. The fairing which covers the connecting pieces is fabricated as two split halves. Tolerances in the design allow the fairing part to slide over the sting and rear part of the connecting piece, and help to keep the fairings attached to the structure. The split parts clip together in the middle, and they are also secured by the vertical fairing which slides over a vertical extrusion of the connecting piece fairing.

An important consideration in the rig design was to ensure the drive system worked under dry conditions. Different type of seals were used to prevent water from leaking

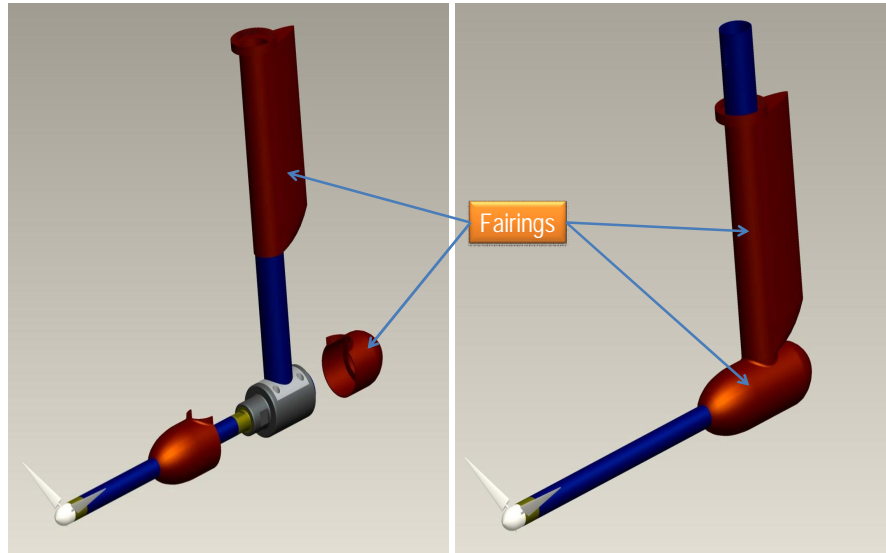


Figure 2.10: Model of fairings covering the submerged structure

inside the underwater structure. O-rings and grooves were placed between two mating surfaces or press-fitted pieces, and lip seals were used to prevent water entering around the rotating surfaces like the rotating shaft in the sting.

Finally, notice that three axial bearings were used in this design to align and minimize the friction for the rotating shaft. There are two bearings on the sting, and a third bearing placed in the rear part of the connecting piece

2.4.4 The Rotor

A 3D material printer available in the Sustainable System Development Lab (SSDL) using FDM techniques was utilized for building the rotor blades (and a number of fairings and other parts of the rig). This technology allows construction in-house of several parts in a short period of time. Then, different blade profiles and sizes can be tried in the ongoing and future experiments. A wide range of thermoplastics with different mechanical properties can be used as printing material; ABS and Polycarbonate (PC) thermoplastics were available for building the parts.

Depending on the material employed, it is possible to accurately manufacture small parts by extruding material into layers as thin as 0.005 in thickness (T10 tip).

For the first set of blades the material used was PC, and the T12 tip was used which creates a layer 0.007 in thick. Build time and part finish are proportional to the tip size used.

The 3D printer, a Fortus 400mc, works with the *Insight* software. This application, installed on the user's work station, allows setting up the properties of the parts to be printed, such as surface smoothness, layer path, filling spaces, void volume, etc.

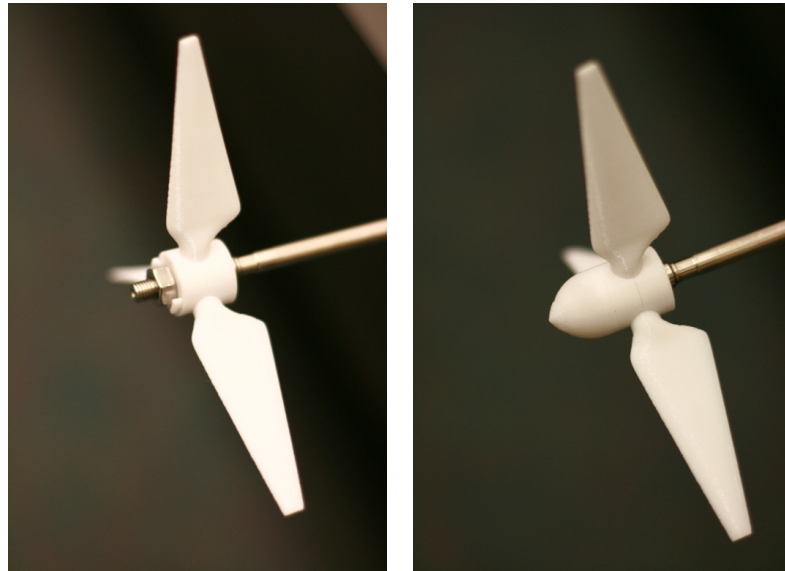


Figure 2.11: Rotor assembly

Figure 2.11 shows the blades and hub parts that were made separately and then assembled together. The upstream end of the rotating shaft has a boss to prevent the hub part from touching the sting assembly (Fig. 2.9) and to align the hub part with the submerged structure. It also has threads allowing the hub-part to be secured against the shaft.

The three blades have identical profile, are about 70 mm long, 25 mm wide at the root, and 7 mm wide at the tip of the blade. The root part has a circular plate plane orthogonal to the span-wise axis, which is used to keep the blade clamped between the two-half hub parts. The hub part is composed of two cylindrical parts meant to clamp the blades and to provide pitch adjustment. A hexagonal nut is used to secure the hub against the shaft boss. The nose cone is attached to the hub part covering the hex-nut.

The initial set of blades built correspond to a NACA63(2)-4XX airfoil profile, with 21 % thickness, and a twist angle of 15° . This relatively large thickness airfoil was used to ensure blade rigidity.

2.4.5 Yaw System

The yaw system works due to the motion of two concentric planes of rotation: the plane of the instrument structure plate, and the circular rotating plate. The former has an axis of rotation about the vertical support tube, and the latter about the water tunnel cover cutout hole.

As shown in Fig. 2.6, the vertical tube which holds the submerged assembly is clamped to the instrument structure. This instrument structure is placed above the circular rotating plate, and secured to the plate by screws. The circular rotating plate is seated on a hole made in the cover of the water tunnel, and is kept attached to the hatch by six clamping pieces and 24 screws.

Figure 2.12 demonstrates the yaw motion for the rig. The starting point is shown in the scheme number 1 of the reference figure. First the circular plate rotates, generating rotation of the the instrument structure, the vertical tube clamped to it, and all the submerged structure attached, as shown in part 2 of the figure. Then, the angle of the sting can be adjusted by rotating the instrument structures plate, as shows part 3 of the figure. In such a way, it is possible to get different yaw angles but keep the rotor at the center of the cross-section of the water tunnel.

Marks for the degree movements are included for both the rotating circular plate as well as the base plate of the instrument structure. The maximum yaw angle obtainable with the original rig design, with a sting of 13.25 in length, is about 23° . It is possible to reach 45° if the sting assembly is replaced for a shorter one of 7.42 in length. In the end, two different sting assemblies were built allowing different yaw capabilities for the final testing rig. At present, the yaw system is actuated manually and fixed during testing. In the future, this system could be automated to enable dynamic yaw event testing.

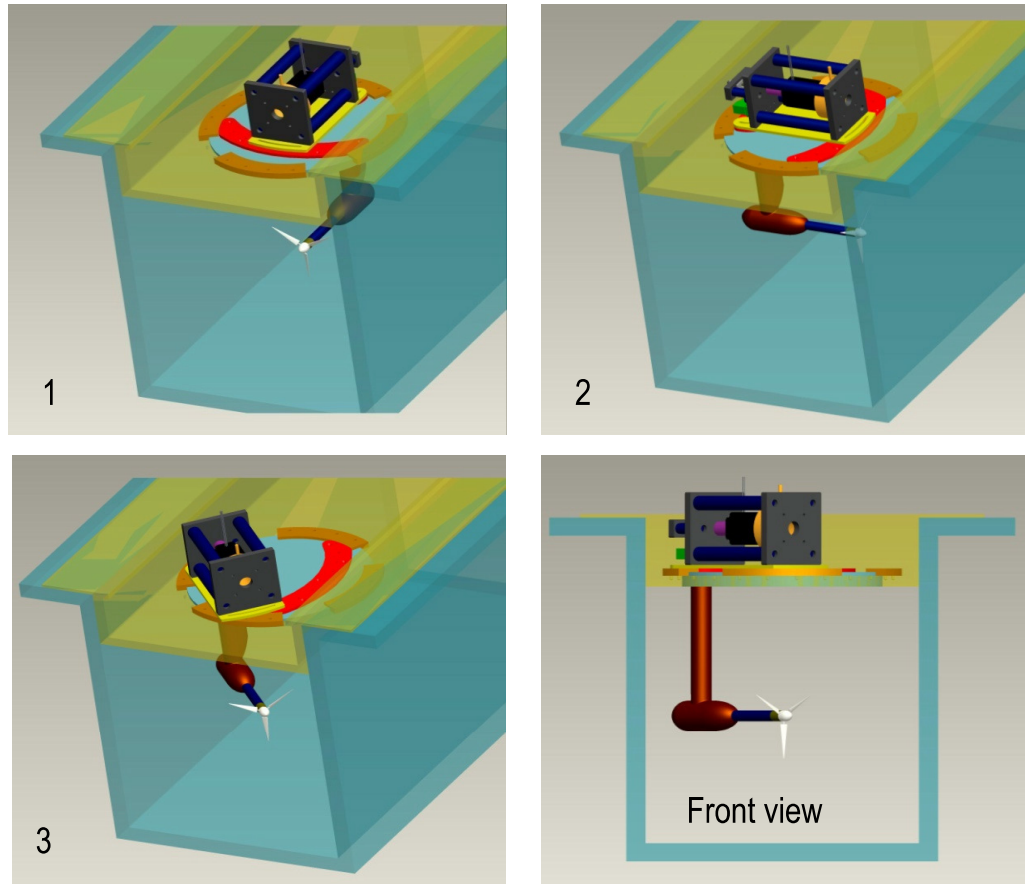


Figure 2.12: Yaw system operation

2.5 Instrumentation

The general layout of the complete rig and PIV system is depicted in Fig. 2.13.⁴ There are two acrylic hatches that cover the water tunnel at the upper surface allowing the section to operate closed instead of having a free surface. As described in §2.4.3, the whole instrument and drive system is kept outside the water tunnel. The rotor is located at the center of the section to minimize wall effect over the measurements.

The DPIV system is comprised of a camera and a laser sheet, and will be used to illuminate a horizontal plane and capture the particle images in the near wake. The area of interest is located behind the rotor up to a few diameters downstream.

⁴The terms Digital Particle Image Velocimetry (DPIV) and PIV as used in this thesis both strictly refer to a DPIV system, as the images are digitally acquired and processed.

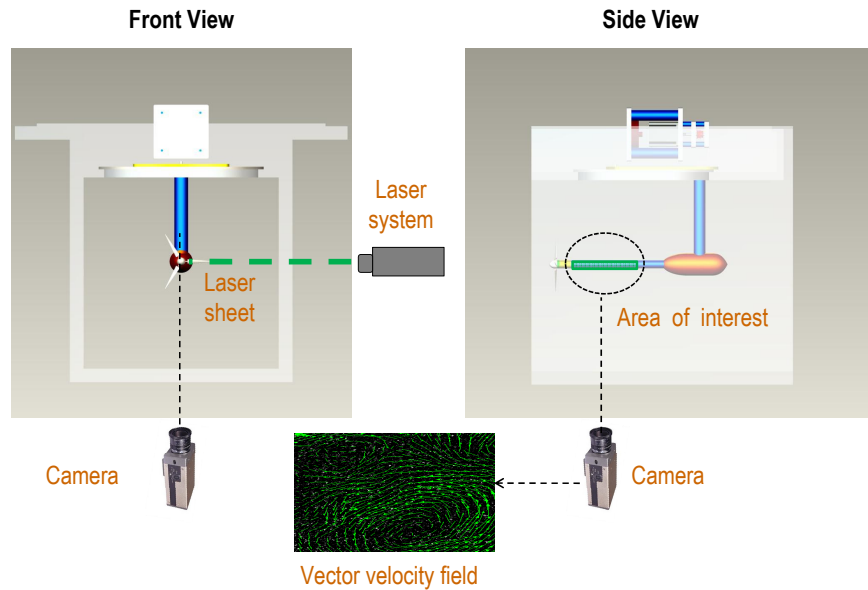


Figure 2.13: PIV system layout

The X - Y plane is parallel to the bottom and roof of the water tunnel, the flow is in the X axis direction, from left to right, and the Z -axis points upward. The laser sheet illumination is the X - Y plane, and the camera is located perpendicular to the illumination plane looking upwards. This general layout is meant to avoid, or at least minimize, shadows in the wake. When illuminating the same plane from the bottom, the vertical tube, that contains the shaft, will probably generate shadows in the area of study. On the other hand, this vertical tube will be positioned as far aft the rotor as is possible in order to minimize the disturbance in the near wake.

The interactions among the components of the integrated electric system that control the experiment are shown in Fig. 2.14. The main components of the integrated system are:

- The rotor itself, imparting torque on the shaft. This torque is transmitted to the drive system by the rotating shaft and belt system.
- The drive system, which runs the rotor, comprised of a stepper motor and the E-AC Driver.

- The Data Acquisition System (DAQ) system is composed of the instrument to measure the torque of the motor, the loadcell, and by the control and data acquisition system, the NI CompactRio hardware. The CompactRio technology is a real time acquisition system which allows control of the drive system, triggers the PIV system to start, and stores all the information acquired. LabView, installed on a user computer, provides a user interface for the DAQ system. Through this software it is possible to display the information being acquired and command the motor velocity and direction, and to start and stop the system.
- The PIV system is an independent piece of hardware with its own controller system and storage capacity. It cannot be commanded by the CompactRio directly to take a picture, but it can be triggered to start operation. It is composed of a laser, a digital camera, and operating software, LaVision. The laser system was the component that was broken during most of the thesis period and precluded operation of the PIV for the trial runs of the rig discussed in Chapter 5.

2.5.1 The Drive System

In order to meet the objectives of the experiment, it was important to have control over the operational conditions of the turbine. It was also desirable to be able to control the rotational position of the rotor, and minimize the number of components and electric equipment working within the system.

Stepper motors allow precise positioning and speed control without the use of encoder or feedback sensors. The stepper motor and the drive selected allows the shaft to move only a set number of degrees when each pulse is delivered by the drive. The stepper motor HV233 and the E-AC 120 *VAC* Microstepping Drive from Parker were chosen as the drive system, as shown in Fig. 2.15. The E-AC Microstepping Drive can be plugged directly into the standard mains supply (ranging between 95 to 132 *VAC*), and can be integrated to the Compact Rio technology control.

BEM simulation runs for comparison to the experimental results were typically done setting an angular accuracy of 5 °. Consequently, providing rotor control with the best angular accuracy is desirable for measurement and comparison. In others words, given the accuracy required on angular position, a restriction on the minimum

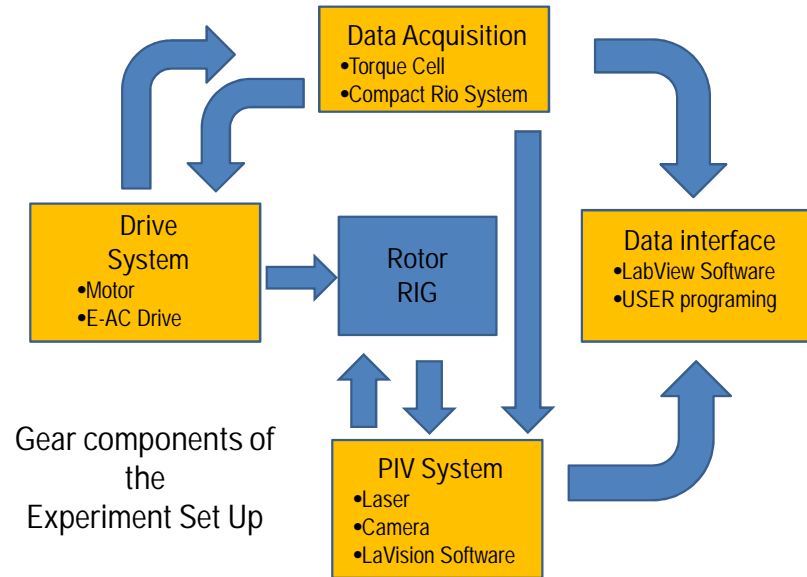


Figure 2.14: Experiment system schematic

resolution was set up for the drive system selection in order to meet these requirements. The drive system chosen satisfied the technical conditions specified, having a resolution of 50,800 steps per revolution, with an error of 3 % to 5 % per step non-cumulative from one step to another, an accuracy of 5.003° can be reached, with an error of $\pm 0.000354^\circ$.

Figure 2.16 shows the performance curve of the motor obtained for the rig, a double shaft HV-233 stepper motor. It provides the maximum torque estimated (0.9 Nm) for operation at 500 RPMs (8.3 revolutions per second) and a wide range of rotational speeds.

2.5.2 The Motor

A motor device is essential to control operational conditions, to keep the λ value within the range established. Also, the testing rig has an inherent friction due to the belt components and bearings, and thus a motor device is necessary to overcome frictional losses. In such a manner, the motor is working as a device that can absorb

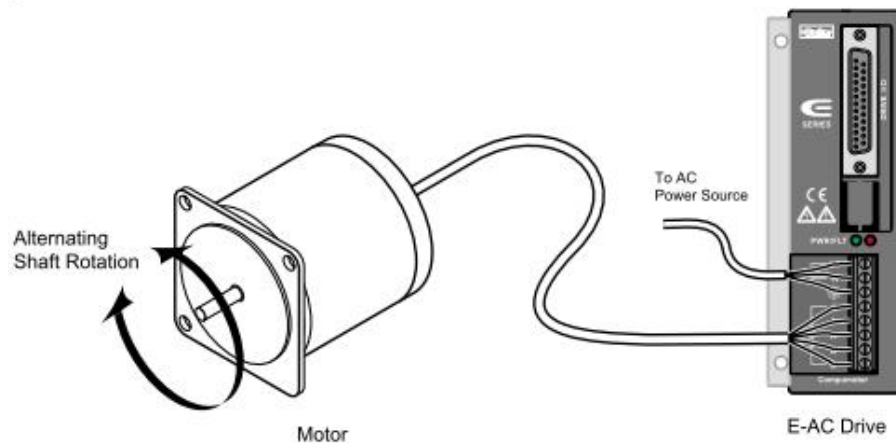


Figure 2.15: Drive system

and provide power, and that allows the net torque of the rotor minus all the losses in the drivetrain to be determined.

In retrospect, while the stepper motor is advantageous in providing speed and position control without feedback, two issues were found in practise. In order to attain the required torques, the coils were connected in series, but this caused the motor to overheat when run longer than 10-20 minutes. In addition, the first motor obtained had some flaw that caused stalling even in no-load conditions. The situation was hard to address, even after multiple attempts at ensuring alignment of matings surfaces, etc. Again, this greatly delayed the experiments, and eventually lead to replacement of the first motor. Perhaps a better approach for future rigs would be a servomotor with encoder feedback positions, although high-accuracy encoders for fine knowledge and control of azimuthal position could be challenging to obtain.

2.5.3 Torque cell

Notice that for small scale models, accurate force measurement is extremely difficult to achieve due to the level of noise in the signals, thus only torque measurement was feasibly for this study. Thrust force measurement was considered, but was considered impractical given the other constraints of the system and the primary requirement for excellent torque and azimuthal position control.

The Novatech *F326-Z* 1 Nm loadcell was chosen to measure the reaction torque of the motor. This type of loadcell fits between a motor and its mounting structure act-

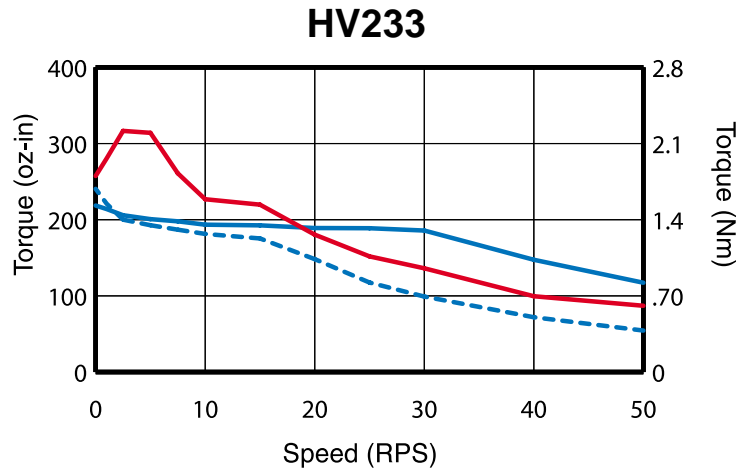


Figure 2.16: Performance curve Parker Motor HV233

ing as a coupling. Novatech proposed two options for the F326-Z mounting, Fig. 2.17, for this rig. The configurations suggested are meant to support the motor weight and remove any extraneous forces and bending moments, if the mounting structure and bearings for shaft supports are properly aligned. At one side of the loadcell, four screws are used to fasten the motor to the torque cell structure so that the motor's torque is transmitted to the F326. This flanged mounted motor torque transducer has a hole through the axial centre of the structure, which allows the motor shaft to pass through it. On the other side of the loadcell another four screws are used to fasten the loadcell to the instrument rig structure. The rig instrument structure follows the first scheme of Fig. 2.17 (single shaft mounting), but utilizing a double shaft motor as described in §2.4. The reaction torque is therefore measured between the case and mounting (earth) structure.

With respect to the torque range measurement and its resolution, the loadcell has the capability to measure torques ranging -1 Nm to +1 Nm, and read values as small as the minimum expected torque for the experiment, which is 0.01 Nm, providing the DAQ electronics components can handle the small signal of 60 μV .

The F326-Z loadcell has a nominal output of 0.6 mV/V, which basically determined the selection of DAQ CompactRio module in charge of torque measurement. Given the minimum torque value to be read (i.e 0.01 Nm), and a 10 volt excitation voltage for the torque cell, this specific DAQ module must be capable of reading a small signal of 60 μV .

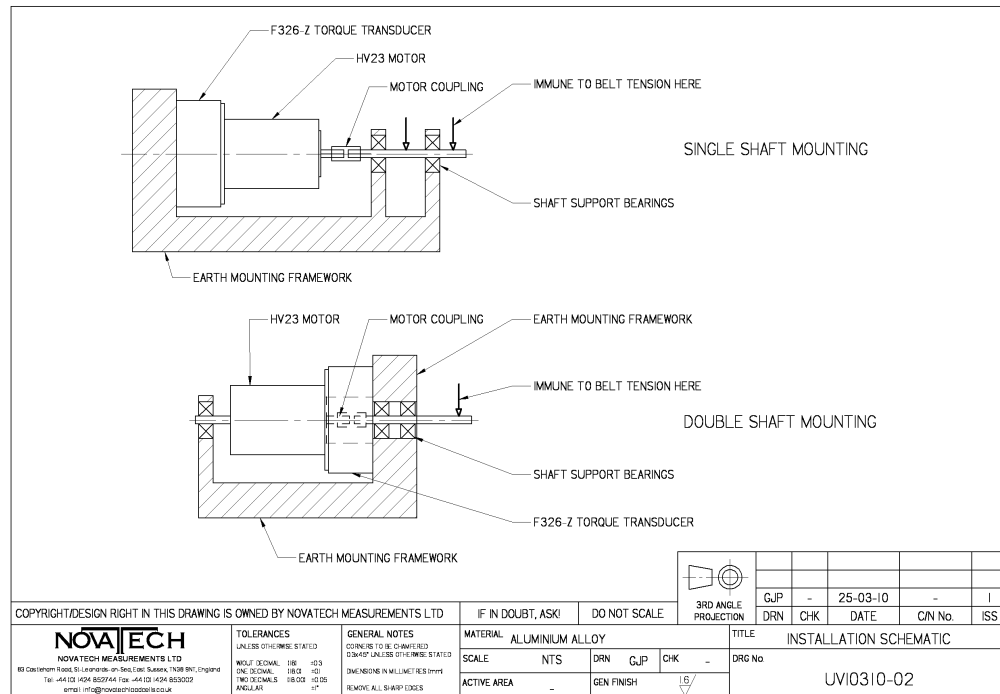


Figure 2.17: Novatech installation schematic

For this reason we looked at a 16 bit minimum DAQ module for torque measurement. A module of less *bits* of resolution would not be capable to handle that small voltage value, and hence it would not provide enough resolution for measurement.

During initial testing, one or more leads internal to the load cell broke for some reason. The loadcell was not overloaded, and hence the structure was intact and only the leads required reattachment by the manufacturer. However, as the vendor was in the UK, this breakdown again set the project back.

2.5.4 PIV system

The acquisition of the vector velocity field that characterizes the near wake will be done using DPIV, which is the most suitable flow visualization technique for the measurement of velocity fields over a two-dimensional region of flow [33]. PIV is an optical method used to obtain instantaneous velocity measurements, and since

optical measurements avoid the need for Pitot tubes, hotwires or other physical flow measurement probes which cause disturbance of the flow field, this method has the advantage of being a non intrusive measurement technique.

The fluid is seeded with tracer particles which are supposed to cause negligible distortion of the fluid flow. These particles have to be carefully chosen depending of the type of fluid and motion to follow the flow dynamics. For this particular experiment, Mearlin Supersparks particles were available with mean diameters in the range of 5 to 7 μm and silver in colour. The specific gravity of these particles is larger than specific gravity of water, thus they are deposited on the bottom of the channel when the water tunnel is off. However, it is possible to infer from others' experiments carried out in the same tunnel facility and having the same type of particles [34], that the flow speed considered for this particular experiment is high enough to keep the particles following the motion of the flow field.

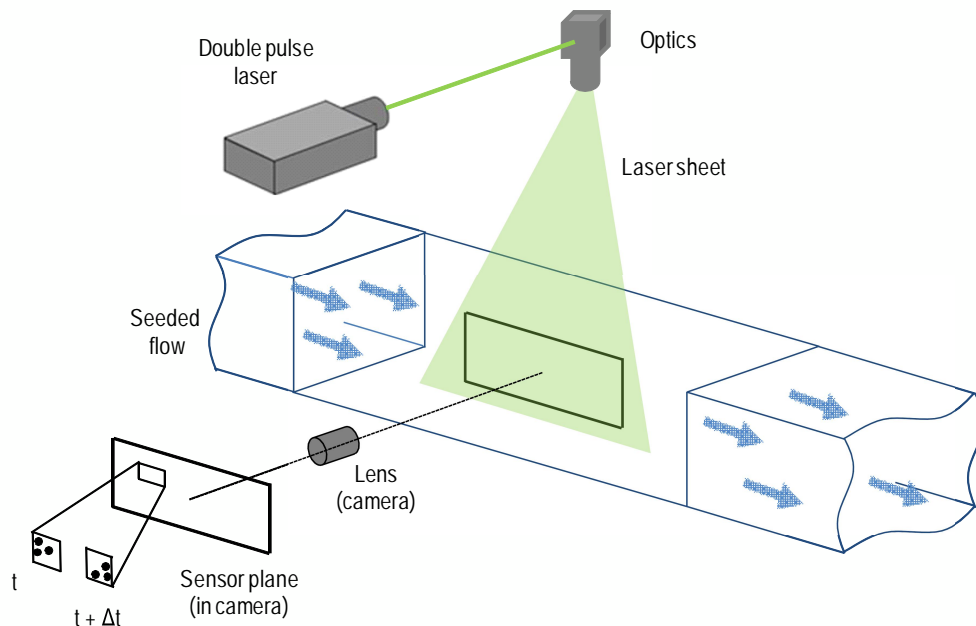


Figure 2.18: General schematics of PIV system

Notice that it is the motion of these tracer particles that makes visible the fluid motion. By recording the position of them at different instances of time, is possible

to determine the displacement of the particles in this time interval, and to calculate its velocity, and eventually build up the flow velocity field.

To capture the image of displacement of the tracers, typically DPIV uses digital cameras with frame rates on the order of 15 - 30 Frames per Second (FPS). To freeze the movement of the particles at specific time, a laser pulse of light is used to illuminate the plane of motion. In this way, the sensor of the digital camera is able to capture the movement of the small particles. Finally, the images taken are processed in a computer to reconstruct the whole velocity field. The schematics of this technique is presented in Fig. 2.18.

There are some factors relevant the DPIV measurement technique, such as timing of the camera shooting, laser pulse, and the size of the interrogation cell. For instance, to get accurate measurements it is crucial to synchronize the camera shutters and laser pulse. Also, the size of the interrogation cell (typically size 6x6 pixels) will depend on the conditions of the flow to be measured. Ideally there are between 3 and 15 particles per area of interrogation. Thus depending on the seeding density, the size of the seeding particle, and the velocity of the flow field, there is a cell size that satisfies that ideal condition and this must be set up for each particular experiment event (a trial and error process). More detailed information about PIV theory is given in Appendix C.

For this particular experiment, in an attempt to reconstitute the 3D velocity fields, PIV images are intended to be taken for a set of different azimuthal planes, each one representing a cross-section of the wake [2]. It is important to notice that PIV images are basically 2D, in this case taken at the plane parallel to the inflow velocity. The set of azimuthal planes are obtained by triggering the camera to take single 2D pictures at different timings relative to the rotor, in such a way that each picture will capture the instantaneous flow velocity corresponding to the vertical position of the blades set at different angles. This will also allow for azimuthally averaged flow quantities to be computed.

The available PIV equipment in the Fluid Lab consisted of a high speed digital camera, a Quantronix Nd:YLF laser, and a PC with hardware for DPIV image data acquisition. For the experiment, the task is to the synchronize the PIV recording equipment with a defined angular position of the rotor, in order to obtain flow photographs at any predetermined position of the blades. This was the primary reason for selection of a stepper motor, and a control system able to trigger the PIV image

recording.

The Darwin-Duo laser series, a 25 mJ Nd:YLF dual diode-pumped type, can be externally triggered via TTL Inputs in such way that the PIV hardware starts the laser operation. At each input signal, the laser provide two laser pulses, having a pulse width of 120 ns and a frequency ranging between 0.1 to 10 kHz. This allows control of the time intervals between each of them with a resolution of 25 ns, and a timing jitter below 2 ns.

The laser optics provides a planar light sheet to illuminate the particles in the region of interest. The digital camera is a HighSpeedStar *HSS* – 5 CMOS sensor with frames rates up to 250 kHz, a maximum resolution of 1024x1024 pixel for a frame rate of 3 kHz and below, and a minimum interframe time of 2 μ s.

The images taken are sent to the software LaVision DaVis 7.2 for data processing. Within the software the recorded images are evaluated by cross-correlating pairs of frame, each containing single exposure of the group of markers (This PIV technique is detailed in Appendix C).

Basically, the required settings for recording images are previously set up in the DPIV PC Hardware, such as pixel size, frequency of image capture, etc. There is a time delay between the starting time of the laser and the moment the camera capture the first picture. Thus, there is also a set time delay before the camera starts in order to synchronize with the laser pulses. Finally, the external trigger starts the DPIV hardware, which triggers the laser and the image acquisition.

Ideally the whole system can be programed to capture an image every turn of the rotor at specific position. However, because of the high rotation speed of the scale model rotor, it is probable that the camera must be set up to capture the images every two or three turns. The final frequency and operation of this integrated system must be adjusted in a trial an error exercise once the PIV system is again operational.

2.5.5 DAQ Rio System

The NI CompactRio package was selected as a combined control and DAQ system. This technology is portable, it communicates over the network, contains a real-time processor, a reconfigurable field-programmable gate array (FPGA), and a variety of analog and digital input/output modules to cover the requirements for the experi-

ments. Each of the NI modules of the CRio package connects directly to sensors, motors, etc, to customize the system architecture.



Figure 2.19: CompactRio package

The National Instruments (NI) package acquired for the experiment, Fig. 2.19, is mainly composed of:

- NI cRio-9022, an embedded real time controller with 533 MHz processor, 2 GB storage for logging data, and 256 MB of memory RAM.
- NI 9401 module, an 8 channel TTL digital input/output signal component. This module outputs the digital signal to trigger the DPIV system.
- NI 9237 24 bit module for load/pressure/strain/torque measurements. The selection of this module is due to its capability and resolution to read the torque cell output voltage measured for the smallest value of torque expected, 0.010 Nm. Thus, for a 10 volt excitation voltage, a $60 \mu\text{V}$ signal has to be handled for the NI module. This task is accomplished by this 24 bits resolution module. The NI 9237 can also output up to 10 V excitation, and has four simultaneous input sampled at up to 50 kS/s per channel, allowing for future expansion.
- NI 9201 8 channel analog input module, which reads the output analog signal of each laser pulse fired.

- NI 9512 stepper drive interface module. This module is probably the most complex of the package. It has its own power supply, and acts as the controller of the drive system. This module makes it possible to control rotation speed and direction of the motor when running, without the need to stop the movement. It also allows moving the rotor in discrete steps.
- NI LabView software, a graphical tool developed by NI can be installed in the user's laptop for designing, prototyping, and deploying embedded applications. The control software for the entire system was implemented in LabView. Figure 2.20 depicts a screen shot of the developed LabView interface software. The figure displays the basic functions programmed such as velocity control, data recording onset, PIV triggering option, data position display, torque measured display, etc.

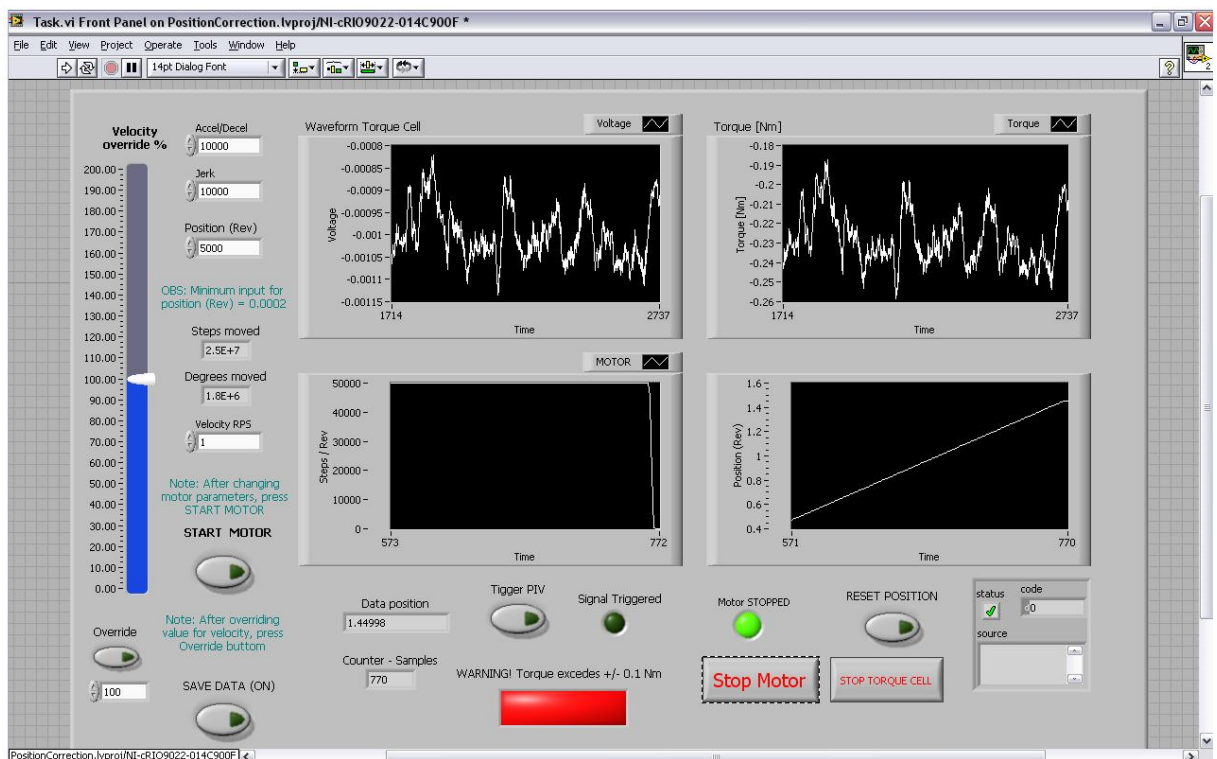


Figure 2.20: LabView interface

Chapter 3

Computational Fluid Dynamic Simulations

This CFD study focuses on providing information that can be used to properly correct the data acquired in the experiment performed in the water tunnel, which is known to be affected by blockage due to the walls of the tunnel facility, as described next in Chapter 4. Since the experimental data obtained must be corrected to unbounded flow conditions (see §4.1), a key point presented in this CFD chapter is the unbounded model domain validation. The study also included Re_D dependency analysis to verify the validity of the simulations results for a range flow conditions.

This chapter has two main sections which describe the computational modelling approach used to represent the fluid phenomena of kinetic turbines operating in water tunnel and free stream conditions. The first section presents the conceptualization of the turbine and physical domain in such a way that can be translated into a simple computational model. In this context, the rotor has been conceptualized as a continuous plane that extracts energy from the flow. Suitable boundary conditions have been set up to the model in order to represent both scenarios, the water tunnel and open flow conditions. The second section of this chapter presents the details of the computational tools used for these purposes. Note that this second section is an overview description of the mathematical equations employed in the ANSYS CFX tool, but is not an exhaustive text on CFD.

3.1 Modelling Approach

3.1.1 Porous disk

Several approaches have been used to model the aerodynamics of horizontal axis wind turbines [3]. Regarding the near wake, the porous or actuator disk technique has been widely utilized in numerical models, as well in experimental testing applied to horizontal tidal stream turbines [12, 35]. This porous disk model has the advantage of requiring a reduced mesh density compared to other available numerical models for CFD simulations [3, 35]. Thus, it is computationally less expensive, and it is utilized to simulate the blockage effects in this study.

Because this method conceptualizes the rotor as a plane which extracts energy from the flow, a drawback of this model is that the blades of the turbine are not directly simulated. However, considering the objectives of these CFD simulations, this approach is adequate to meet the study purposes.

The total pressure drop that the actuator disk area exerts on the fluid is represented by a unidirectional momentum loss, or thrust force per volume unit, χ applied at the disk volume. For the CFD simulations, this momentum loss is rewritten in terms of the thrust coefficient (C_T), the upstream axial inlet velocity (U_0), the water density (ρ), and the thickness of the disk (t), as presented in Eq. (3.3). Equation (3.3) is obtained by equating the thrust force from Eq. (3.1) and Eq. (3.2), as follows:

$$T = \frac{1}{2}\rho AU_0^2 C_T \quad (3.1)$$

$$\chi At = T \quad (3.2)$$

$$\chi = \frac{\frac{1}{2}\rho U_0^2 C_T}{t} \quad (3.3)$$

3.1.2 Domain

The simulations were run over two different computational domains. The first domain accounted for the unbounded conditions where no wall prevents the streamlines from expanding freely. The second computational domain models the water tunnel, which allows for comparison between experimental and full scale conditions.

Defining D (15 cm) as the diameter of the scaled rotor being tested, the rectangular water tunnel computational domain has a cross-sectional area of $3D \times 3D$ and

a length of $15D$, and the disc is placed $5D$ downstream of the inlet centred in the tunnel section, corresponding to the experimental setup. The unbounded rectangular computational domain is defined with a section of $6D \times 6D$, $25D$ long, and the disc located $5D$ downstream from the inlet. For both cases, a structured mesh was generated using ICEM, applying O-grid and blocking topology features that facilitate the manipulation of the grid for a 3D model.

As detailed in the boundary conditions section next, symmetry is applied to the original model described, which allows the simulations to be run over a quarter-domain as shows scheme in Fig. 3.1.

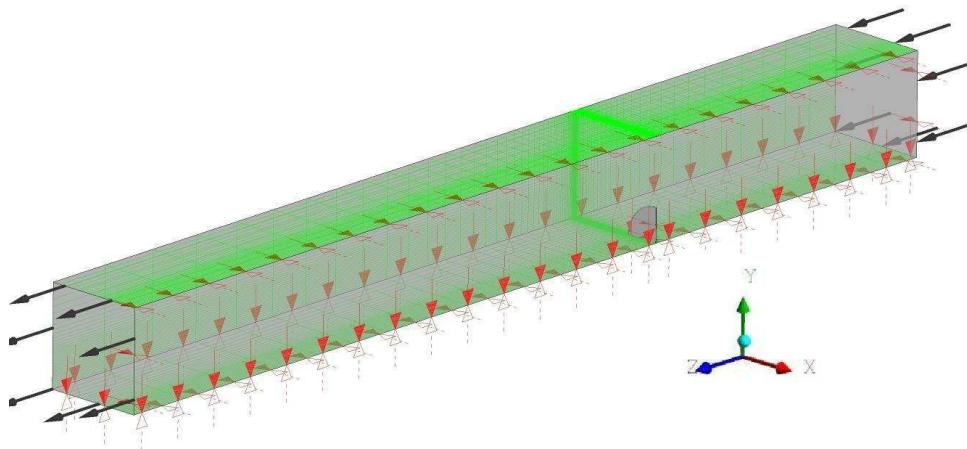


Figure 3.1: Quarter domain water tunnel model (ANSYS CFX)

By computing simulation results for four different rotor sizes, the effects of blockage ratio were explored, where blockage ratio is defined as the ratio of rotor swept area to tunnel section area (A/A_{tunnel}). The thickness of the disc was fixed at 0.5% of the rotor diameter ($0.005D$) in all cases.

3.1.3 Boundary Conditions

A uniform axial velocity of 2 m/s was set up at the inlet of the domains. This boundary condition is physically driven by the pump in the water tunnel, and also represents the operational expected flow velocity in the open water. At the outlet, an average static pressure was defined, with relative pressure equal to zero. Specifying an average static pressure over the whole outlet allows the pressure variable to vary locally over the outlet boundary such that the average pressure is constrained to a specific value. Physically, this may be the situation of the experiment with a higher velocity at the centre of the section and lower near the wall region. Additionally, this boundary condition configuration is listed as the most numerically robust option in Ansys CFX [36].

At the actuator disk a unidirectional momentum loss χ (referring to Eq. (3.3)) was applied to account for the pressure drop for each C_T value computed. Since a quarter domain was used, two symmetry planes were applied, in the vertical and horizontal planes respectively. These boundary conditions were also active for the area of the disc in contact with these symmetry planes. For the unbounded domain, an opening boundary condition, allowing fluid to cross the boundary surface but keeping a constant pressure value at the boundary, was applied to the walls. For the water tunnel domain, the base case considers a free-slip wall condition.

Even though free-slip conditions at the walls were previously defined as a boundary condition in order to compare the CFD results to the analytical expressions for blockage discussed in §3.3, additional simulations were run to investigate the effects of the boundary layer growth within the tunnel. A minimum number of 10 nodes within the boundary layer is suggested by the ANSYS CFX Guidelines [37] for the near-wall turbulence model to work properly. For a turbulent boundary layer on a flat plate in similar flow and fluid conditions, the viscous sublayer thickness should be less than 1 mm [38]. Thus, to include the effects of viscous losses at the boundary, a mesh having 10 nodes within this first 1 mm layer was generated from the wall to properly compute the boundary layer [36]. The dimensionless wall distance is known as $y_+ = \frac{u_* y}{\nu}$ where the friction velocity is $u_* = \sqrt{\frac{\tau_w}{\rho}}$ and τ_w is the wall shear stress. In the simulations run, y_+ was approximately 10.

The water tunnel used for testing has a very low turbulence level (approximately 1%) which was used in the simulation inputs. Both laminar and turbulent flows were computed. The Reynolds Average Navier-Stokes (RANS) equations were solved for

steady and incompressible flow, using a finite-volume method, and the $K-\Omega$ equation was used to model the turbulence, as described next in §3.2.1.

3.2 Computational Model

The academic version 12.0 of the commercial package ANSYS CFX was used for the three-dimensional CFD simulations, and the structured mesh over the domain was generated using ANSYS ICEM.

The Navier-Stokes equations for mass-flow and momentum can be discretized and solved numerically using diverse solution methods. The CFX package corresponds to a particular CFD code based on a finite volume technique [39] in which the fluid region of interest is split into smaller sub-regions, so called control volumes. This subdivision allows an iterative solution of the set of partial differential equations for each small sub-region. Finally, an approximate solution of the variables of study is obtained, point by point, over the entire flow field domain.

3.2.1 Governing Equations

The basic equations of fluid mechanics, for describing the fluid motion, are the Navier-Stokes equations, Eq. (3.4) and Eq. (3.5), where ρ is the fluid density, u the vector velocity, p the pressure, τ the stress tensor, and S_M the additional scalar term representing a momentum source (refer to section next 3.2.2). Equation (3.4) is known as the continuity equations, and Eq. (3.5) is called the momentum equation. These general N-S equations are valid for both turbulent and non-turbulent flows, steady and non steady conditions. The energy equations were not required, as the change in fluid properties with temperature are negligible in the cases under investigation.

$$-\frac{\partial \rho}{\partial t} + \nabla(\rho u) = 0 \quad (3.4)$$

$$-\frac{\partial(\rho u)}{\partial t} + \nabla(\rho u \otimes u) = -\nabla p + \nabla \cdot \tau + S_M \quad (3.5)$$

The fluid conditions that characterize the experiments performed in the water tunnel makes it necessary to incorporate turbulence in the CFD model. Turbulence occurs when the inertia forces in the fluid become important relative to viscous forces

(i.e. higher Reynolds numbers). In CFD modelling turbulent flows can be thought of as an average characteristic, with an additional random fluctuation superimposed in time and space. Thus, the turbulent flow can be statistically modelled for example as an instantaneous velocity expressed as the sum of the mean velocity and a fluctuating component Eq. (3.6), where the mean velocity is estimated as expressed in Eq. (3.7).

$$\mathbf{u} = \bar{u} + u' \quad (3.6)$$

$$\bar{u} = \frac{1}{\Delta t} \int_t^{t+\Delta t} \mathbf{u} dt \quad (3.7)$$

This statistical technique is applied to the Navier-Stokes equations producing the RANS equations. For this particular model the governing equation for the turbulent and incompressible flow are the RANS equations. The averaged quantities are substituted into the general transport equations and rearranged, resulting in Eqs. (3.8) and (3.9):

$$-\frac{\partial \rho}{\partial t} + \nabla(\rho \mathbf{u}) = 0 \quad (3.8)$$

$$-\frac{\partial(\rho \mathbf{u})}{\partial t} + \nabla(\rho \mathbf{u} \otimes \mathbf{u}) = -\nabla p + \nabla \cdot (\tau - \overline{\rho \mathbf{u} \otimes \mathbf{u}}) + S_M \quad (3.9)$$

where the terms $\overline{\rho \mathbf{u} \otimes \mathbf{u}}$ have the same structure as the viscous stress tensor and are called Reynolds Stresses, however these terms arises from a non-linear convective term contribution of the fluctuating velocities to the change of the averages ones. The Reynold stress tensor incorporates additional unknown variables to be solved in the CFD model, generating a closure problem.

Since this study considers stationary flow conditions, the varying-time terms in Eq. (3.8) and Eq. (3.9) become zero. Notice that ANSYS CFX is an iterative solver which approaches the solution of the set of partial differential equations over a set of iterations. The solver therefore uses a timestep for iteration process, used only to under-relax the governing equations.

In order to achieve closure for equation Eq. (3.9), turbulence models are introduced to compute the Reynolds stresses and fluxes. Depending on the assumptions of these models, there are two main types available in CFX: eddy viscosity models and Reynolds stress models [36]. For this study, to achieve closure, the $K - \Omega$ model

was used, which is part of the family of eddy viscosity two-equation turbulent models. This model has become a widely used turbulence model [40], which can predict effects for both free shear flows (which is the case of the wake behind the rotor in this study) and wall-bounded boundary layer flows with reasonable accuracy provided a good detailed mesh is used, as indicated in §3.1.3 [36]. Considering the simulations comprises both free-slip and non-slip boundary condition set ups, this turbulence model is suitable for the whole range of flow conditions. In addition, CFX has been run in a laminar model (i.e. with Reynolds averaging) for comparison to the turbulence model results.

3.2.2 Momentum Source Sink

In ANSYS CFX, sources allow for adding additional terms to the set of equations being solved by CFX with the purpose of modelling an additional physical process. In this case, the pressure drop, caused by the disc, is introduced by setting a general momentum source sink in the streamwise direction, over the disc volume (thin plane). Note that this type of source does not introduce any additional mass but it does model flow resistance.

This momentum source sink is specified in terms of a momentum loss value per unit of volume in a specific direction, and setting up a value equal to zero in all others directions. Convergence is improved when the source is a function of velocity [36]. The source is linearized by setting a momentum source coefficient K . Note that this momentum source coefficient K is equivalent to the unidirectional momentum loss (thrust force per volume unit) χ defined in Eq. (3.3), therefore this χ value is calculated as function of the variables characteristic of each running, and introduced in the CFX model.

Finally, ANSYS CFX solves Eq. (3.10) within the system of equations for the Z coordinate component direction (components in the X and Y axis directions were set up as zero).

$$-\frac{\partial p}{\partial Z} = KU_Z \quad (3.10)$$

3.2.3 CFX Boundary Conditions

The set of boundary conditions established in this model were already stated in §3.1.3, and therefore this section explains the tools available in ANSYS CFX for applying the boundary conditions depicted in Fig. 3.2.

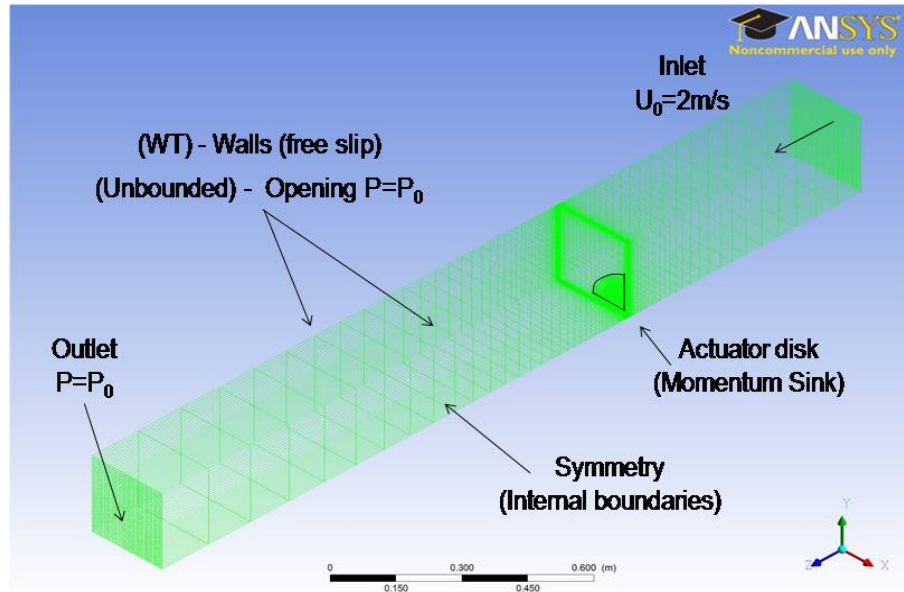


Figure 3.2: CFX quarter domain boundary conditions

To simulate an open boundary condition, representing the unbounded domain, the Opening Boundary was applied to the walls [41]. This CFX boundary condition allows fluid to enter and exit the domain, and a constant pressure is kept at the boundary surface, as shown Eq. (3.11).

$$p_{opening} = p_{spec} \quad (3.11)$$

For the water tunnel domain, the Wall Boundary Free Slip was applied to the walls. For this case the velocity normal to the wall and the wall shear stress are both set to zero, whereas the velocity component parallel to the wall has the velocity computed for the fluid flow at that location. No fluid is allowed to cross the surface domain. Summarizing, for the constrained domain with free slip condition: $U_{n,wall} = 0$ and $\tau_w = 0$.

Since a quarter domain was defined in the model, two boundary symmetry planes were applied to the vertical (Y axis) and horizontal (X axis) respectively. This boundary condition provided a plane of both geometric and flow symmetry.

The recommended general configuration of boundary conditions provided by the ANSYS CFX Solver Modelling Guide [36] indicated that setting velocity flow at the inlet and static pressure at the outlet is the most robust configuration. Thus, a Cartesian velocity component inlet boundary was set up at the boundary surface, having a uniform finite value in the direction normal to the surface (Z axis) and zero in the X and Y axis, as Eq. (3.12) states.

$$U_{inlet} = U_{spec,X} + U_{spec,Y} + U_{spec,Z} = 0 + 0 + U_{spec,Z} \quad (3.12)$$

For the outlet surface, the static pressure outlet boundary was applied. A relative average pressure equal to zero was maintained fixed at the outlet surface, as Eq. (3.13) states.

$$P_{average,outlet} = P_{spec} \quad (3.13)$$

In the additional simulations run to investigate the effects of the boundary layer growth within the tunnel, the Wall No slip boundary condition was applied to the wall surfaces. In these cases the velocity of the fluid is set to zero at the wall. Then, the boundary condition for the velocity turned is $U_{wall} = 0$.

3.3 CFD Simulation Results

The results from the CFD simulations are presented in this section, where *theory* stands for the values of the simple momentum theory without corrections.

Four different rotor sizes were computed in the CFD simulations, corresponding to 5.5%, 9%, 20%, and 55% blockage ratios, where the blockage ratio was defined as the ratio of the rotor swept area to the cross-sectional area of the tunnel (A/C). A volume-weighted average axial induction factor was computed over the disk volume for each run. The power coefficient C_P was then computed as a function of the thrust coefficient C_T , which is an input to the simulations, and the axial induction factor, as stated in Eq. (3.14):

$$C_P = C_T(1 - a) \quad (3.14)$$

3.3.1 Unbounded Flow Validation

The results for the power coefficient, for both laminar and turbulent flow simulations, for unbounded conditions, were found to have good agreement with respect to the standard actuator disc theory presented in Appendix A up to C_T values of 0.8 (see Figure 3.3). For higher values of C_T , the difference between the simulations and analytic theory becomes larger, as expected, due to the absence of a high thrust coefficient model in simple momentum theory. Also, in terms of power coefficient, there is no significant difference between the results obtained for laminar and low turbulence level flow simulations.

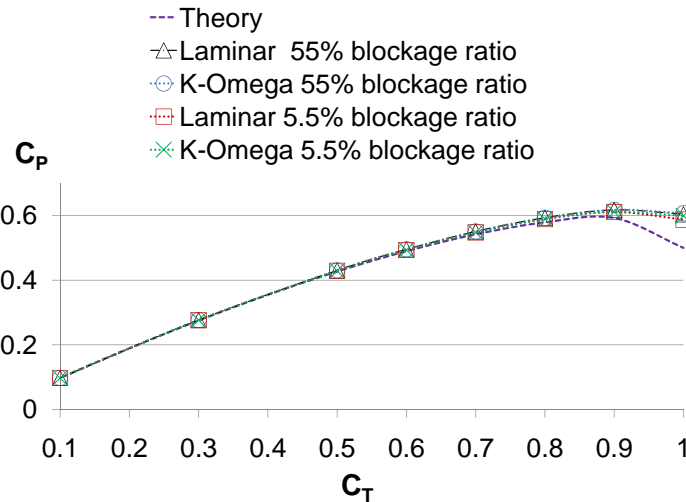


Figure 3.3: C_P v/s C_T for turbulent flow conditions in bounded domain with opening boundary conditions

Referring to Fig. 3.3, the results from the smallest and larger disc sizes computed (i.e. 5.5% and 55%) were used to check the opening boundary condition influence. As the two results are quite similar, the ability of the opening boundary condition to unduly influence the results for unbounded conditions is verified.

As part of the unbounded flow validation results, a disk thickness and mesh dependency study were also performed. For the disk thickness analysis, four width values were computed, referred to the disc of 15 cm diameter. These four values correspond

to a thicknesses of 5%, 1%, 0.5%, and 0.25% of the disc diameter respectively. The C_P was computed for the four cases and the results compared to the C_P values expected from theory (Appendix A). Table 3.1 presents the difference between the computed C_P and the theory value, for each disc thickness case, over a range of C_T values.

C_T	5 % diameter	1 % diameter	0.5 % diameter	0.25 % diameter
0.1	0.06 %	0.06 %	0.06 %	0.06 %
0.3	0.24 %	0.23 %	0.22 %	0.22 %
0.5	0.52 %	0.52 %	0.49 %	0.49 %
0.7	1.19 %	1.15 %	1.07 %	1.07 %
0.9	3.28 %	3.18 %	3.02 %	3.01 %

Table 3.1: ΔC_P (%) with respect theory value for different disc thickness

From this study, a disc thickness of 0.5 % of disc diameter was found to be appropriate for the simulations, since at this width value the difference in C_P values with respect the theory became almost constant. Decreasing the disc thickness further did not increase the accuracy of the results but did increase the simulation run times.

Regarding the mesh dependency study, a similar approach was used to determine the best mesh configuration based on a tradeoff between speed and accuracy. A structured mesh was defined for the unbounded domain. Since the main changes in the velocity vector occur in the axial plane (perpendicular to the rotor plane), the mesh of the sections aligned with the rotor plane was kept constant upstream and downstream of the rotor, and only the mesh comprising the elements perpendicular to the disc plane were changed to explore mesh dependency. The mesh in the axial plane was defined starting with the smallest element sizes at the disc plane and then increasing the element size upstream and downstream perpendicular to the disc plane. The mesh inflation ratio at the disc proximity was set to a value of 1.1.

Four cases were run, as detailed in Table 3.2, and the results in terms of the difference between C_P from simulations and theoretical expected values are presented in Table 3.3.

Based on the result obtained for the different configurations, presented in Table 3.3, the mesh with 40 elements upstream and 50 elements downstream was found

Case No	Elements upstream	Elements downstream	Total mesh elements
1	20	25	95,885
2	40	50	178,910
3	80	100	344,960
4	100	125	427,985

Table 3.2: Cases for mesh dependency study

C_T	Case 1	Case 2	Case 3	Case 4
0.1	0.10 %	0.06 %	0.06 %	0.06 %
0.5	0.57 %	0.49 %	0.49 %	0.48 %
0.7	1.13 %	1.07 %	1.07 %	1.07 %
0.9	3.16 %	3.02 %	3.01 %	3.01 %

Table 3.3: ΔC_P (%) with respect theory value for different mesh configurations

to be good enough for the purpose of the study. The finest mesh slightly increases the accuracy of the results at the expense of greatly increased running time.

Regarding convergence, the RANS equations were solved with Root Mean Square (RMS) velocity residual levels of 1E-05, within the maximum number of iterations set for the solver, and a maximum momentum residual of 1E-04. Increasing the number of iterations was not found to modify the results, and so the solution was considered converged for the purposes of this study. Note that an RMS of 1E-05 indicates adequate convergence for most engineering applications [37].

3.3.2 Bounded Flow Results

Figure 3.4 shows the results for power coefficient and thrust coefficient in turbulent flow conditions, for the water tunnel domain. It is seen that for C_T values higher than 0.3, the increment in power coefficient with respect to the simple momentum theory (Chapter A) for unbounded flows becomes noticeable, especially for the larger rotors.

It is found that as the blockage ratio increases, a higher maximum value of power coefficient is obtained, which occurs at a higher C_T value, as depicted in Fig. 3.5.

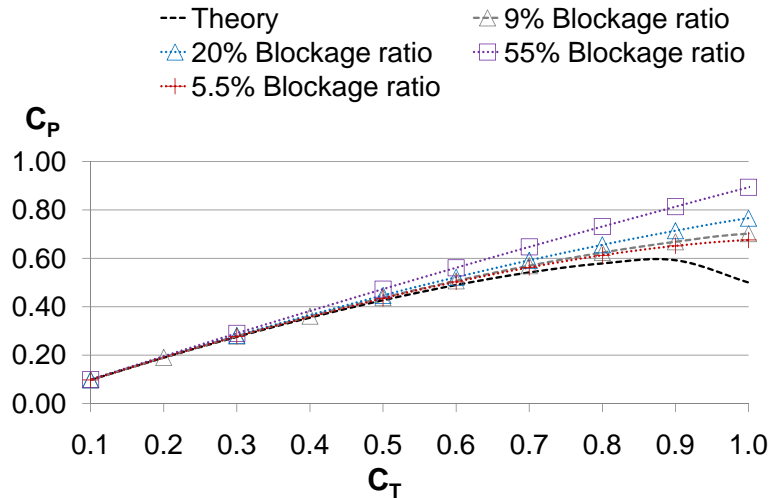


Figure 3.4: C_P v/s C_T for turbulent flow conditions in water tunnel domain

Note that optimal rotor performance for free-stream conditions occurs at a C_T value of approximately 0.89, thus these differences become important. This effect was also mentioned by Garret, in the study of the efficiency of a tidal turbine operating in its optimum conditions [42]. Table 3.4 presents the maximum value of the power coefficient found for each blockage ratio in the CFD simulations.

Notice that as the blockage in the tunnel is increased, extra power needs to be added to flow. Physically this is made possible in the experiments by extra pressure being provided by the pump system to keep a constant flow rate at the inlet of the water tunnel while performing the experiments. In a real tidal channel, increased blockage would in fact retard the overall flow through the channel. Therefore Fig. 3.5 should not be interpreted as indicated that very high blockage ratios are advantageous (there will be a unique optimum for each channel [42]).

3.3.3 Tunnel Wall Boundary Growth Effects

The effect of boundary layer growth was explored for a blockage ratio of 9%, which represents the scaled rotor size within the water tunnel facility. The results are shown in Fig. 3.6. For the case in which a no-slip condition was defined at the wall boundary,

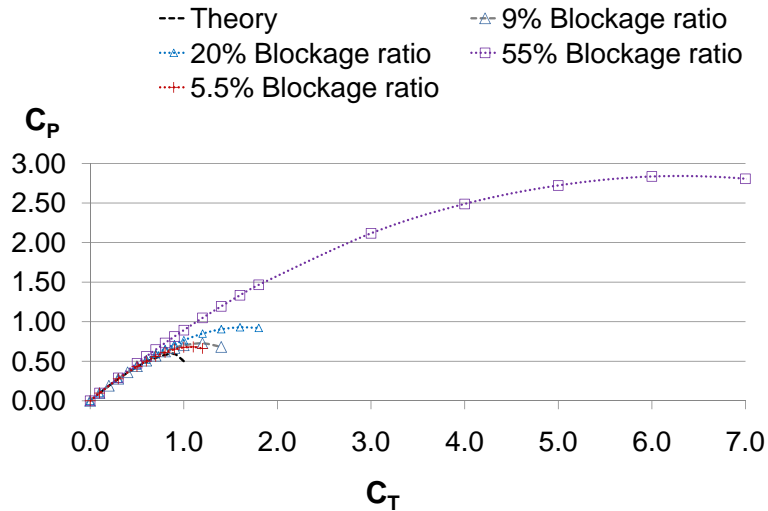


Figure 3.5: C_P values for a wider range of Thrust Coefficients

an increment in power coefficient was found with respect to the case where free slip condition was defined at the wall. This effect can be explained by a reduction in the water tunnel section caused by the growth of the boundary layer. The increment in power coefficient is not significant in this particular case, reaching a value of 2% for a thrust coefficient of 0.9. The simplification of not resolving the boundary layer helped to reduce the long run-times of the simulations, and focused the investigation on the blockage effects for a given domain size, as discuss in Chapter 4. In any case, this extra increment in power due to wall boundary growth effects can be eventually

Blockage ratio	Max. C_P	C_T
5.5%	0.682	1.1
9%	0.727	1.2
20%	0.929	1.6
55%	2.835	6

Table 3.4: Maximum C_P values

incorporated to the final axial induction factor $a-C_P$ correction curve.

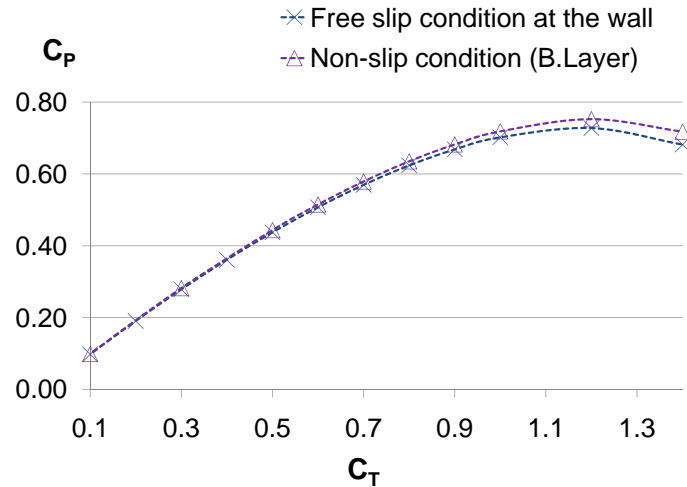


Figure 3.6: Boundary layer effect for a rotor diameter 15 mm (9% blockage ratio) referenced to tunnel conditions

3.3.4 Reynolds Dependency Analysis

A set of simulations for turbines of different diameters and flow speeds were run to explore the Reynolds wake dependency effects over a wider range of Re_D . These simulations, as detailed in Table 3.5, resulted in practical Re_D ranging from 2×10^5 to 2×10^7 , where Re_D is defined based on disc diameter. The intent of these simulations was to explore any Reynolds number effects in the viscous wake to verify the assumptions of Re_D independence in the CFD simulations.¹ Clearly the actuator disc simulations ignore any blade chord Reynolds number effects, which are known to be important, but are a separate consideration to the wake dependency on Re_D .

Simulations for each case detailed in Table 3.5 were run for different blockage ratios. The change in power coefficient as defined in Eq. (4.4) was computed for each case. Figure 3.7 presents the results for the power coefficient to thrust coefficient

¹It is commonly asserted that wake dynamics are Re_D in experimental campaigns.

Turbine diameter [m]	Inlet velocity [m/s]	Re_D
0.15	2	2×10^5
0.15	150	2×10^7
1	3	2×10^6
10	3	2×10^7

Table 3.5: Turbine size and flow conditions for additional RANS simulations

relationship in turbulent flow conditions for the unbounded domain. For thrust coefficients up to 0.8 good agreement can be observed for the power coefficient with respect the theory, for the whole range of Re . Also, there is no noticeable difference between the power coefficient values obtained in the simulations for Re ranging from 10^5 to 10^7 .

Figure 3.8 shows the increment in power coefficient with respect the unbounded domain at $C_T = 8/9$, as the blockage ratio varies, for different Re_D conditions. There is an expected positive trend; as the blockage ratio increases, the increment in C_P also becomes greater. With respect to the values of C_P obtained for the same blockage ratio and different Re numbers, there is only a subtle difference between the values, less than 2 % in terms of C_P increment that becomes noticeable at larger blockages ratio values, such as 60 %. These results support the assumption that the mismatch between full-scale and model scale Reynolds number do not affect wake development, as these CFD simulations only simulate the wake behaviour.

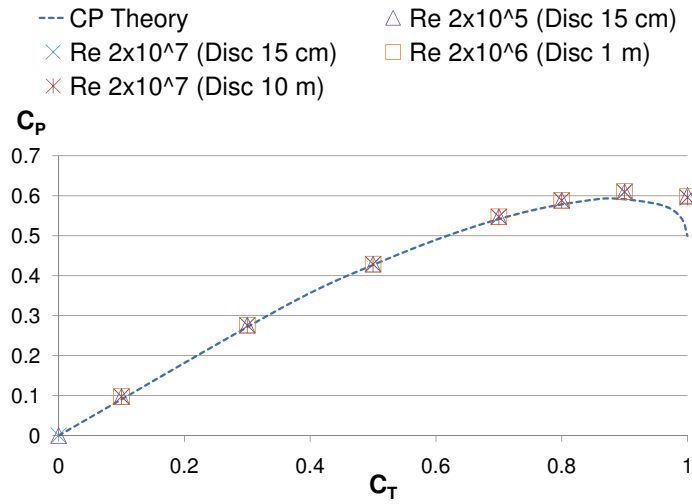


Figure 3.7: C_P v/s C_T , Unbounded domain

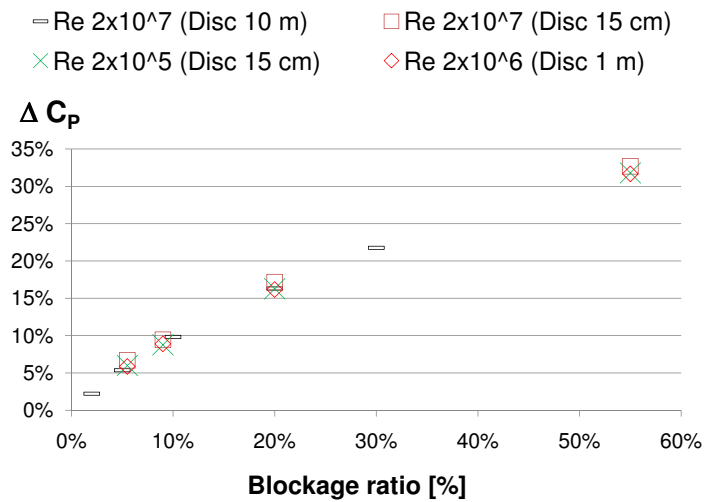


Figure 3.8: C_P increment v/s blockage ratio at $C_T = 8/9$

Chapter 4

Tunnel Blockage Correction Models

It is desirable in experimental testing to have larger scale models to achieve Reynolds (Re_c) similitude. However, for a large ratio of rotor swept area to tunnel cross-section area, the walls of the water tunnel constrain the flow and increase the velocities around the rotor. This in turn increases the forces and torques compared to open water conditions, as depicted in Fig. 1.2, Chapter 1. Thus, the values acquired from experiments performed in tunnel facilities must be corrected to unbounded conditions, to accurately predict the performance of full size turbines. Available methodologies for correcting results handle the tunnel interference by determining an equivalent free stream velocity, and correlating this value to thrust coefficient to finally correct the measured power coefficient.

Hence, standard blockage correction techniques require measurement of rotor thrust to correct power coefficients for bounded testing domains. Due to the small forces and compact nature of the testing rig developed in this thesis, accurate thrust measurement is not possible. This chapter therefore presents a methodology that utilizes the velocity field data at the rotor plane obtained from the water tunnel test and CFD simulations based on the actuator disk concept to account for blockage without the requirement for thrust data. The velocity can be obtained with PIV or other techniques, however PIV data is to be simultaneously utilized for wake characterization and to estimate the average velocity at the disc plane, and so was made the basis of the new correction technique.

In essence, the correction technique uses PIV measurements to compute an average

axial induction factor that can be related to the characteristic power coefficient. From CFD simulations, the increment in C_P is predicted for a given set of operational conditions that represents the water tunnel setup. These CFD values then provide a $a-C_P$ correction curve to be utilized for processing the experiment test data. Furthermore, to investigate the validity of the conventional analytical expressions, a comparison is made between analytical and CFD correction results for different operational conditions and blockage ratios.

4.1 Thrust Based Analytical Models

One of the first tunnel correction methods was developed for propeller testing by Glauert [20] in the late 1920's. Glauert introduced the concept of equivalent free air speed V' which would produce the same velocity at the disc, thrust and torque on the rotor as those observed in the tunnel for the corresponding tunnel datum velocity U_0 . In that model, the real and scale machines both rotate at the same angular velocity thus giving different tip-speed ratios for free and tunnel conditions. For propellers, the equivalent free stream velocity is normally less than the tunnel datum velocity, whereas for energy extracting devices, such as wind and tidal turbines, this equivalent freestream velocity is larger than the tunnel datum speed.

To find the equivalent free velocity V' , based on the actuator disk approach, the principles of momentum balance, force balance, and continuity are applied to the case of the device rotating in the tunnel. Finally, an analytical expression correlating V' , inflow tunnel velocity U_0 , relative rotor/tunnel size, and thrust coefficient C_T is found and used to correct the testing data to unbounded conditions. This method, based on the axial momentum theory, is still widely used and has been adapted for wind turbine experimental testing corrections [19], accounting for negative thrust (relative to propellers which in Glauert's theory have positive thrust).

An improvement to the Glauert method was recently developed by Mikkelsen and Sorensen for wind turbines [21, 43]. This method is also based on the axial momentum theory and the concept of equivalent free stream velocity of Glauert [20], but a new solution was presented to account for the wall blockage effects of flow expansion. This method has the advantage of working with non-dimensional variables and obtaining the corrected free stream velocity U_C in a more straightforward procedure but still

requiring thrust measurements. Moreover, this methodology resolved the singularity inherent in Glauert's correction for a thrust coefficient of -1.

Regarding tidal turbines, as yet little has been developed to account for wall interference in experimental testing. One good reference is provided by Bahaj [15] who derived an analytical blockage correction for wake expansion applicable to experimental testing of tidal turbines. This analytical correction was derived using an actuator disk model to represent the rotor of the turbine, and applying the principles of continuity and momentum and force balance on the water between the far upstream and far downstream at the tunnel facility. An equivalent water speed U_F , similar to the equivalent free stream velocity V' determined by Glauert [20], was obtained by applying an iterative procedure. Finally, experimental power and thrust coefficients, as well as tip speed ratios are corrected as a function of the ratio of equivalent open water speed to water tunnel velocity. The method is very similar to those developed for wind turbines.

4.1.1 Momentum Based Model

The three analytic reference models cited above represent the propeller [20] or turbine [15, 21, 43] by a disk plane that causes a uniform pressure drop as the flow goes across it [1]. The flow field is assumed to be inviscid, irrotational, and incompressible over the entire domain. Two separate regions are clearly defined as shown in Fig. 4.1; the region inside the streamtube and the region between the streamtube and the walls of the tunnel.

Far upstream, the flow is characterized by a uniform axial inlet velocity U_0 and a pressure p_0 . A stream tube with upstream area smaller than the disc bounds the flow through the disk. As the flow approaches the disk, its velocity slows down, which also causes expansion of the streamtube. This induced velocity can be described by a speed variation factor $a = 1 - \frac{u_1}{U_0}$ called the axial induction factor. At the disk plane, a pressure drop ($p_+ - p_-$) is exerted to account for energy extraction, and as a result of this the downstream flow inside the streamtube, called the wake, proceeds with reduced pressure and reduced velocity, compared to the flow outside the streamtube. In the far wake, it is assumed that the pressure has risen to match the flow pressure outside the bounding streamline, and the wake has fully expanded. Very far downstream viscous mixing combines exterior and interior flows. Refer to Fig. 4.1,

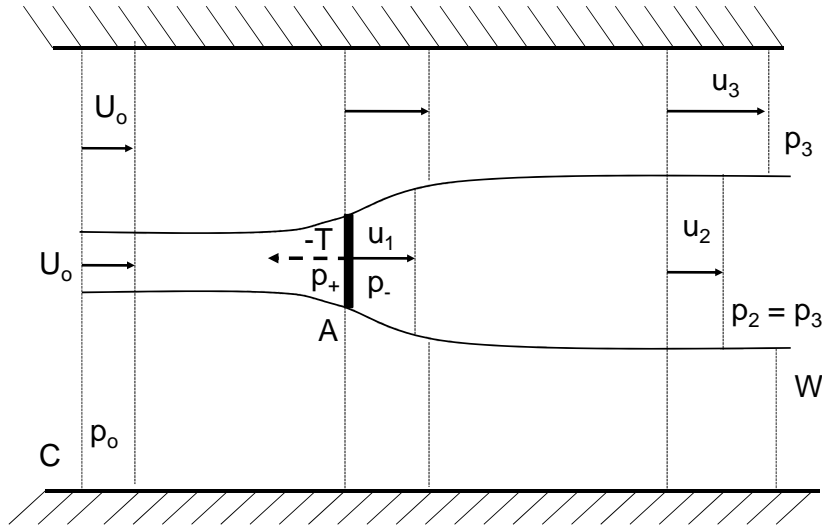


Figure 4.1: Actuator disk model in a closed tunnel section

at the far wake $p_2 = p_3 < p_0$ and $u_2 < u_3$. Clearly the distinct wake expansion then mixing regions are an approximation to reality, but this standard theory has been shown to be a reasonable analytic model.

Unlike what this simple theory dictates and from which the analytical corrections [15, 20, 21, 43] were obtained, while performing experimental testing in a water tunnel, the viscosity and the turbulence in the fluid will produce - to a greater or lesser degree depending on the flow conditions - lateral flow mixing between the wake and the region outside the streamtube. Additionally, the larger the blockage ratio and the rotor load, the larger the increment in the axial induction factor, which leads to smaller velocities in the wake and higher velocities downstream outside the streamtube which eventually will cause the flow to mix into the streamtube. Also, for higher thrust loads, a region with flow recirculation becomes visible within the wake. These effects are accounted for in standard the BEM theory used to analyze rotors through empirical C_T models, as the simple momentum formulations of BEM theory break down. Therefore, depending on the operational conditions of the turbine being tested, and the relative rotor size to the tunnel cross sectional area, analytical expressions may

not give accurate corrections. This uncertainty motivates the current investigation to determine the blockage ratio range in which analytical corrections can be satisfactorily applied without incurring significant errors. In addition, rationalized bounds on model size and testing thrust values are required.

4.2 Blockage Correction Model Development

The models presented by Glauert [20], Mikkelsen and Sorensen [21, 43], and Bahaj [15], provide a correlation between C_T and the ratio of equivalent open velocity (U_C) to tunnel velocity. This accounts for the change in loading and induced velocities, due to wall interference in a testing tunnel, and can be used to correct the experimental data. Once the theoretical corrected velocity is determined, by solving any of the methods previously identified, the corrections to the experimental characteristic coefficients are a straightforward mathematical calculation.

For a given C_T obtained from thrust measurement in the test tunnel, there is a corresponding correction factor that should be applied to get the equivalent characteristic coefficient in open conditions. Corrections for the power and thrust coefficients and the tip speed ratio λ , as noted in reference [15] are:

$$C_{P,unb} = C_{P,wt} \left(\frac{U_0}{U_C} \right)^3 \quad (4.1)$$

$$C_{T,unb} = C_{T,wt} \left(\frac{U_0}{U_C} \right)^2 \quad (4.2)$$

$$\lambda_{unb} = \lambda_{wt} \left(\frac{U_0}{U_C} \right) \quad (4.3)$$

where U_0 is the actual inlet velocity in the experiments, U_C is the velocity corrected to freestream conditions, $C_{P,unb}$, $C_{T,wt}$, and λ_{unb} correspond to the power coefficient, thrust coefficient and tip speed ratio for unbounded domain, and $C_{T,unb}$, $C_{P,wt}$, and λ_{wt} correspond to the power coefficient, thrust coefficient, and tip speed ratio obtained in the tunnel facility.

It is important to notice that a difficulty arises in this process when thrust data is not being acquired during testing. To address this issue, in the current work, CFD simulations are used to estimate the corrected free stream velocity and to also provide

a correction curve relating the available experimental data and the corrected velocity, as described in the following paragraphs.

Figure 4.2 shows the trend curve for C_P versus C_T for both domains, the water tunnel and the unbounded region. Δ is defined as the difference between the water tunnel-power coefficient $C_{P,wt}$ and the unbounded-power coefficient $C_{P,unb}$, for a given C_T value, as shown in Eq. (4.4). Note that C_T is referenced to actual conditions in both domains.

$$\Delta = C_{P,wt} - C_{P,unb} \quad (4.4)$$

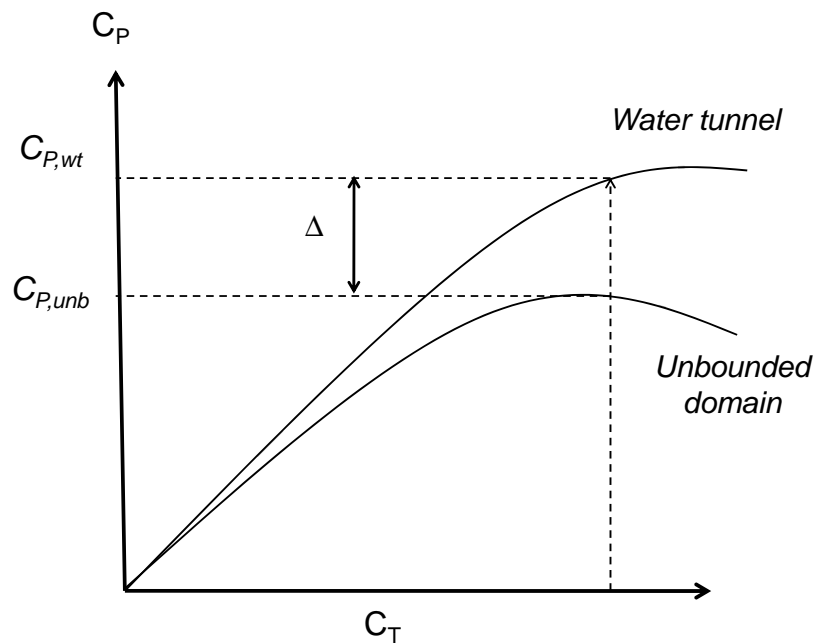


Figure 4.2: Trend of C_P v/s C_T in water tunnel and unbounded domains

Thus, the power coefficients in the water tunnel and unbounded domains for a given thrust coefficient can be expressed as in Eq. (4.5) and in Eq. (4.6), where P_{wt} and P_{unb} are the power extracted by the rotor in the water tunnel and unbounded domain respectively.

$$C_{P,wt} = \frac{P_{wt}}{\frac{1}{2}\rho AU_0^3} \quad (4.5)$$

$$C_{P,unb} = \frac{P_{unb}}{\frac{1}{2}\rho AU_0^3} \quad (4.6)$$

Since $C_{P,wt} > C_{P,unb}$, for a given C_T value, it is clear that $P_{wt} \neq P_{unb}$ as defined in Eq. (4.5) and Eq. (4.6). However, it is possible to define a corrected freestream velocity U_C that will produce the same thrust force at the rotor in the unbounded domain as in the water tunnel, for a given velocity u_1 across the disk, and when the turbine is assumed to keep the same angular velocity [20]. Therefore, at these similar conditions in the bounded and unbounded domains, the same torque and power are generated.

For this corrected freestream velocity U_C , the power in the water tunnel is the same as the power in the unbounded domain $P_{wt} = P'_{unb}$, where P'_{unb} is the equivalent power that the rotor would extract while running at the same rotational speed inserted in a flow stream having a speed equal to the corrected free stream velocity U_C [20]. Consequently, $C_{P,unb}$ can be rewritten as in Eq. (4.7), where $C_{P,wt}$ is found to be proportional to $C_{P,unb}$ by a factor K^3 , as shown in Eq. (4.8). From CFD simulations, the power coefficient for both the unbounded and water tunnel conditions can be obtained for a range of thrust coefficients. Then, replacing the corresponding values of $C_{P,unb}$ and $C_{P,wt}$ in Eq. (4.8) a correction factor K^3 , correlating power and thrust coefficient, is estimated. Also, from CFD simulations an average axial induction factor is computed for both the unbounded and tunnel domain, for the range of C_T values. As a result, there is a corresponding power coefficient C_P , an axial induction factor a , and a correction factor K^3 associated with each given thrust coefficient C_T . In such way, a curve correlating axial induction factor and thrust coefficient is obtained, providing the final axial induction factor/power coefficient correction curve that will be utilized in the data correction for the experimental testing.

$$C_{P,unb} = \frac{P'_{unb}}{\frac{1}{2}\rho AU_C^3} \quad (4.7)$$

$$C_{P,wt} = C_{P,unb} \left(\frac{U_C}{U_0} \right)^3 = C_{P,unb} K^3 \quad (4.8)$$

4.2.1 CFD Correction Factors

Using the same CFD models presented in Chapter 3 and Eq. (4.8), the ratio of corrected free-stream velocity to tunnel inlet velocity is found for a range of thrust coefficients, in turbulent flow, and for different blockage ratios. The results are depicted in Fig. 4.3. As expected, the equivalent open velocity (U_C) is larger than the inlet velocity (U_0). Additionally, the corrected velocity increases as the rotor load is increased (C_T) and this later effect is positively correlated to the blockage ratio. Figure 4.3 only shown results to $C_T=1.0$, since for the experiment the blockage ratio is about 9% and this gives a corrected C_T of 0.9, which is basically the maximum power condition from theory.

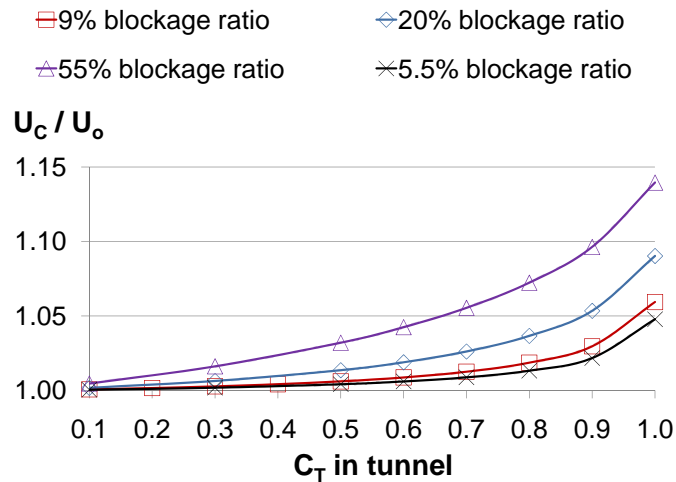


Figure 4.3: CFD-computed corrected velocity to inlet velocity ratio for different blockage ratios and operational conditions

Figure 4.4 shows a comparison between the analytical corrections in §4.1 and the new CFD corrections applied to the power coefficient data simulated for the water tunnel domain. The corrections were made utilizing the information presented in Fig. 4.3 and the relation stated in Eq. (4.8). A good agreement is found between both correction models for the smaller values of blockage ratio, corresponding to 5.5% and 9%, whereas for the highest blockage ratio of 55%, a noticeable difference

appears between the analytical and CFD corrections. At the Betz limit condition, the analytical expressions seem to overestimate the corrections by 7% and 20%, for a blockage ratio of 20% and 55% respectively.

Finally, a correction curve based on axial induction factor $a-C_P$ is obtained for a 9% blockage ratio that will be utilized to correct the experimental data. The correction curve is depicted in Fig. 4.5b which provides information related to the power coefficient increment expected for a given axial induction factor. Given that the novel CFD correction method appears valid for higher blockage ratios, future experimental campaigns will include larger rotors with higher blockage to validate this approach. For these cases, additional CFD data for higher C_T could be used to generate extended correction curves. The use of larger rotors would of course alleviate on-blade Reynolds Re_c number effects as well as provide higher forces which could improve the signal-to-noise ratios of the torque measurements. Typically, optimal operational conditions occur at an axial induction factor of 0.3, thus a potential 20% increment in C_P can be predicted for the experimental data, as seen in Fig. 4.5.

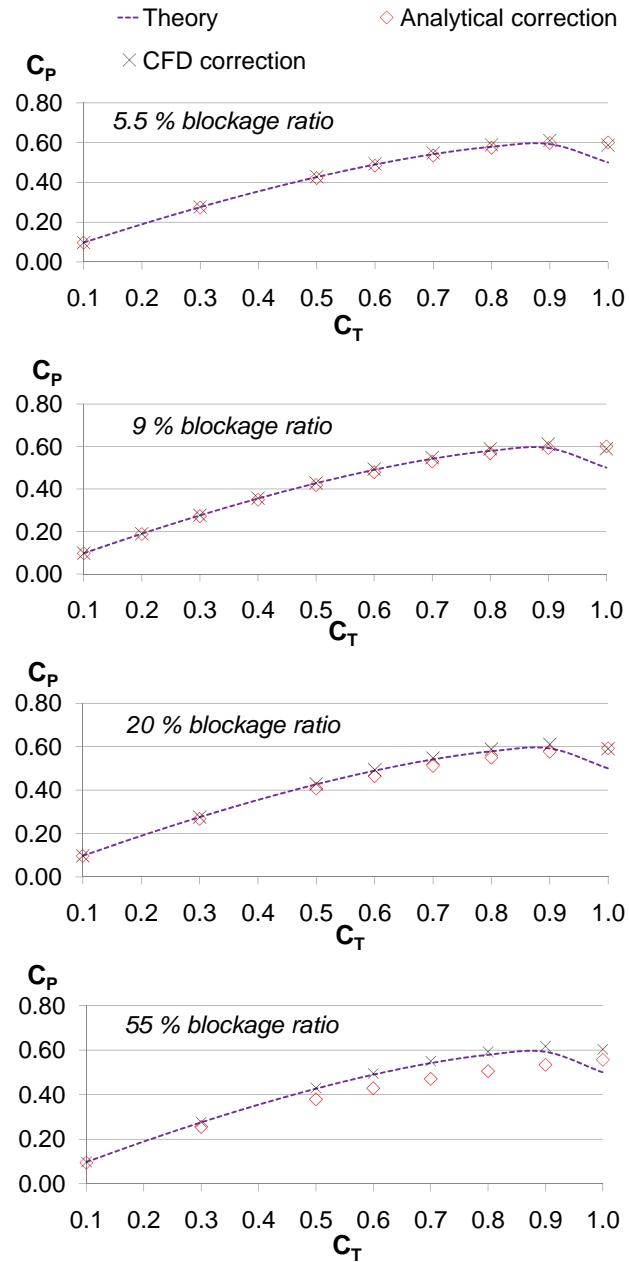
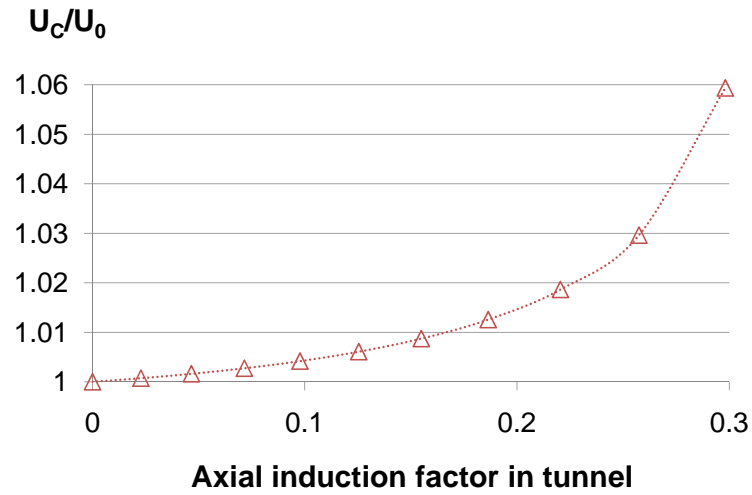
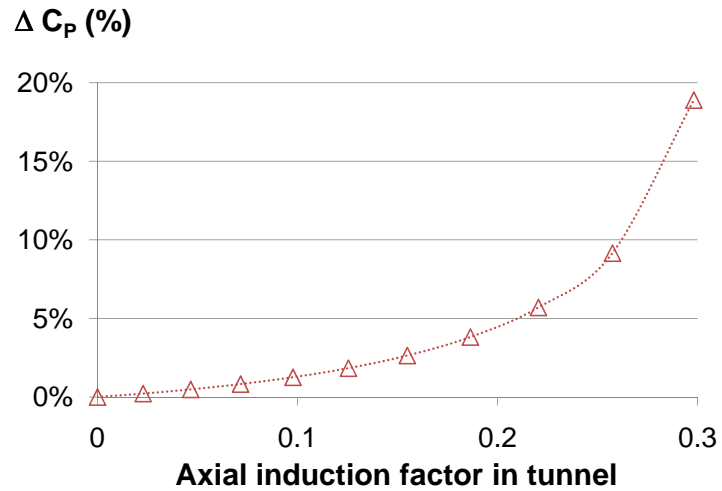


Figure 4.4: Comparison between analytical and CFD power coefficient corrections (all values corrected to free-stream, C_T referred to tunnel conditions)



(a) Ratio of corrected velocity to tunnel velocity v/s axial induction factor for a 9% blockage ratio



(b) Increment in power coefficient v/s axial induction factor for a 9% blockage ratio

Figure 4.5: Correction curve for the experimental testing referenced to tunnel conditions

Chapter 5

Experimental Procedures and Testing Campaigns

The ultimate goal of the experimental rig developed in this thesis is to enable testing of a wide range of model rotors. These scaled models of HATTs and HAWTs will be tested in a pressurized water tunnel at UVic in order to obtain characteristic power coefficients and to address the need for detailed rotor wake measurements that will be used to validate numerical prediction models.

The rig is specifically designed for the water tunnel having a cross sectional area of 45 x 45 cm, with a maximum flow speed of 2 m/s. The nominal rotor diameter designed for is 15 cm, so that the rotor swept area to the water tunnel section will be approximately 9% to limit blockage effects as discussed in previous chapters. However, as noted in Chapter 4, it will be possible to use larger rotors and correct for blockage effects *a posteriori*. The inlet velocity of the water tunnel is limited to 2 m/s. In order to maximize the blade Reynolds number, and to obtain different tip speed ratios, the rotational speed will be therefore be varied. The velocity field in the near wake behind the rotor will be acquired using PIVs technique with digital technology [44, 45].

This chapter first describes the specific objectives of the experimental campaigns to be conducted with the rig. The experiment protocol utilized to carry out experiments is described next, followed by results from the first set of results obtained from the rig. The initial set of results presented in §5.5 (obtained by the author) turned out to be not useful due to a number of difficulties realized after the test campaign. The final set of results presented here were obtained by another co-op student, Peter Root, with post-processing by the author.

5.1 Objectives of the experiment

The two specific objectives of this experimental rig are power output estimation and the acquisition of the velocity field in the near wake behind the rotor, for different operational conditions. Based on the power output estimation, the power coefficient characteristic of the model run under different rotor speeds and inflow velocity in the testing facility can be obtained. This characteristic is the fundamental performance metric of any rotor. The vector velocity obtained in the near wake will provide quantitative information to validate predictive codes. Additionally, as discussed in Chapter 4, the same PIV data can be used to correct C_P values obtained from the experimental data.

5.1.1 Power output

For the power output estimation, the reaction torque of the motor driving the rotor is measured. Having measured this reaction torque, the power output characteristic of the model P_{wt} is estimated as follows:

$$P_{wt} = \tau_{rotor} \Omega \quad (5.1)$$

where τ_{rotor} is the measured reaction torque, and Ω is the angular velocity of the rotor. Once the power output is computed for a diverse range of rotational speeds, the power coefficient characteristic of the model is calculated as shown in Eq. (5.2).

$$C_{P,wt} = \frac{P_{wt}}{1/2\rho U_\infty^3 \pi R^2} \quad (5.2)$$

where $C_{P,wt}$ is power coefficient characteristic of the model running in the water tunnel, ρ is the density of the water, and R the radius of the rotor.

The operational conditions can be expressed as defined in Eq. (2.1), where λ relates the rotor speed and the tunnel inflow velocity, both characteristic factors of the experiment being carried out. Notice that, later on, this experimental data must be corrected to unbounded conditions as detailed in Chapter 4.

5.2 Experiment Protocol

The experiment will run the turbine placed inside a closed section water tunnel over a range of rotational speeds. In such a way, it is possible to obtain a set of torque measurements for a wide range of operational conditions. The results can then be calculated and corrected for C_P and λ to defined the characteristic curve of the rotor.

The first stage in the experiment, once the rig is placed into position with the desired yaw condition for the particular test, is to fill the water tunnel until the section is slightly pressurized. The pressurization is just enough to prevent air to come into the tunnel while running the tunnel and the turbine.

Second, since the torque measurements are the net result of the forces on the blades and the friction in the drivetrain of the rig, as discussed in §2.4, an important step is to quantify the torque due to friction. This must be done without the rotor blades installed, and a dummy hub installed instead of the rotor. The shaft is then driven through the complete range of rotor speeds, and a correlation found between friction torque and rotor speed. This friction torque will include bearing friction, the dynamic seal on the shaft, and the belt system. The tests are run with the water tunnel off, as the freestream fluid motion is unlikely to influence the frictions values obtained (this has been verified experimentally). This frictional torque can then be included in the final calculation of hydrodynamic torque, in order to isolate just the component of torque due to the rotor. This friction estimation should be performed every time the rotor is installed in the tunnel, and ideally before each round of testing.

Third, before starting up the rotor with the blades re-installed (the water tunnel must be re-pressurized as well), the water tunnel is turned on and its flow speed is gradually increased until reaching the value chosen for the set of measurements. Then, the motor is run between 1 and 22 Revolutions per Second (RPS) for the data to be acquired within that range. Notice that, as discussed in §2.4, the motor will operate as a motor or generator depending on the net friction in the system, leading to turbine or propeller operational conditions. This stage can be repeated for a number of different inflow velocities in the water tunnel. The flow velocity is controlled by adjusting the frequency of the pump system of water tunnel recirculation, as Table 5.1 shows. Note that the advertised maximum flow speeds in some cases caused air leakage into the tunnel, making it difficult for the tunnel to operate without air entrainment. This can be avoided through additional pressurization (adding water) to the tunnel during

operation.

Finally, the water tunnel is turned off and the friction measurement is repeated. It is important to open the drainage valve of the water tunnel when decreasing the flow speed, otherwise the testing section is flooded and water will leak between the sealed surfaces in contact with the top of the tank.

Frequency [Hz]	Tunnel inflow velocity [m/s]
15	0.6
25.5	0.9
35	1.3

Table 5.1: Pumping system frequencies and tunnel inflow velocity

5.3 Experimental Blade Sets

The blade sets used in these experiments had simple linear chord and twist distributions. The baseline blades used NACA63(2)-421 airfoil profiles. Inboard the blades blended to a circular profile for attachment to the hub, which had a diameter of 19 mm. Over the active airfoil section of the blade, the chord tapered from 25 mm to 7 mm, and the blade was twisted 15 deg toward stall from zero pitch at the root. The overall pitch angle of the blades in the rotors of the experiments was defined relative to the pitch of the root section, with zero pitch aligning the root section in the plane of rotation of the rotor.

For comparison to simulations, aero or hydrofoil properties at low Reynolds numbers can be input to the simulations, enabling comparison of the larger flow field conditions and power outputs which are the primary area of interest for simulation validation work. The blades produced for the rig using FDM technology (see §2.4.4) inherently have a moderate surface roughness. Previous studies have shown that fixed trip strips on the order of 0.25% chord located in the first 25% of the chord can avoid the laminar separation type behaviour that limit airfoil performance at Reynolds numbers around 1×10^4 to 1×10^5 [46]. The trip serves to prematurely trigger turbulent transition, and this more energetic boundary layer is then able to navigate the adverse pressure gradient on the airfoil without separation. In some cases

full transition may not occur at the trip strip, but reattachment can be facilitated through laminar-turbulent transition over a laminar separation bubble.

Based on literature from the FDM manufacturer¹, the typical surface roughness R_a for the finest T10 tips (0.127 mm inch) is 0.015 mm. For typical chord lengths for the rig's blades around 10-30 mm, the surface roughness is on the order of 0.15% to 0.05% chord, but distributed over the entire blade surface. The natural as-produced surface roughness is therefore expected to be in the proper range to promote transition to turbulence and hence achieve reasonable airfoil performance without massive laminar separation regions or large laminar separation bubbles.

5.4 Measurement Error Estimation

Defining the error of a measurement as the difference between the measured value and the true value of the variable to be measured, in experiments we can identify two main categories of errors: systematic errors and random errors. Systematic errors are fixed or bias errors; they are consistent and repeatable. It is assumed that if the same measuring system is used in the same manner, and several measurements are taken, the error will be the same each time. Random error are the scatter in the data measured caused by a lack of repeatability in the output of the measuring system. The random error in a single measurement corresponds to the difference between a single reading and the average of all reading.

Notice that normally is not possible to know the error level in an experiment. However, the uncertainty interval of the measurement can be estimated. The uncertainty is defined as an estimation of the limits of error in the measurement [47]. Any experimental measurement will include some degree of uncertainty due to lack of accuracy in the data acquisition equipment, random variation in the measurand, sample size, etc.

Random uncertainty can be estimated using the expression given in Eq. (5.3):

$$UNC.R_X = \pm t \frac{S_X}{\sqrt{M}} \quad (5.3)$$

where $UNC.R_X$ is the random uncertainty estimation of the X measurement, S_X is the standard deviation of the sample, M is the sample size, and t is equal to 2 for

¹www.fortus.com

a sample size larger than 30 and a confidence level of 95 %. Notice that random uncertainty trends to zero as the sample size increases.

Systematic uncertainty does not depend on the sample size. In a particular variable measured systematic uncertainties will remain constant if the experiment is repeated under the same conditions. These fixed errors can be estimated but not eliminated from the measurement process.

In this study, uncertainty estimates were done to demonstrate the validity of the results, and took into account the imprecision of the measurement (i.e. random uncertainty) and an estimated maximum fixed error (i.e. systematic uncertainty) in the torque data acquired.

Regarding PIV uncertainty, the main sources of error are related to the particle displacement calculation. These errors mainly result from not choosing the most appropriate method to extract the displacement peak from the correlation function, or for distortion of the correlation function [48]. Low seeding density, velocity gradients, interrogation cell resolution, etc. can cause errors in locating particles' position from the images and errors in velocity calculation. Fortily and Strykowski [48] presented a procedure that allows quantification of the bias and precision errors of DPIV in an attempt to correct the systematic error presented in the mean displacement measurements. However, no PIV data was acquired in this experiment thus, no uncertainty analysis was be done for this measurand. As a reference, a similar experiment what tested a scale model of a vertical turbine [49] in the same tunnel facility estimated the total error in velocity was less than 2 %. However, values for spatial and temporal resolution, appropriate for the operational conditions of this experiment, are needed to more accurately estimate these errors.

5.4.1 Error estimation

In DAQ measurement systems there are several error sources, so called elemental error sources, generating either a random or systematic uncertainty. These elemental errors can be arranged in 5 categories as ASME suggests [47]: calibration uncertainties, data-acquisition uncertainties, data-reduction uncertainties, uncertainties due to method and other uncertainties. This grouping has the sole purpose of identifying and comparing uncertainties in measurements. In the end the elemental uncertainties

are combined by using the square root of the sum of the squares (RSS) to obtain the total uncertainty [47].

The standard calibration process done at the factory is intended to minimize resulting systematic errors, however there are some residual errors, leading to systematic uncertainties. Example of these calibration uncertainties are hysteresis and nonlinearity. In the experiment performed, there are two instruments involved: the torque cell and the NI 9237 module for torque measurement (§2.5).

Table 5.2 presents a summary of the sources of elemental error and uncertainties of the measurements associated with each instrument, based on technical specifications provided by the vendor.

Instrument	Elemental Error	Uncertainty (%)
Torque Cell	Non linearity	0.1
Torque Cell	Repeatability	0.05
Torque Cell	Hysteresis	0.04
NI 9237	Gain error	0.2

Table 5.2: Uncertainties of measurement

Systematic and random uncertainty are combined by using the square root of the sum of the squares (RSS) to obtain the total uncertainty. Notice that, because of the large size of the sample (i.e. greater than 10,000), the random uncertainty is estimated to be zero. Then, the total uncertainty estimates result in approximated $\pm 0.23\%$, obtained as in Eq. (5.4), where UNC is the total uncertainty estimate. This means a maximum possible error of ± 0.0023 Nm for any given measurement. As this error level is so small, error bars are not shown on any of the results plots, as they are too small to be seen.

$$UNC = \sqrt{0.1^2 + 0.05^2 + 0.04^2 + 0.2^2} \quad (5.4)$$

5.5 Initial Testing Campaign

For the first testing campaign, the submerged structure was aligned with the incoming flow, thus no yaw condition was included. The frictional torque was measured for several rotational speeds up to 22 RPS in the water tunnel turned off. The data acquired were voltage values, which were then converted to torque values by simply multiplying the raw data with the conversion factor given by the vendor of the load cell as function of the excitation voltage. Then, the turbine measurements were done for three different water tunnel speeds: 0.6 m/s, 0.9 m/s, and 1.3 m/s, with turbine rotational speed ranging between 1 RPS and 22 RPS.

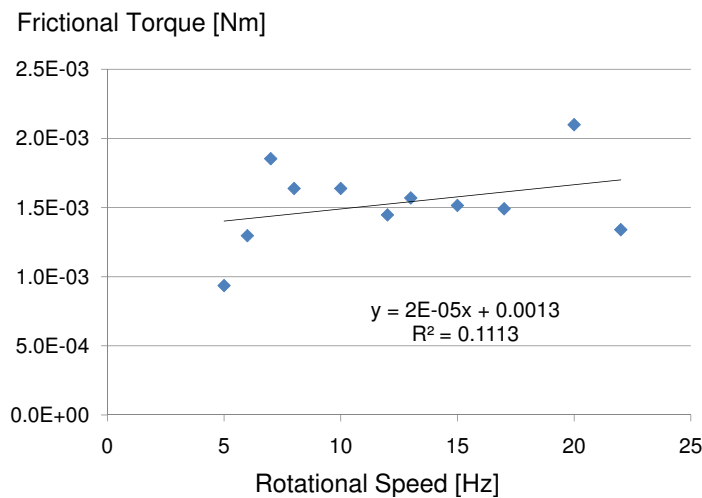


Figure 5.1: Frictional Torque - Dec. 2010

Notice that two forms of friction are present, static and dynamic friction. There is an initial threshold static torque value that must be applied to start the shaft rotating. Beyond that point, dynamic friction occurs. Since it was expected that the dynamic frictional would vary with the rotational speed of the shaft, the frictional torque was measured for different rotational speeds. A linear curve was then fit to the frictional data in a least-squares sense, in order to get an analytical expression to included in the final calculation of hydrodynamic torque. The frictional torque is

plotted in Fig. 5.1. In this first set of runs, frictional torque turned out to be of the same order of magnitude as the turbine torque for rotational speeds up to 12 RPS.

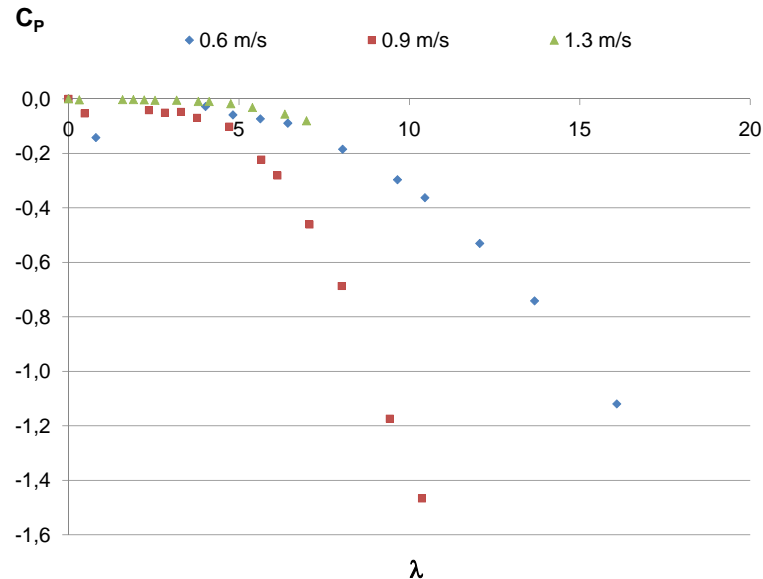


Figure 5.2: C_P v/s λ Results Dec. 2010

The blades of the rotor were then installed at 0° pitch angle relative to the blade roots. Unfortunately, as seen in Fig. 5.2, the measurements obtained in this first campaign were not useful in terms of characterizing turbine performance. Negative C_P values obtained confirmed the rotor was adding energy to the flow, not extracting as expected for turbine rotor behaviour. The rotor operating as a propeller is explained due to misalignment of the blade root, which resulted in a large negative pitch at the tip and consequently, negative angles of attack accelerating the flow downstream (propeller) rather than retarding it (turbine). This illustrates the utility of the motor/generator approach, so both turbine and propeller can be tested at constant λ .

5.6 Second Testing Campaign

As a result of the lessons learning during the first testing campaign by the author, a second testing campaign was performed by a co-op student, Peter Root, who re-designed the blade roots and achieved proper pitch alignment. The tests were re-run

with 1X and 1.5X blades, [50], again with NACA63(2)-4XX airfoil profiles. where the size scaling is defined in terms of chord and blade radius length. The 1.0X and 1.5X blade size designations refer to linearly scaled blades, with the 1.0X blade size corresponding to blades of 75 mm radius length, root chord of 25 mm and tip chord of 7 mm. The overall twist of the blade was kept constant.

Different flow conditions, blade sizes and surface roughness effects were explored in this set of experiments. Measurement were taken at a combination of low tunnel velocity (0.6 to 1.3 m/s) and high tunnel velocity (1.5 to 1.9 m/s); ‘smooth’ and ‘rough’ blade surfaces, for both the 1.0X and 1.5X blade sizes.

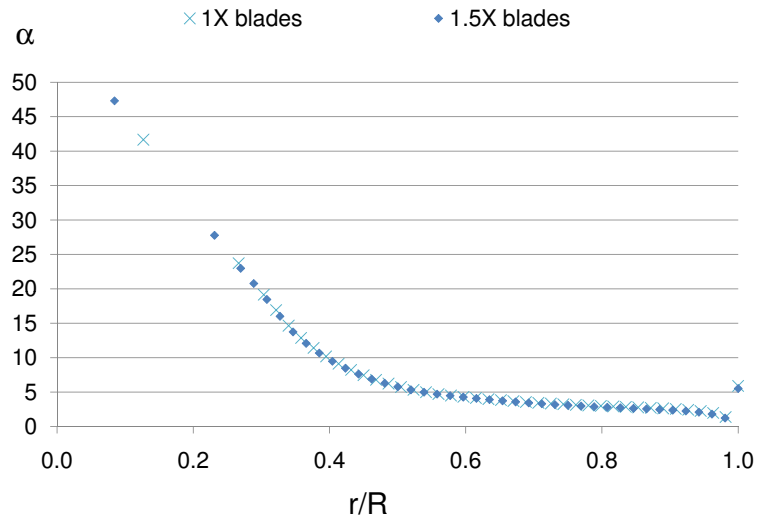
The ‘rough’ blades were produced using T12 FDM tips (see §2.4.4), while the ‘smooth’ blades were produced using T10 tips. The 1.5X blade was obtained by scaling the 1.0X blade up by 50%. Also, BEM simulations were run following the methodology developed by Crawford [51], to be used for experimental results comparison. The BEM code used is typical of design codes used for kinetic turbines. Lift and drag 2D airfoil coefficients were estimated using the XFOIL software² [52], with forced transition at two chord locations, 10 % c and 30 % c . Forced transition was used to reflect the flow conditions on the rough blade surfaces, and because free-transition was found to predict massive separation at the lower Reynolds numbers tested, even though overall rotor performance was not indicative of massive separation.

5.6.1 Operational Conditions

Figures 5.3 and 5.4 illustrate the α and Re operational range respectively, along the blade, for both the 1.0X and 1.5X sized blades. The results are from the BEM simulations where α is defined as the angle of attack determined from the incident resultant velocity in the cross-sectional plane of the airfoil.

This second test campaign also faced inconsistent results for power and C_P values. It was first found that signal to noise ratio is low for the slow tunnel speeds, because torque values measured were quite close to friction torque levels. This can be improved by increasing inflow speeds [50]. Thus, the following test runs were performed with the tunnel running at 1.5 m/s, 1.7 m/s and 1.9 m/s tunnel inflow velocity, corresponding to 40, 45, and 50 Hz pumping frequencies, respectively, as indicated in Table 5.3.

²XFOIL solves a coupled inviscid-viscid problem with boundary layer equations for 2D airfoils. This allows for good prediction of lift/drag performance across a range of Reynolds numbers, up to conditions nearing stall where the approach becomes invalid as gross separation occurs.

Figure 5.3: α (deg) v/s r/R

5.6.2 Experimental Results

Figures 5.5 and 5.6 show the results obtained for the 1.0 X blade size, rough surface, and operating over different ranges of water tunnel speeds. BEM simulations results, for both forced transition location $x_{tr}=0.1$ and $x_{tr}=0.3$, are also plotted as references. Fig. 5.7 plotted the performance curve obtained for the 1.0X blade with smooth surfaces at high water tunnel speeds.

The scatter in the data measured at the low flow speed conditions is noticeable in Fig. 5.5, compared to that occurring at higher water tunnel speeds for both smooth

Frequency [Hz]	Tunnel inflow velocity [m/s]
40	1.5
45	1.7
50	1.9

Table 5.3: Pumping system frequencies and tunnel inflow velocity

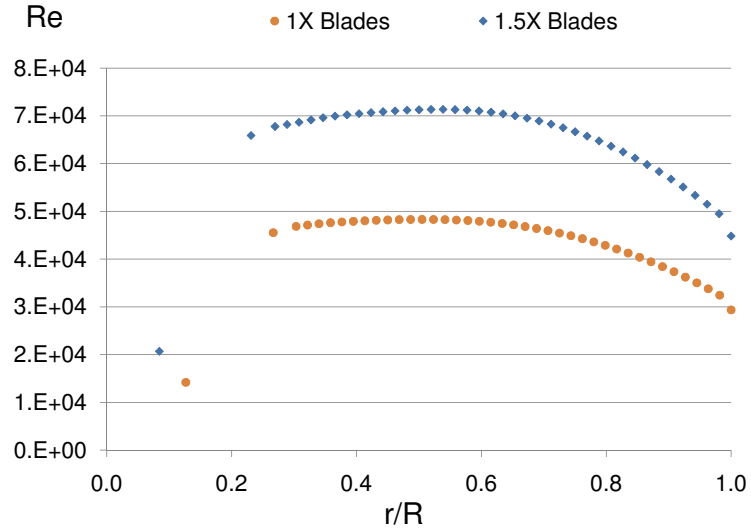


Figure 5.4: Re v/s r/R

and rough blade surfaces. Also, measurements from high tunnel velocities with rough surfaces seems to have better performance curve agreement with BEM simulations than the experimental data for smooth-surfaced blades. The smooth surface blade results show lower C_P peaks compared to the rough surface data, at the same conditions. There is also a clear shift in the C_P vs. λ characteristic between the BEM simulations and the experimental results. The differences are likely related to Re number effects on the blade section characteristics, however the shift in performance curves with respect to expected simulation results are not fully explained by his comparison.

5.6.3 Surface Roughness and Reynolds Number Effects

In order to explore and understand discrepancies due to Re and surface roughness, Fig. 5.8 plots the results for the 1.0X and 1.5X blade sizes, both smooth surfaces, at higher tunnel speeds.

It is instructive to look at the airfoil behaviour for an explanation. Figures 5.9 and 5.10 present predicted 2D lift coefficients over a range of angles of attack at

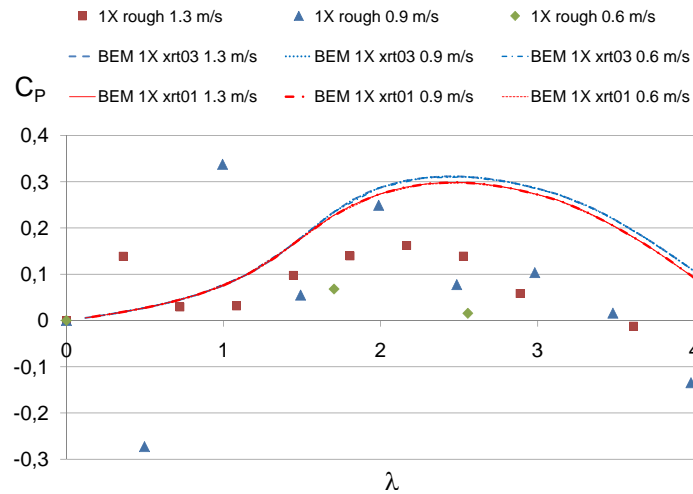


Figure 5.5: C_P v/s λ at low water tunnel velocity (rough)

different Re , for transition forced at 10 % and 30 % chord respectively. Here xtr is defined as the location for forced transition in terms of percentage of the chord length starting from the leading edge of the airfoil section. At a Re of 1×10^5 , there is a bump in the curve between 12 degree and 14 degree data because the transition point moves upstream of the $0.3c$ fixed transition point. The flow over the airfoil becomes turbulent earlier, delaying laminar separation, thus reducing drag and increasing lift. Then, for even higher angles of attack, turbulent separation grows and drag increases. This situation is depicted in Figs. 5.11 and 5.12, at $xtr = 0.1$ and $xtr = 0.3$.

These predicted airfoil performance curves explain to some degree the higher C_P values for the rough blades surface compared to the smooth blades. As shown in Figs. 5.3 and 5.4, the operational Re are in the 3×10^4 to 7×10^4 range and generally below stall. Over those ranges, the $0.1c$ transition location curves (representative of rough blades) generally have better performance in terms of drag compared to the $0.3c$ transition location curves (representative of smooth blades). Therefore, although the BEM results to not predict large differences between bladesets, the experimental data suggests that the airfoil performance is quite sensitive over this Reynolds number range, and to the surface roughness. The better performance of the smooth 1.5X

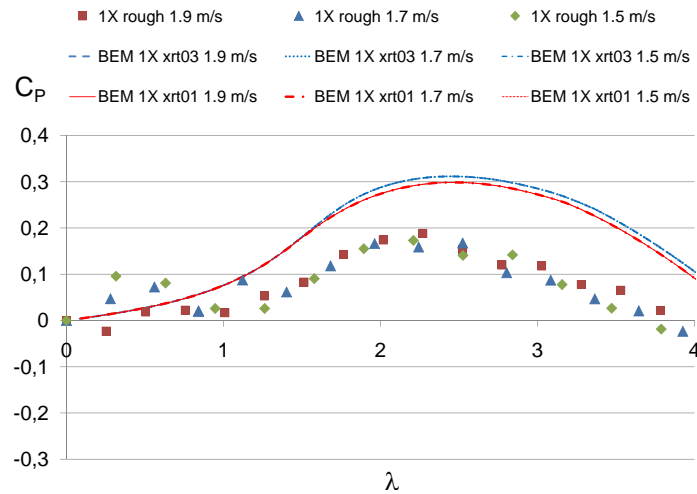


Figure 5.6: C_P v/s λ at high water tunnel velocity (rough)

blades relative to the smooth 1X blades indicate a significant Re effect, given the surfaces have similar roughness. Comparing the rough and smooth 1X blade results in Figs. 5.6 and 5.7 respectively, the rough results are clearly superior in terms of performance, again lending support to the hypothesis that rougher blade delay laminar separation effects and enhance performance at these low Re numbers.

5.6.4 Estimation of Blockage Effects

It is also important to notice that increasing blade size lead to improved full size turbine representation (larger Re), but also affects the measurements due to wake expansion, and hence blockage effects must be explored too. Unfortunately, there was no PIV data available to make a proper correction to experimental data accounting for the induced velocity using the procedures developed in Chapter 4. However, a rough CFD correction can be made, based on the methodology presented in Chapter 4, considering lower and high thrust loads exerted by the rotor.

For the 15 cm rotor diameter (1.0X blade) the blockage ratio is about 9%. Two correction factors $K = U_C/U_0$ are taken from the CFD simulations, Fig. 4.3, the first for a low C_T (e.g. 0.1) and the second for a high C_T values (e.g. 1.0). In such a

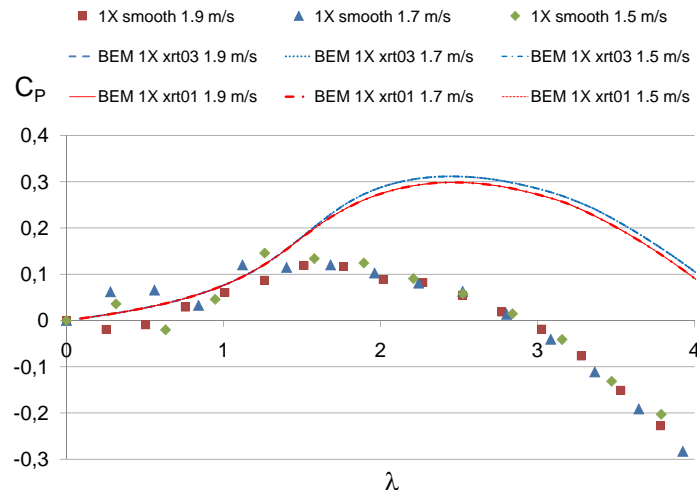


Figure 5.7: C_P v/s λ at high water tunnel velocity (smooth)

way, CFD correction bounds are plotted in Figs. 5.13 to 5.15 over the experimental data for the 1.0X rough blade surface, the 1.0X smooth blade surface, and the 1.5X smooth blade surface, for the water tunnel running at 50 Hz (1.7 m/s flow velocity).

These bounds on the corrections that should be applied to the data in the absence of PIV data. This is true even at the relatively small 9% blockage ratio. It also appears that some of the discrepancy between the 1X and 1.5X blades in Fig. 5.8 can be explained by the higher blockage for the 1.5X blades not being accounted for in the absence of PIV data. This suggests that the Re_c effects may not be as dramatic as initially suggested by the uncorrected performance curves.

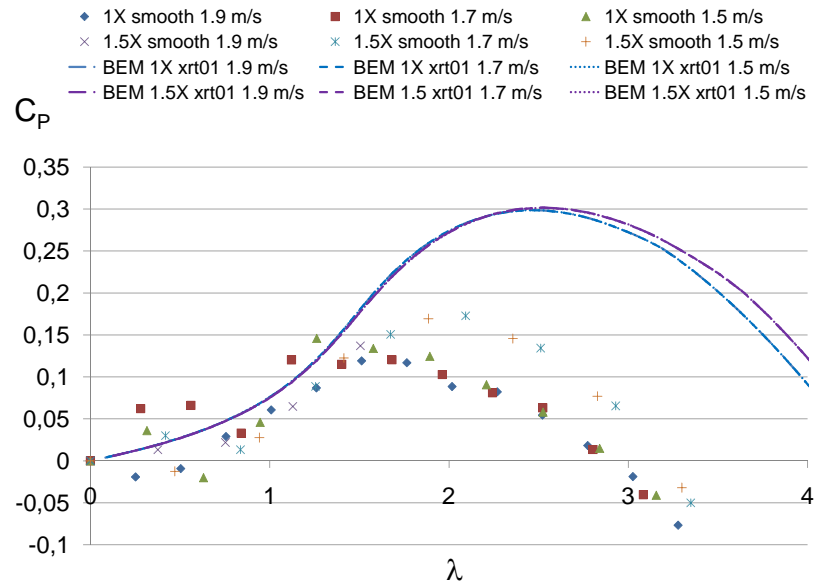


Figure 5.8: C_P v/s λ at high water tunnel velocity, 1.0X and 1.5X smooth blades

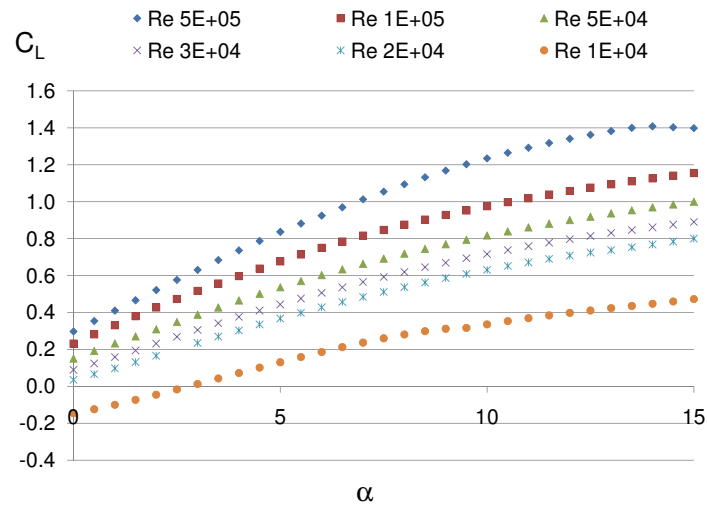


Figure 5.9: C_L v/s α , forced transition at 0.1 chord

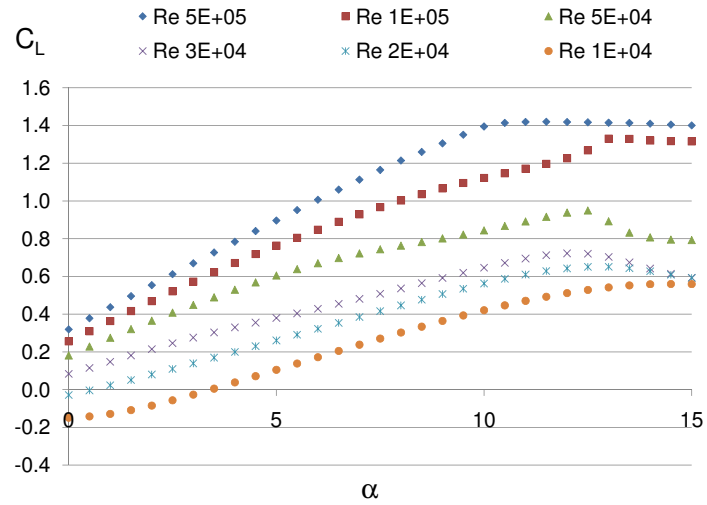


Figure 5.10: C_L v/s α , forced transition at 0.3 chord

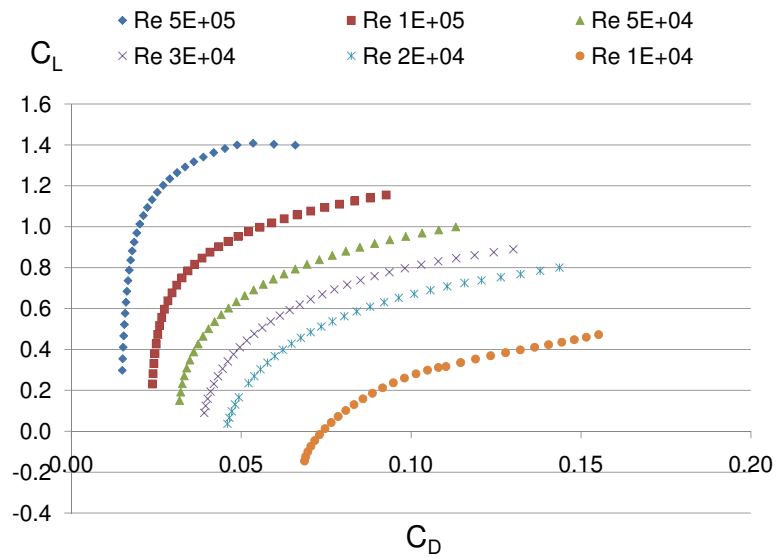


Figure 5.11: C_D v/s C_L $x_{tr}=0.1$

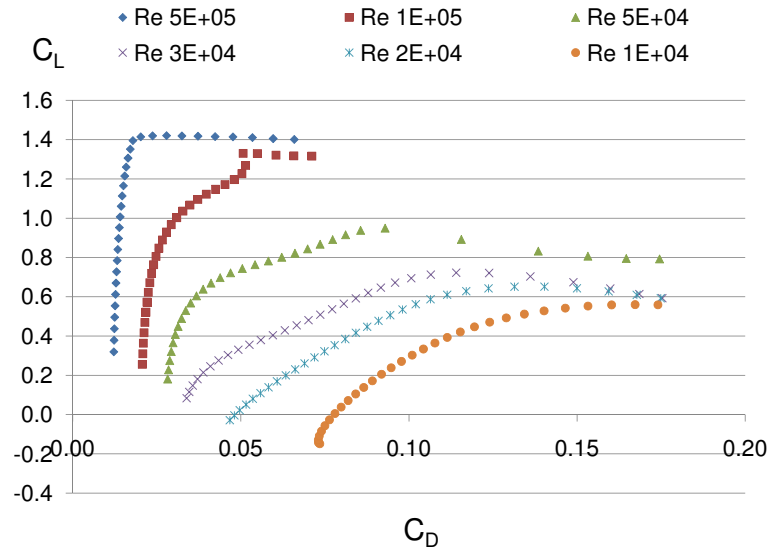


Figure 5.12: C_D v/s C_L xtr=0.3

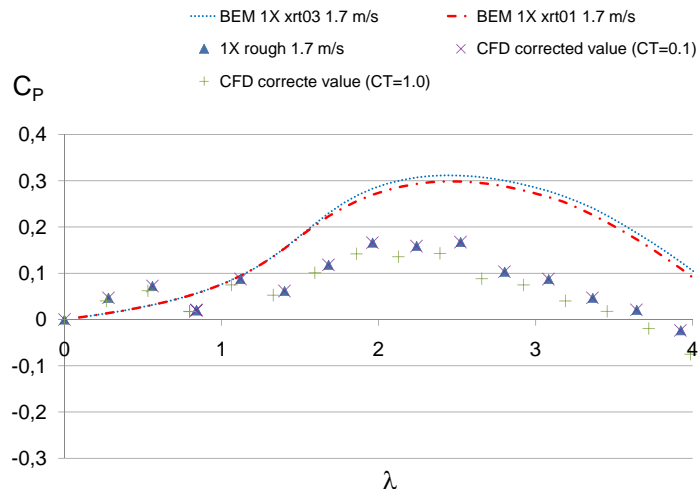


Figure 5.13: C_P v/s λ 1X rough surface blade - correction bounds

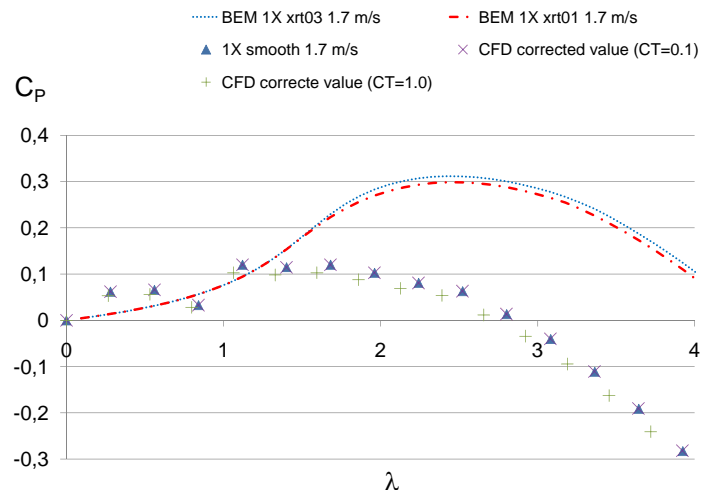


Figure 5.14: C_P v/s λ 1X smooth surface blade - correction bounds

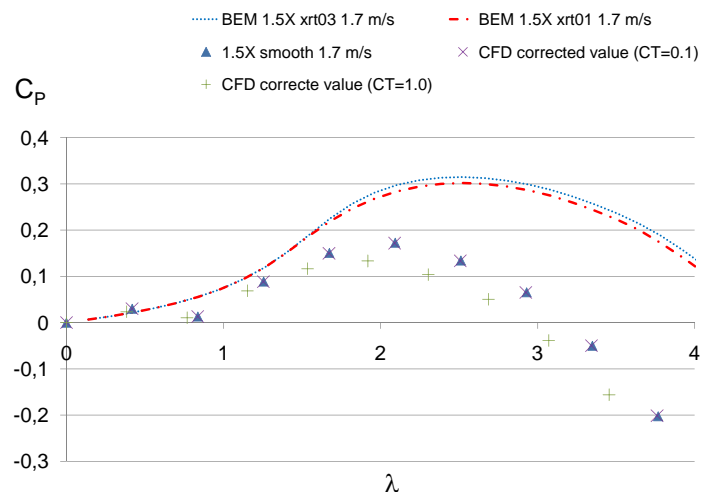


Figure 5.15: C_P v/s λ 1.5X rough surface blade - correction bounds

Chapter 6

Conclusions

Although it was not possible to complete final testing using PIV equipment during the course of this thesis, a number of achievements were made. A rotor rig was designed and tested, which when coupled with PIV measurements will provide high-accuracy data using small-scale blade sets, enabling a large testing campaign. A set of testing procedures were developed, including a PIV-based correction routine, that will enable proper post-processing of the results to account for blockage effects. The initial set of experiments has also highlighted the key areas needing refinement to enable comparison of simulation and experimental results.

6.1 Rig Design

The design of the test rig was a comprehensive task, which included consideration of scaling issues to achieve appropriate scale models that maximize chord Re without compromising the reliability of the experimental data acquired because of blockage effects. FEM modelling of the structure was completed to avoid coupling of vibrations in the system and deformations of the rig support and sting beyond limits predefined. The mechanical design itself meet several conditions both required and desirable for testing purposes. The features of the rig are that it: minimizes the disturbance of flow, allowing testing in yawed flow conditions up to 45° , and providing control over operational conditions; it has an interchangeable hub that allows varying size rotors; and it is a rig that can be added to by other SSDL researchers as future requirements arises. Most notably, the rig could be improved by automation of the yaw system for future tests.

6.2 Computational Fluid Dynamic Simulations

This research developed a methodology for wall interference corrections, based on CFD simulations, that can be applied to find a correction curve for the experimental data acquired in tunnel testing facilities. This curve correlates the average axial induction factor (a) and the power coefficient (C_P) in the water tunnel, and an explicit curve $a-\Delta C_P$ is derived to correct the dimensionless water tunnel power coefficient ($C_{P,wt}$) to freestream conditions.

An interesting outcome is that CFD results and analytical expressions present good agreement (less than 5% difference) for blockage ratios up to 10%. For higher ratios of swept rotor area to tunnel section, analytical expressions - based on the axial momentum theory - seem to underestimate the power coefficient in the water tunnel, which leads to higher analytical correction factors compared to that obtained from CFD simulations.

The results of the wake Reynolds dependency study show the simulations turned out to be Reynolds independent, which allow extrapolating the results of the model to real operation conditions of the full size turbine.

6.3 Experimental Study

An experiment protocol was developed to acquire torque measurements for different operational conditions in order to finally obtain the performance curve of tip speed ratio to characteristic power coefficient.

Two testing campaigns have been carried out so far. The first set of experimental data revealed an error in the alignment of the blade root. The rotor was operating as a propeller rather than a turbine; hence, it was not possible to use the acquired information to characterize the turbine behaviour. However, the testing capability of the rig was successfully verified, and the data acquisition hardware allowed for controlled operational conditions as needed.

The second testing campaign provided more useful results. As first insight, measurements at low torque seem to be easily disturbed by other signals. Comparison of data for each blade set across a range of higher water tunnel speeds show consistent results. Comparison between blade sets of different sizes and similar roughness do however likely show some Re dependency, however the bounds on the tunnel blockage

corrections to the data indicate that this effect may be dominant over Re dependency. In any case, the C_P results of smooth blade surfaces are lower than C_P values obtained from rough blades. Also, the best performance curves from simulation correspond to rough blades at higher water tunnel velocities. It is clear that blade surface is a key factor in the blade performance. Roughness significantly affects flow separation onset on the airfoil profile, causing an earlier transition to turbulence and drag reduction for angles of attack up to approximately 14 degree at $1E + 05 Re$.

6.4 Future Work

It is obvious from the results presented in this thesis that in order to compare simulation and experimental results, the low Reynolds number performance of the airfoils to be used on the blade sets must be ascertained. The effect of roughness, including manufacturing procedures and setup, must be a part of the characterization. To this end, the additional experimental apparatus under construction in the SSDL is required to experimentally measure 2D airfoil performance, as analysis codes such as XFOil have ambiguous parameters and must be validated to use predictively.

Obviously the next step in the rig testing campaign is to integrate the PIV system, and acquire simultaneous torque and PIV data. With this extra data, the mechanical data can be properly corrected. Furthermore, the wake structure information will be invaluable in validating rotor computation models, once accurate 2D airfoil data is obtained. In the longer term, new blade designs can be constructed and tested on the rig to validate performance of a wide range of kinetic turbine designs.

Bibliography

- [1] T. Burton and D. Sharpe, *Wind Energy Handbook*. John Wiley & Sons, 2001. [ix](#), [xi](#), [3](#), [12](#), [14](#), [15](#), [16](#), [64](#), [101](#)
- [2] F. Massouh and I. Dobrev, “Exploration of the vortex wake behind a wind turbine rotor,” *Journal of Physics*, no. Series75-012036, 2007. [1](#), [12](#), [16](#), [41](#)
- [3] L. J. Vermeer, J. N. Sorensen, and A. Crespo, “Wind turbine wake aerodynamics,” *Progress in Aerospace Science*, vol. 39, pp. 467–510, 2003. [1](#), [5](#), [9](#), [11](#), [13](#), [46](#)
- [4] A. Bahaj and L. Myers, “Analytical estimates of the energy yield potential from the alderney race (channel islands) using marine current energy converters,” *Renewable Energy*, vol. 29, pp. 1931–1945, 2004. [2](#)
- [5] J. King and T. Tryfonas, “Tidal power stream power technology - state of art,” *IEEE*, 2009. [2](#), [3](#)
- [6] Tidal Generation Ltd., “Tidal generation.” [2](#)
- [7] Nova Scotia Power, “In-stream tidal turbine project overview.” [3](#)
- [8] J. S. Carlton, *Marine Propellers and Propulsion*. Elsevier, 2nd edition ed., 2007. [3](#)
- [9] L. Blunden and A. Bahaj, “Initial evaluation of tidal stream energy resources at portland bill, uk,” *Renewable Energy*, vol. 31, pp. 121–132, 2006. [4](#)
- [10] I. Bryden, T. Grinsted, and G. Melville, “Assessing the potential of a simple tidal channel to deliver useful energy,” *Applied Ocean Research*, vol. 26, pp. 198–204, 2004. [4](#)

- [11] X. Sun, *Numerical and Experimental Investigation of Tidal Current Energy Extraction*. PhD thesis, The University of Edinburgh, 2008. [4](#)
- [12] X. Sun, J. P. Chick, and I. G. Bryden, “Laboratory-scale simulation of energy extraction from tidal currents,” *Renewable Energy*, vol. 33, pp. 1267–1274, 2008. [4](#), [46](#)
- [13] J. Clarke, G. Connor, A. Grant, C. Johstone, and D. Mackenzie, “Development of a contra-rotating tidal current turbine and analysis of performance,” tech. rep., Energy Systems Research Unit, Department of Mechanical Engineering, University of Strathclyde, Glasgow, UK. [4](#)
- [14] L. Myers and A. Bahaj, “Power output performance characteristics of horizontal axis marine current turbine,” *Renewable Energy*, vol. 31, pp. 197–208, 2006. [4](#)
- [15] A. S. Bahaj and A. F. Molland, “Power and thrust measurement of marine current turbines under various hydrodynamic flow conditions in a cavitation tunnel and a towing tank,” *Renewable Energy*, vol. 32, pp. 407–426, 2007. [4](#), [6](#), [12](#), [16](#), [64](#), [65](#), [66](#)
- [16] L. Myers and A. Bahaj, “Wake studies of a 1/30th scale horizontal axis marine current turbine,” *Ocean Engineering*, vol. 34, pp. 758–762, 2007. [4](#)
- [17] M. G. Gomez, “Marine current turbines: Array effects,” Master’s thesis, University of Strathclyde, 2008. [4](#)
- [18] A. Krynytzky and B. Ewald, *Conventional Wall Correction for Closed and Open Test Sections (Chapter 2nd of AGARDograph 336 Wind Tunnel Wall Correction)*. Advisory Group for Aerospace Research & Development, France, October 1998. [6](#)
- [19] J. E. Hackett and P. R. Ashill, *Wall Correction Methods for Powered Models of Conventional Take Off and Landing Aircrafts (Chapter 7th of AGARDograph 336 Wind Tunnel Wall Correction)*. Advisory Group for Aerospace Research & Development, France, October 1998. [63](#)
- [20] H. Glauert, *The Elements of aerofoil and airscrew theory*. Cambridge University Press, 2nd edition ed., 1947. [6](#), [63](#), [64](#), [65](#), [66](#), [68](#)

- [21] J. Sorensen and R. Mikkelsen, “Wall correction model for wind tunnel with open test section,” *AIAA*, vol. 44, pp. 1890–1894, August 2006. [6](#), [63](#), [64](#), [65](#), [66](#)
- [22] C. Lartiga and C. Crawford, “Actuator disk modeling in support of tidal turbine rotor testing,” in *3rd International Conference on Ocean Energy*, (Bilbao, Spain), Oct. 6–8 2010. [7](#)
- [23] C. Lartiga and C. Crawford, “Water tunnel rotor testing with post processing based on PIV measurements,” in *Proceedings of the ASME 2010 International Mechanical Engineering Congress & Exposition (IMECE2010)*, (Vancouver, BC), Nov. 12–18 2010. [7](#), [9](#)
- [24] B. Rawlings, V. Klaptocz, C. Crawford, C. Lartiga, M. Shives, M. Sireli, and M. Alidadi, “Assessment of blockage effects on tidal energy converter performance,” tech. rep., Nova Scotia Power Inc., Halifax, NS, Feb. 2011. [7](#)
- [25] A. Pope, W. H. Rae, and J. B. Barlow, *Low-Speed Wind Tunnel Testing*. John Wiley & Sons, 3rd edition ed., 1999. [15](#), [16](#)
- [26] J. Whale and C. Anderson, “An experimental and numerical study of the vortex structure in a wake of a wind turbine,” *Journal of Wind Engineering and Industrial Aerodynamic*, vol. 84, pp. 1–21, 2000. [16](#)
- [27] H. Fernando, “Designing a water tunnel rotor dynamometer,” tech. rep., Department of Mechanical Engineering, University of Victoria., 2010. [18](#), [22](#)
- [28] Ansys Inc., *Ansys Help*. ANSYS, 12 ed., 2010. [18](#), [20](#), [109](#)
- [29] D. L. Logan, *A first course in the finite element method*. CL Engineering, 4th ed., July 2006. [19](#)
- [30] Ansys Inc., *Ansys Structural Analysis Guide*. ANSYS, 9.0 ed., November 2004. [20](#)
- [31] E. Wang and T. Nelson, *Structural Dynamic Capabilities of Ansys*. CADFEM GmbH, Munich Germany. [20](#)
- [32] SDP/SI, *Handbook of Timing Belts and Pulley*, 1973. [26](#)

- [33] A. Krothapalli and L. Lorenco, *Atlas of Visualization III, Chapter Four*. The Visualization Society of Japan, 1997. [39](#), [114](#)
- [34] O. Barannyk, “Effect of chordwise flexibility and depth of submergence on an oscillating plate underwater propulsion system,” Master’s thesis, University of Victoria, 2009. [40](#)
- [35] M. E. Harrison and W. M. J. Batten, “A comparison between cfd simulations and experiments for predicting the far wake of horizontal axis tidal turbines.,” in *Proceedings Eighth European Wave and Tidal Energy Conference*, (Upsala, Sweden), pp. 558–565, September 2009. [46](#)
- [36] Ansys Inc., *ANSYS CFX-Solver Modeling Guide*. Ansys, Inc., 13.0 ed., November 2010. [48](#), [50](#), [51](#), [53](#)
- [37] Ansys Inc., *ANSYS CFX-Solver Modeling Guide*. Release 12.0. [48](#), [56](#)
- [38] H. Schlichting and K. Gersten, *Boundary Layer Theory*. Springer, 8th revised edition ed., 2000. [48](#)
- [39] Ansys Inc., *ANSYS CFX-Theory Guide*. [49](#)
- [40] M. P. J. H. Ferziger, *Computational Methods for Fluid Dynamic*. Springer, 2002. [51](#)
- [41] Ansys Inc., *ANSYS CFX-Solver Theory Guide*. Ansys, Inc., 12.0 ed., April 2009. [52](#)
- [42] C. Garrett and P. Cummins, “The efficiency of a turbine in a tidal channel,” *Fluid Mechanics*, vol. 588, pp. 243–251, 2007. [57](#)
- [43] R. Mikkelsen and J. Sorensen, “Modelling of wind tunnel blockage,” in *Proceedings of 2002 Global Windpower Conference and Exhibition*, www.ewea.org, 2002. [63](#), [64](#), [65](#), [66](#)
- [44] M. Raffel and C. Willert, *Particle Image Velocimetry*. Springer, 1998. [73](#)
- [45] C. E. Willert and M. Gharib, “Digital particle image velocimetry,” *Experiments in Fluids*, vol. 10, pp. 181–193, 1991. [73](#), [114](#), [115](#), [116](#)

- [46] P. Lissaman, “Low-reynolds-number airfoils,” *Annual Review Of Fluid Mechanics*, vol. 15, pp. 223–23, 1983. [76](#)
- [47] A. R. G. Anthony J. Wheeler, *Introduction to Engineering Experimentation*. Pearson Education, Inc., second ed., 2004. [77](#), [78](#), [79](#)
- [48] D. J. Fortily and P. J. Strykowski, “Bias and precision errors of digital particle image velocimetry,” *Experiments in Fluids*, vol. 28, 2000. [78](#), [116](#)
- [49] A. Akhgari, “Experimental investigation of the performance of a diffuser-augmented vertical axis wind turbine,” Master’s thesis, University of Victoria, 2011. [78](#)
- [50] P. Root, “Developing and executing test procedures and pos processing strategies for analysis of wind and water turbine blades using a water tunnel,” tech. rep., University of Victoria, 2011. [82](#)
- [51] C. Crawford, “Re-examining the precepts of teh blade element momentum theory for coning rotors,” *Wind Energy*, vol. 9, pp. 457–478, 2006. [82](#)
- [52] M. Drela, “XFOIL: An analysis and design system for low reynolds number airfoils,” in *Conference on Low Reynolds Number Airfoil Aerodynamics*, (University of Notre Dame), 1989. [82](#)
- [53] R. J. Adrian, “Particle - imaging techniques for experimental fluiif mechanics (annual reviews),” *Fluid Mechanics*, 1991. [113](#)

Appendix A

Momentum Theory: The Actuator Disc Concept

Figure Fig. A.1 illustrates the actuator disc concept, where the disc represents a rotor with an infinitive number of blades. The upstream flow gradually slows down its velocity when approaching the disc, and reaches a lower value as it arrives at the disc. Just before the disc, there is a stream-tube expansion as a result of the flow retardation and, since no work has been on the flow yet, the static pressure in the fluid rises to absorb the decrease in kinetic energy. At the disc plane work is done on the fluid, resulting in a static pressure drop ($p_d^+ - p_d^-$) as the fluid passes through the disc. The fluid then proceeds downstream with reduced speed and static pressure; this region of the flow is called the wake. Eventually, far downstream, it is assumed that pressure equilibrium is achieved as the wake achieves full expansion and the static pressure in the wake returns to the original upstream value. In the standard theory, a streamtube is assumed to exist downstream of the rotor separating the external flow and the flow through the rotor. In the very far wake, it is assumed that mixing across the streamtube boundary returns the wake flow back to the uniform inflow velocity.

Within the boundaries of the streamlines, the rise in static pressure is at the expense of the kinetic energy and so causes a further slowing down of the flow.

The flow expansion is due to mass flow conservation, see Eq. (A.1). Because there is a reduction in the velocity, the cross sectional area must increase since the mass flow rate must be the same everywhere along the stream-tube.

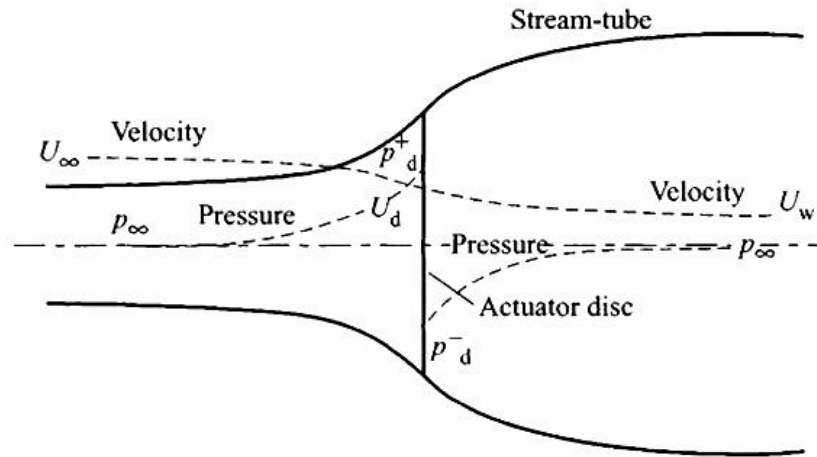


Figure A.1: An energy extracting actuator disk and stream-tube (adapted from the Wind Energy Handbook [1])

$$\rho A_{\infty} U_{\infty} = \rho A_d U_d = \rho A_w U_w \quad (\text{A.1})$$

where ρ is the fluid density; A , U are the cross sectional area and the fluid velocity at the respective locations. The symbols ∞ , d , and w , stand for the undisturbed flow far upstream, the disc position, and the far wake respectively.

Near the disc, the actuator disc reduces the velocity of the free-stream as the presence of the rotor is felt by the flow. This variation can be expressed in terms of the free-stream velocity U_{∞} and the so called axial induction factor a as shown in Eq. (A.2):

$$U_d = U_{\infty}(1 - a) \quad (\text{A.2})$$

The flow inside the boundaries of the stream-tube that passes through the disc experiences a rate of change in momentum, as given in Eq. (A.3) which is essentially given by the change in velocity times the mass flow rate. Notice that in this simplified model the force that causes this change in momentum comes entirely from the pressure difference across the actuator disc, as given by the right hand side of Eq. (A.3). Thought of another way, the momentum deficit is absorbed by the momentum sink representing the rotor in the CFD simulations (§3.2.2).

$$(U_\infty - U_w)\rho A_d U_d = (p_d^+ - p_d^-)A_d \quad (\text{A.3})$$

Then, substituting Eq. (A.2) into the U_d term in left side of Eq. (A.3) we obtain Eq. (A.4):

$$(U_\infty - U_w)\rho A_d U_\infty(1 - a) = (p_d^+ - p_d^-)A_d \quad (\text{A.4})$$

Applying Bernoulli's equations at both sections of the stream-tube, upstream and downstream, with respect to the actuator disc plane, we can obtain the pressure difference across the disc. It is important to notice that the total energy is different upstream and downstream, thus two separate equations, Eq. (A.5) and Eq. (A.6), are required to obtain this pressure difference approaching from upstream and downstream respectively.

The general Bernoulli's equations for steady conditions states that the total energy in a streamline flow remains constant if no work is done on or by the fluid. For this study the flow is assumed to be incompressible ($\rho_\infty = \rho_d = \rho_w = \rho$), and the disc is perpendicular to the flow.

Therefore, in the upstream section Bernoulli's equation results in:

$$p_d^+ = 1/2\rho(U_\infty^2 - U_d^2) + p_\infty \quad (\text{A.5})$$

Between the disc and the downstream station we obtain:

$$p_d^- = 1/2\rho(U_w^2 - U_d^2) + p_\infty \quad (\text{A.6})$$

Next, subtracting equations Eq. (A.5) and Eq. (A.6) we obtain Eq. (A.7):

$$p_d^+ - p_d^- = 1/2\rho(U_\infty^2 - U_w^2) \quad (\text{A.7})$$

Finally, substituting Eq. (A.7) and Eq. (A.2) into Eq. (A.4), we obtain that the relation between the velocity downstream far in the wake and the upstream undisturbed velocity in terms of the axial induction factor a as shown Eq. (A.8):

$$U_w = (1 - 2a)U_\infty \quad (\text{A.8})$$

The thrust force T can be computed from the pressure drop times the disc surface area A_d as $T = (p_d^+ - p_d^-)A_d$. From Eq. (A.4) and Eq. (A.8), we can rewrite the thrust force in terms of the undisturbed upstream velocity U_∞ , the density ρ , and the axial induction factor (a) as given in Eq. (A.9):

$$T = (p_d^+ - p_d^-)A_d = 2\rho A_d U_\infty^2 a(1 - a) \quad (\text{A.9})$$

Then, the rate of work done by the thrust force times the local flow velocity at the disc U_d is defined in Eq. (A.10) (equation obtained from Eq. (A.9) and Eq. (A.2)), which indeed represents the useful power extraction from the air.¹

$$TU_d = 2\rho A_d U_\infty^3 a(1 - a)^2 \quad (\text{A.10})$$

Finally, the useful power extracted ($P = TU_d$) can be non-dimensionalized to give a power coefficient C_P as defined in Eq. (A.11), where the denominator represents the available power in the flow without disc. The equation is finally written in terms of the axial induction factor for the actuator disc theory.

$$C_P = \frac{2\rho A_d U_\infty^3 a(1 - a)^2}{1/2\rho U_\infty^3 A_d} = 4a(1 - a)^2 \quad (\text{A.11})$$

¹Note that TU_∞ is the total work done on the flow by the disc including all wake mixing losses, etc.

In similar manner, the force on the actuator disc (thrust force) is non-dimensionalized, and expressed in terms of the axial induction factor, to give a thrust coefficient C_T :

$$C_T = 4a(1 - a) \quad (\text{A.12})$$

These quantities can also be defined using results from CFD and experimentally determined quantities as:

$$C_P = \frac{P}{1/2\rho U_\infty^3 A_d} \quad (\text{A.13})$$

$$C_T = \frac{T}{1/2\rho U_\infty^2 A_d} \quad (\text{A.14})$$

The development of the analytic tunnel blockage correction models referred to in Chapter 4 is based on this theoretical approach and its limiting assumptions. For example, the maximum achievable value of power coefficient turns out to be 0.593, for $a = 1/3$, commonly referred to as the Betz limit. Recall that the actuator disc model considers the stream-tube to be completely surrounded by flow at constant pressure, with no lateral mixing between the external and internal regions. In addition, if the streamtube is expanding, there must be a net axial pressure force on the sides of the streamtube, but this is ignored in the simple analytic actuator disc theory. As shown in the CFD simulations for unbounded domain in §3.3.1 these assumptions are only approximately true, and so the simple analytic theory must be treated with caution, including instances when correction factors (e.g. for high thrust/induction cases) are employed.

Appendix B

Finite Element Analysis Modelling

As described in Chapter 2, the experimental setup consists of a three-bladed rotor attached to a main shaft which is driven by an electric motor mounted on a platform above enclosed water tunnel. To connect the rotor to the motor (generator) a belt carried up through a vertical support tube which connects to the main body of the turbine. The main upright body ($tube_3$) and the horizontal bodies ($tube_1$ and $tube_2$) are made of alloy aluminum tubing. This appendix describes, step by step, the methodology followed and required in the FEM analysis.

B.1 Geometry and Material Properties

The submerged structure of the testing rig, shown in Fig. 2.3 in Chapter 2, is mainly made of high-strength aluminum (alloy 2024) tubes. This structure can be modelled as three tubes of different length, diameter, and thickness, joined by rigid connections as shown in Fig. 2.3. This scheme is a simplification of the structure that satisfied the purposes of the FEM performed using ANSYS 11.0. The detailed dimensions of each tube is presented in Table B.1.

The density and modulus of elasticity of the aluminum are about one third of the respectively values of the steel. It is ductile and easily machined, which is why it was chosen for this particular design. A Young's modulus of 70 GPa, a density of 2700 kg and a Poisson's modulus of 0.35 are considered as properties for this particular structural model.

The yield strength of pure aluminum is 7 MPa to 11 MPa, while aluminum alloys have yield strengths ranging from 200 MPa to 600 MPa. For this model a value of

Variables	Model 1	Model 2	Model 3	Model 4	Model 5	Model 6	Model 7	Model 8	Model 9	Model 10
Length $tube_1$ cm	30	30	30	30	30	30	30	20	20	20
Diameter $tube_1$ in	0.5	0.5	0.5	0.5	0.5	0.5	0.75	0.5	0.5	0.75
Wall thickness $tube_1$ in	0.058	0.058	0.058	0.065	0.065	0.12	0.12	0.065	0.12	0.12
Length $tube_2$ cm	5	5	5	5	5	5	5	5	5	5
Diameter $tube_2$ in	0.75	0.75	0.75	0.75	0.75	0.75	0.75	0.75	0.75	0.75
Wall thickness $tube_2$ in	0.058	0.058	0.058	0.065	0.065	0.12	0.12	0.065	0.12	0.12
Length $tube_3$ cm	25	25	25	25	25	25	25	25	25	25
Diameter $tube_3$ in	0.75	0.75	0.75	0.75	0.75	1	1	0.75	1	1
Wall thickness $tube_3$ in	0.058	0.12	0.058	0.12	0.12	0.12	0.12	0.12	0.12	0.12

Table B.1: Configurations of study for modal analysis

200 MPa is used as yield strength, typical of the 6061 aluminum available in the machine shop.

The origin is located at key point 1. The tubes are defined in Ansys by keypoints and lines as shown in Fig. B.1. The three tubes are connected by flanges at keypoints 2 and 3, and the rotor is located at keypoint 1.

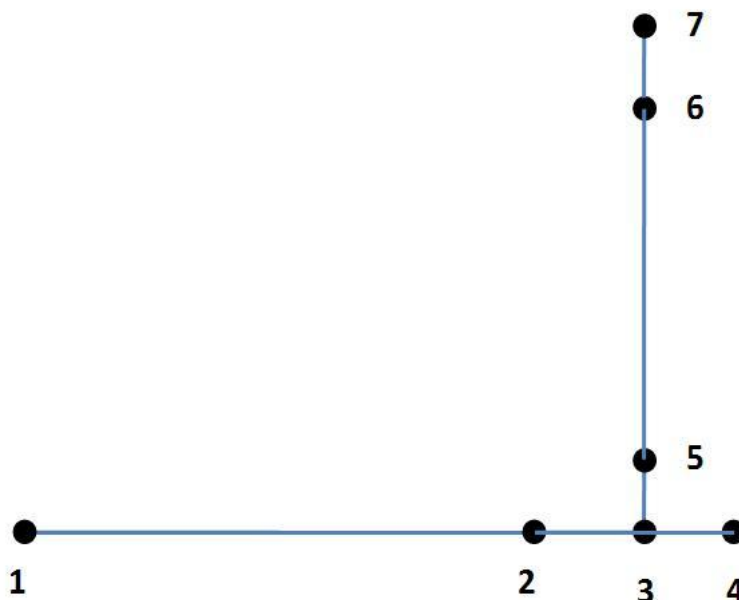


Figure B.1: Rig structure modelling

The seven keypoints defined six line-elements on the model; the properties associated with each type of tubing are set up on each of the six lines. A linear isotropic model is selected for the aluminum material. For the nodal analysis the mass associated to the flanges connection at node 2, 3 and 7 is neglected, however the mass of the rotor at the nose of the structure will be included for the modal analysis as a mass point located in node 1. Nodes 5 and 6 are defined for support of a streamline-plate that will avoid excessive disturbance and forces on the vertical tube. For this analysis, no forces will be applied to these two keypoints, the design of the streamlined component is not yet defined. With respect the boundary conditions, displacement and rotation about all axes are zero at keypoint 7, which connect the tubes-structure with a platform located outside the water tunnel.

B.2 Forces Applied to the System

Referring to Fig. B.2 the tubing-structure will support the rotor located at key point 1, and then the force exerted by the fluid flow at the rotating set of blades will be directly transmitted to the tubing structure. When the rotor is aligned with the horizontal tubing and the plane of the rotor faces the flow orthogonally, the force at node 1 is a vector acting along in the X direction only: F_X as shown scheme. The system will also operate in yawed conditions in the XZ plane. Only the plane of the rotor is modified, and then the tubing structure keeps it location. The force applied on node 1 will be a vector with components acting in the X and Z axis. No yaw is exerted in the YZ plane. Forces applied on any other node are neglected in this model. For the static analysis, the maximum possible value of these forces it is applied.

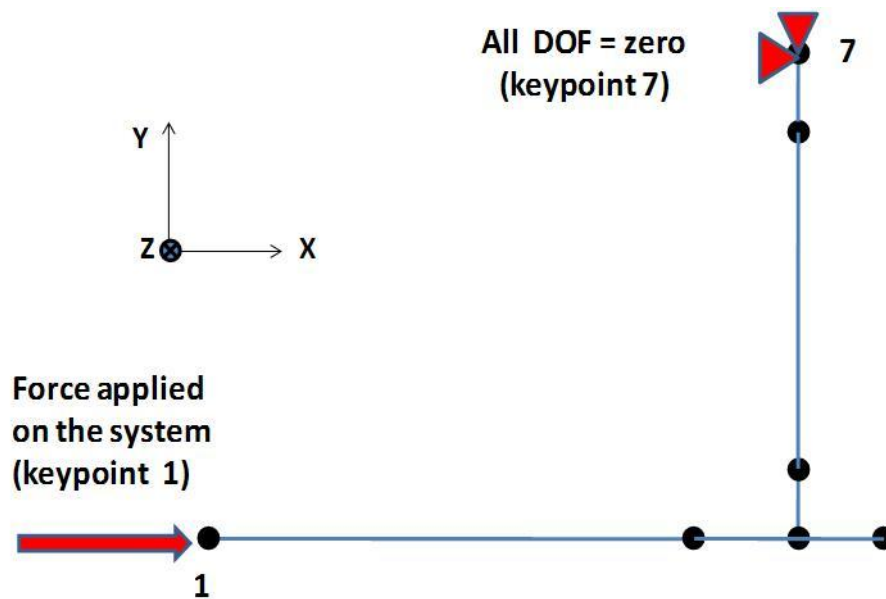


Figure B.2: Rig structure modelling

The resultant maximum forces are summarized in Table 2.2.

Since the forces are both aligned on the rotor axis and yawed in the plane XZ, displacement in X, Y, and Z direction can occur. A three dimensional analysis was

performed, and thus an element with 3D capabilities (axial, torsion and bending in X,Y and Z directions) was used to model the tubes. In addition, a mass element was chosen to represent the rotor attached to the horizontal tubing 1.

PIPE16 Element was selected for the tubes. *PIPE16* is a uniaxial element with tension-compression, torsion, and bending capabilities. The element has six degrees of freedom at two nodes: translations in the nodal x, y, and z directions and rotations about the nodal x, y, and z axes. This element is based on the 3-D beam element (BEAM4), and includes simplifications due to its symmetry and standard pipe geometry [28].

For the element input data, it was required to include the pipe outer diameter and wall thickness, as detailed in Table B.1. The density of the material, elasticity and Poisson's ratio was already defined in material properties for aluminum material. The element mass is calculated from the pipe wall material.

To represent the mass associated with the rotor, the *MASS21* element is available in ANSYS. *MASS21* is a point element having up to six degrees of freedom: displacement in the X, Y and Z direction and rotation about the nodal X, Y and Z axes. The mass element is defined by a single node; in this case associated to keypoint 1, and having a mass of 30 gr.

B.3 Maximum Deflection - Results

The maximum deflection and stresses were computed for the forces estimated at the rotor plane for both, the yawed and non-yawed condition (see Table 2.2 in Chapter 2.

The following Table B.2 shows the maximum deflections and the maximum stresses (von Misses) computed when the inflow is aligned with the axis of the turbine.

Observing the system loaded in the axial turbine direction only, which is the stiffer condition of the structure, models 1 to 4 already experienced deflections of 1 mm or larger. Consequently, those first four configuration were no longer considered for the yawed condition analysis. Tables B.3 and B.5 present the maximum deflection of the structure and maximum von Mises stresses computed for the yawed conditions of 30° and 45° respectively.

Case	Max.deflections [mm]	Max.Stress [MPa]
<i>Model</i> ₁	1.63	24
<i>Model</i> ₂	0.997	14.7
<i>Model</i> ₃	7.31	68.40
<i>Model</i> ₄	0.997	14.7
<i>Model</i> ₅	0.374	7.31
<i>Model</i> ₆	0.374	7.31
<i>Model</i> ₇	0.374	7.31
<i>Model</i> ₈	0.764	14.7
<i>Model</i> ₉	0.286	7.31
<i>Model</i> ₁₀	0.286	7.31

Table B.2: Maximum deflections and stresses (Non-yawed condition)

Case	Max.deflections [mm]	Max.Stress [MPa]
<i>Model</i> ₅	1.5	6.91
<i>Model</i> ₆	1.228	6.91
<i>Model</i> ₇	0.645	6.91
<i>Model</i> ₈	1.064	13.5
<i>Model</i> ₉	0.506	6.57
<i>Model</i> ₁₀	0.358	6.57

Table B.3: Max.deflections and stresses at 30° yaw angle

B.4 Modal Analysis - Results

Results of the modal analysis for models 5 to 10 are presented in Table B.5:

B.5 Mesh Refinement

The structure was defined by 7 keypoints; six element lines Pipe 16 and one element MASS 21 at node and keypoint 1. Different elements size were computed to study the effect of the number of elements in results of the model.

In general terms, a fine mesh allows the definition of small "sub elements" to get good values of the distribution of stresses along the total length of each element. In such a way the solution and stress values will be more precise, and it is possible to

Case	Max.deflections [mm]	Max.Stress [MPa]
<i>Model</i> ₅	2.155	4
<i>Model</i> ₆	1.736	3.84
<i>Model</i> ₇	0.817	3.84
<i>Model</i> ₈	1.219	6.69
<i>Model</i> ₉	0.646	3.37
<i>Model</i> ₁₀	0.378	3.37

Table B.4: Maximum deflections and stresses at 45° yaw angle

Mode	<i>Model</i> ₅	<i>Model</i> ₆	<i>Model</i> ₇	<i>Model</i> ₈	<i>Model</i> ₉	<i>Model</i> ₁₀
<i>Mode</i> ₁	55	56	69	74	97	108
<i>Mode</i> ₂	576	59	76	82	105	117
<i>Mode</i> ₃	204	184	196	175	217	260
<i>Mode</i> ₄	263	235	237	215	274	289
<i>Mode</i> ₅	543	506	713	897	947	1,292
<i>Mode</i> ₆	555	523	742	951	1,002	1,293
<i>Mode</i> ₇	1,446	1,333	1,627	1,385	1,684	1,818
<i>Mode</i> ₈	1,466	1,374	1,635	1,407	1,774	1,874
<i>Mode</i> ₉	1,785	1,743	2,087	2,650	2,549	3,360
<i>Mode</i> ₁₀	1,885	1,797	2,204	3,014	3,031	3,677

Table B.5: Result of modal analysis - natural frequencies [Hz]

identify areas with higher critical tensile stresses in the structure. Specially, when there are distributed loads applied to the system, and the purpose of the analysis is to resolve peak bending stresses, the node point should be near the real location of the peak value, otherwise the linear bending moment can be underestimated. In this particular model there is only one point load. Even if the maximum displacement obtained will be not affected by the mesh size, since a modal analysis was also performed, it was important to obtain accurate solutions for the peak stresses, so mesh refinement was performed.

Note that the maximum number of nodes that the Academic Version of Ansys 11.0 allows is 32,000. Thus, the smallest possible element for this model has a length of 0.025 mm.

For the mesh analysis, a modal analysis was performed over the $Model_{10}$ configuration, with the mass element added at key point 1, considering different element sizes for the mesh. The first 20 modes of each coarser mesh of element sizes 100 mm, 10 mm, 1 mm, and 0.1 mm were compared to the modes obtained for the finest possible mesh of element size 0.025 mm.

Figure B.2 show the differences between the frequency results obtained for each coarser (100 mm, 10 mm, 1 mm, and 0.1 mm) mesh and the finest possible mesh allowed by software limitations. It was found that an element of 0.1 mm size provides accurate enough results compared against to the results obtained for the finest mesh. Thus, this 0.1 mm element size is used to compute the static and modal analysis for the different set of configurations.

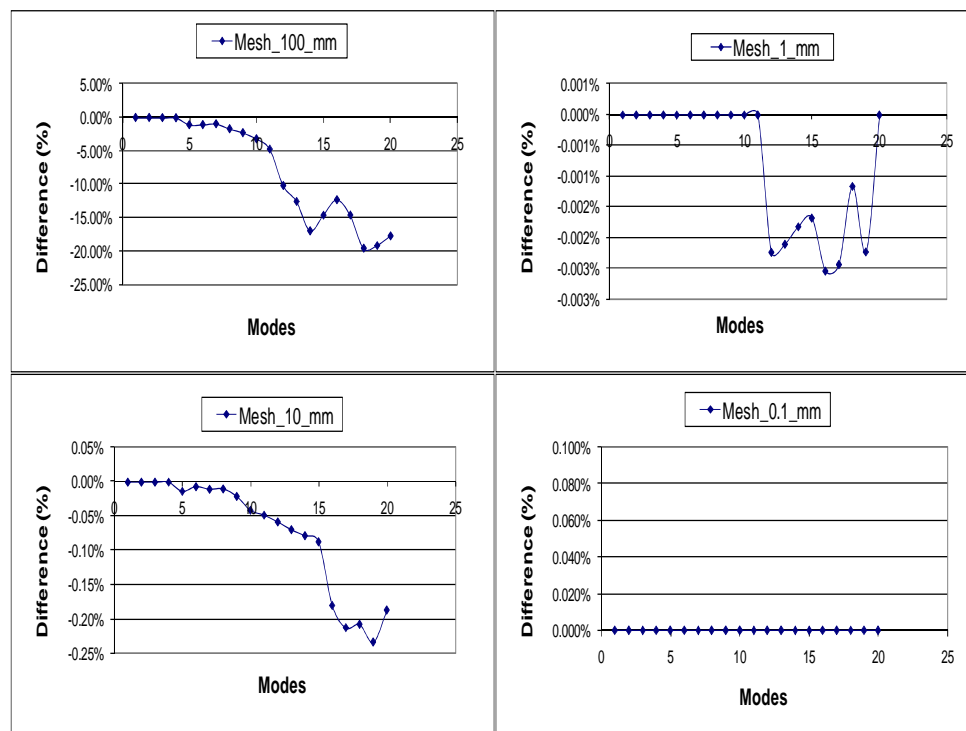


Figure B.3: Mesh analysis ($Model_{10}$)

Appendix C

PIV Theory

The fundamental premise of the PIV technique is that instantaneous fluid velocities can be evaluated by recording the position of images produced by small markers, suspended in the fluid, at consecutive intervals time. This concept assumes that the small particles follow the fluid motion, with minimal lag, and do not modify the fluid properties. Solid particles are often employed as markers, either in liquid or gas fluid flow.

In a typical arrangement of a PIV system, the fluid being studied is illuminated by a pulsed light sheet. A photograph or video device is located in the plane perpendicular to the sheet to capture the light reflected by the particles seeded in the fluid that follow the flow motion. Finally, the information is transferred to a computer to be analyzed [53].

By controlling the pulse light and the continuity of the image recording (frame) several representations of pulse code and framing can be obtained, for example multi-frame/single-pulse, etc. The relevance of the pulse code is to provide images of the location of the particles in an interval of time Δ_t that allows calculating the displacement of the particles for a particular flow condition. The separation of the pulses Δ_t of light in addition to light intensity are the factors that rule the range of velocity possible to be measured, and the sharpness of the particle picture obtained [53].

Two distinct operation modes are possible in this technique: the autocorrelation mode where two or more instantaneous image patterns created by the tracers is recorded in the same frame; and the cross-correlation mode, in which the individual instantaneous patterns are kept in separate frames. The time separation between

exposures is chosen in such a way that the markers will have moved only a few diameters, far enough to resolve their motion, but less than the smallest fluid macro scale. The distance between the multiple-exposed images from one marker, which is proportional to the fluid motion, can be obtained by using standard image processing techniques [33].

In digital particle image velocimetry (DPIV) the information of two consecutive digital images through an interrogation window at a specific area is used, and the local spatial cross-correlation is performed computationally. The mean observed spatial displacement between the particles of the twin images can be predicted with a linear model. The input to the system is the first sampled region $f(m, n)$; the output of the system is the twin image taken in a posterior Δ_t time, $g(m, n)$. The mathematical expression that describes the output function as a result of the displacement function applied to the input data is given by the following Eq. (C.1), which is basically the spatial discrete convolution of $f(m, n)$ and the spatial shifting function $s(m, n)$;

$$g(m, n) = \left[\sum_{k=-\infty}^{\infty} \sum_{l=-\infty}^{\infty} (s(k-m, l-n)f(k, l)) \right] + d(m, n) \quad (\text{C.1})$$

The displacement function can be obtained by finding the best match between the images in a statistical sense. This is achieved by calculating the discrete cross-correlation function $\Phi_{f,g}(m, n)$ of the sampled regions, as is written in the following Eq. (C.2);

$$\Phi_{f,g}(m, n) = \frac{\sum_{k=-\infty}^{\infty} \sum_{l=-\infty}^{\infty} f(k, l) \cdot (g(k+m, l+n))}{\sum_{k=-\infty}^{\infty} \sum_{l=-\infty}^{\infty} f(k, l) \sum_{k=-\infty}^{\infty} \sum_{l=-\infty}^{\infty} g(k, l)} \quad (\text{C.2})$$

Basically, the cross-correlation function statistically quantifies the degree of match between the two samples for a given shift. When a significant number of particles have a strong linear relationship with its twin image shifted, a value of 1 is expected from the cross-correlation. Among the peaks correlation values observed, the highest one represents the strongest match. The maximum cross-correlation value matches the position of the displacement function [45].

The cross-correlation of two functions is equivalent to a complex conjugate multiplication of their Fourier transforms, and the cross-correlation process can be accel-

erating by applying a Fast Fourier Transformation (FFT) [45]. The figure Fig. C.1, taken from *Digital Particle Image Velocimetry* [45] shows the last version of the technique presented by Willert and Gharib (1991). In this enhanced process, the cross-correlation is computed over the spatial frequency domain, where Fourier transform were first performed to both of the images digitally recorded.

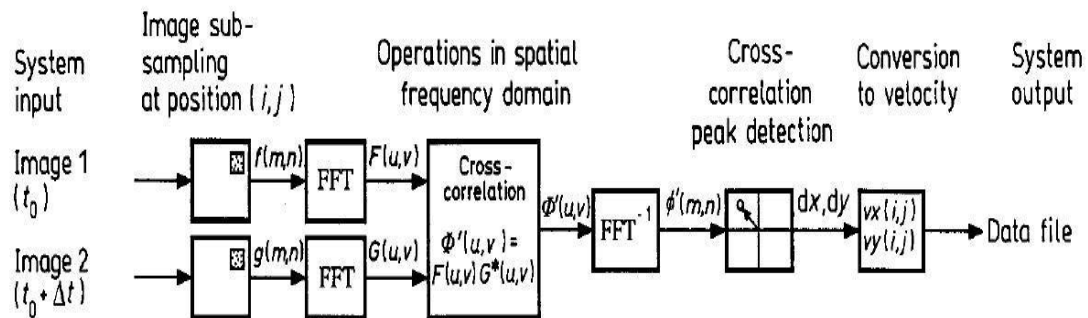


Figure C.1: Numerical processing flow-chart DPIV

By implementing this FFT the number of computations is greatly reduced. To obtain the cross-correlation peak, a parabolic or exponential curve is adjusted around to the highest element initially estimated for the two dimensional array. Finally, once the image displacement have been determined, by using the magnification factor between the image plane and the object plane it is possible to calculate the particle displacement, and then the velocity of the flow.

To deal with the inherent restriction in the resolution and ambiguity in the DPIV measurement, the particle image size, the size of the interrogation window, local velocity gradients, the number of particles within the sampling window, the apparatus performance, quantization effects, and computational errors are factors that must be taken into account when performing the analysis. For example, an increase in seeding densities has a positive effect in the certainty in the measurement. There are two main factors that lead to inaccuracy in the displacement measurement: the intrinsic error of the peak correlation estimation considering three points; and the presence of gradient velocity in the flow field that is not appropriated taking into account [45].

In the experiment carried out by Willert and Gharib [45], which studied the temporal evolution of a vortex ring, the displacement vector obtained shows areas of high velocity gradients near the center of the core. These gradients will bias the cross-correlation peak. To avoid this effect, a possible solution is to lessen the sampling window for the analysis, but this action will also affect the spatial resolution because the lower density seeding of the images taken [2]. Then, the way to deal with this problem is to remove the doubtful data which could lead to misinterpretation, and some vectors for each data set must be interpolated with the associated loss of information. Also, a convolution filtering (low pass spatial filter) could be applied to the data, which eliminates the high frequency jitter associated with the different location estimates of the cross-correlation peak, with no information lost. The validation of the measurements is so far the most difficult and laborious duty within this whole process [45].

Several types of errors can be found in velocity measurement in DPIV; however, the interesting point is the errors in the particle displacement calculation. This error can be the result of not choosing the most appropriate method to extract the displacement peak from the correlation function, or for distortion of the correlation function, for example due to velocity gradient [48]. Fortily and Strykowski (2000) presented a procedure that allows quantifying the bias and precision errors of DPIV in an attempt to correct the systematic error presented in the mean displacement measurements.

In this procedure [48], to resolve the directional ambiguity two digital images at each pulse separation were taken within this region a wide range of flow gradients are presented, and the digital images are processing with the different algorithms available in the software package that is being utilized for the experiment. Firstly, images must be taken for non-flow conditions, several uniform displacement images are generated by varying the mirror speed and pulse separation, in this fashion a wide range of displacement and a detailed measurement of the sub-pixel displacement region are obtained. For example, if the sampling windows size has 128x128 pixels, and the images are interrogated on a spatial grid of 30x10 displacement measurements over the image domain, then 300 displacement vectors can be obtained for each image. If the interrogation windows are large, the displacement peaks results clearly taller than the noise peaks, at each image. Finally, the bias error can be calculated as the difference between the displacement measured and the displacement generated (at each pulse

separation), which represents the error in the average displacement measured. This calibration process is suggested to find the best mathematical algorithm option, for the particular experimental set up, within the available methods available in the software in use.